Ex LIBRIS
UNIVERSITATIS
ALBERTENSIS

The Bruce Peel
Special Collections
Library

Digitized by the Internet Archive
in 2025 with funding from
University of Alberta Library

https://archive.org/details/0162014941072

University of Alberta

Library Release Form

Name of Author [illegible]

Title of Thesis [illegible]

Degree [illegible]

Year this Degree Granted [illegible]

# University of Alberta

## Library Release Form

**Name of Author:** Weimin Chen

**Title of Thesis:** Superconducting and Normal-State Properties of High-$T_c$ Bismuth Cuprates

**Degree:** Doctor of Philosophy

**Year this Degree Granted:** 2000

Permission is hereby granted to the University of Alberta Library to reproduce single copies of this thesis and to lend or sell such copies for private, scholarly, or scientific research purposes only.

The author reserves all other publication and other rights in association with the copyright in the thesis, and except as herein before provided, neither the thesis nor any substantial portion thereof may be printed or otherwise reproduced in any material form whatever without the author's prior written permission.

**University of Alberta**

# Superconducting and Normal-State Properties of High-$T_c$ Bismuth Cuprates

by

Weimin Chen ©

A thesis
submitted to the Faculty of Graduate Studies and Research in partial fulfillment of
the requirements for the degree of

Doctor of Philosophy

**Department of Physics**

Edmonton, Alberta

Spring 2000

# University of Alberta

## Faculty of Graduate Studies and Research

The undersigned certify that they have read, and recommend to the Faculty of Graduate Studies and Research for acceptance, a thesis entitled **Superconducting and Normal-State Properties of High-$T_c$ Bismuth Cuprates** submitted by Weimin Chen in partial fulfillment of the requirements for the degree of Doctor of Philosophy in Physics.

# Abstract

Superconducting and normal-state properties of the high-$T_c$ bismuth cuprates, $Bi_2Sr_2CaCu_2O_{8+\delta}$ (Bi-2212) and $Bi_2Sr_2Ca_2Cu_3O_{10+\delta}$ (Bi-2223), were systematically explored by transport measurements over the full temperature range (4.2 to 300 K).

Bi-2223 whiskers had been grown by adding $Al_2O_3$ in the starting material, while perfect Bi-2212 single crystals were obtained without Al doping. In resistivity ($\rho$) measurement, anomalous features were found near $T^* \sim 250$ K, where $\rho$ deviates upward from the linear-$T$ dependence. The "excess resistivity", $\Delta\rho \equiv \rho - (a + bT)$, forms a kink within about 30 K, which was interpreted to be caused by structural instabilities (lattice distortion). We argue that structural instability is an important factor in high-$T_c$ cuprates. The features below the kink were associated with the scenario of stripe formation. The coherence length ($\xi_c(0) \sim 1$ Å) was determined from the dimensional crossover temperature in superconducting fluctuation. The anisotropy factor, $\gamma \equiv (m_c/m_{ab})^{1/2}$, was found to be 183 (Bi-2212) and 364 (Bi-2223), by scaling the magnetoresistance from different field orientations.

In the mixed-state, various regimes of flux motion were observed in connection with different pinning conditions. Surface degradation (caused by thermal annealing) was found to cause effective pinning, which generally results in thermally activated flux flow (TAFF). The field dependence of the barrier ($U$) takes the form: $U \propto H^{-n}$, with $n =$ 1/6, 1/3, and 1/2. In clean sample, the vortex lattice melts into a highly viscous liquid (due to vortex entanglement). The plastic barrier was confirmed to agree with the

theoretical prediction: $U_{pl} \sim (1-T/T_c)/H^{1/2}$. Above some characteristic temperature, pure free flux flow (FFF) was found in clean samples with perfect surface morphology. The resistance agrees well with the Bardeen-Stephen theory. In other cases, a possible combination of both plastic motion and FFF appears above the crossover temperature. A universal $\rho$-$T$ behavior was also observed in which $d\rho/dT$ approaches a constant. These samples are in the "superclean" regime and the peculiar resistivity was interpreted as due to core-state dissipation. $I$-$V$ characteristics and critical current ($J_c$) were measured. Both $(1-T/T_c)$ and $(1-T/T_c)^{3/2}$ dependencies of $J_c$ were observed at low temperature and near $T_c$, respectively.

# Acknowledgements

I would like to sincerely thank Dr. Jurgen P. Franck for giving me the opportunity to explore the fascinating realm of superconductivity. The present work was completed under his guidance. I also thank Dr. Jan Jung for his co-supervision.

I am deeply indebted to my parents, my wife, and our two boys for their crucial support and patience in my physics studies over the years. I am thankful to all of them.

Many colleagues had offered generous help in this program. I wish to thank Dr. Ray Egerton (electron microscopic measurements), Dr. David Lawrie (inspiring discussions), Dr. John Beamish (low-temperature expertise), Mr. Donald Mullin (machine shop works), Mr. Steve Rogers and Ms. Yolande Peske (weekly liquid helium supply), and many others in the Physics Department.

The exam committee members' work and critical comments on my thesis are gratefully appreciated. Revisions were made according to their suggestions.

Finally I wish to thank all the authors and the following organizations for their kind permission to reproduce published figures (detailed in the text): The American Physical Society, Nature (Macmillan Magazines Ltd.), Elsevier Science, and Springer-Verlag.

# CONTENTS

Abstract

Acknowledgements

Chapter 1 Overview of Crystal Structure and Carrier Doping of Cuprates

1.1 Crystallographic structures ........ 1

1.2 Antiferromagnetism in high-temperature superconductors ........ 7

1.3 The scenario of a stripe phase ........ 12

1.4 Carrier doping ........ 15

Chapter 2 BSCCO Whiskers: Single Crystal Growth, Thermal Annealing, and Sample Preparation

2.1 Growth of Bi-2212 whiskers ........ 18

2.2 Growth mechanism ........ 25

2.3 Growth of Bi-2223 whiskers ........ 26

2.4 Sample preparation ........ 29

Chapter 3 The Normal State of High-Temperature Superconductors

3.1 Unusual normal-state properties ........ 31

3.2 Scenarios for the normal state ........ 39

3.3 Concluding remarks ........ 42

Chapter 4 Unusual Features in the Normal-State Resistivity of Bi-2223 Whiskers

4.1 Introduction ........ 44

4.2 Experiment ........ 45

4.3 Results and discussion ........................................................ 46

4.4 Conclusion ........................................................ 54

Chapter 5 Signatures of Exotic Electronic Scattering

5.1 Structural instabilities in the normal state of cuprates ........................ 55

5.2 Evidence of exotic electronic scattering ........................................ 56

5.3 The scenario of bipolaronic conduction ........................................ 64

Chapter 6 Superconducting Fluctuation ........................................ 68

Chapter 7 Transport Properties of the Mixed State

7.1 General features of the mixed state ........................................ 74

7.2 Activation energy ........................................ 77

7.3 Crossover behavior in flux motion ........................................ 80

7.4 Critical current measurement ........................................ 86

Chapter 8 Anisotropy and *c*-axis Conduction

8.1 Anisotropy factor of BSCCO cuprates ........................................ 90

8.2 *c*-axis transport ........................................ 93

8.3 Influence of twin boundary conduction ........................................ 96

Chapter 9 Dissipation in the Vortex Core ........................................ 100

Summary and Remarks ........................................ 112

References ........................................ 114

## Chapter 1

# Overview of Crystal Structures and Carrier Doping of Cuprates

The physical properties of high-$T_c$ cuprates are closely correlated to their various structural features (of crystallographic, electronic, and magnetic nature). Therefore, detailed knowledge of these important features is helpful in understanding the peculiar behavior of the cuprates [1].

## 1.1 Crystallographic structures

The structures of high-$T_c$ cuprates can be considered as inter-growths of perovskite ($ABO_3$) and rock salt layers (Fig.1.1). The $CuO_2$ layers and the adjacent cations form the perovskite block, whereas the rock salt structure consists of the LaO, BiO, and TlO sheets. The existence of hole carriers in the $CuO_2$ planes is crucial for high temperature superconductivity. This determines the oxidation states of Cu.

In the case of $YBa_2Cu_3O_7$ (Y-123) (Fig. 1.2), there are two kinds of Cu atoms: those in the $CuO_2$ planes with five coordinated oxygen atoms (pyramids) and those in the chains which have four oxygen atoms ($CuO_4$ squares) and a typical oxidation of $Cu^{2+}$. If oxygen content is reduced through thermal annealing, the oxygen is lost from these particular chains. The material becomes insulating when copper is reduced to monovalent $Cu^+$ (with two oxygen atoms left), i.e. $YBa_2Cu_3O_6$. However, the origin of superconductivity is not directly related to these $CuO_4$ chains, because they do not exist in other high-$T_c$ cuprates. Here a charge transfer process occurs which results in the oxidation of the basal coppers ($Cu^{2+}$ to $Cu^{3+}$) in the $CuO_5$ pyramids. The chains are thus known as "charge reservoirs". Adjusting the oxygen amount in these layers of $CuO_x$ chains changes the value of $T_c$. In double-chain $YBa_2Cu_4O_8$ (Y-124), the $CuO_2$ sheets are interconnected by two layers of CuO chains. In this material, variable oxygen

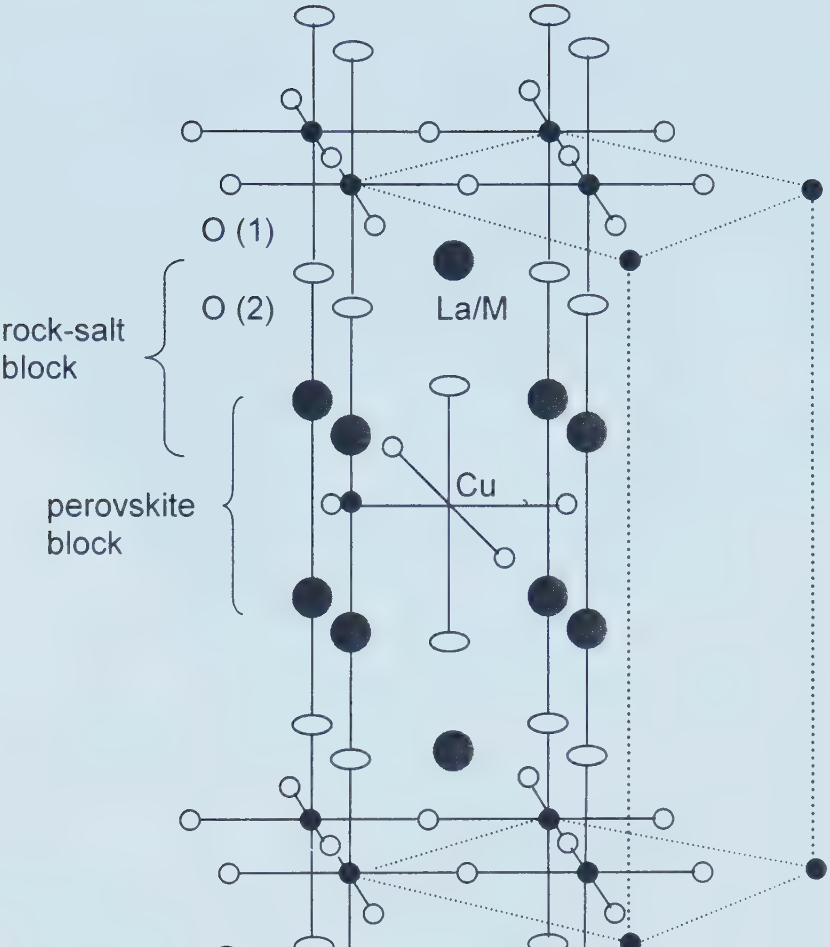
O (1)
O (2)
La/M
rock-salt block
perovskite block
Cu

Fig. 1.1 Tetragonal and orthorhombic unit cells of $La_{2-x}M_xCuO_4$ (M = Sr or Ca) and $La_2CuO_4$, respectively.

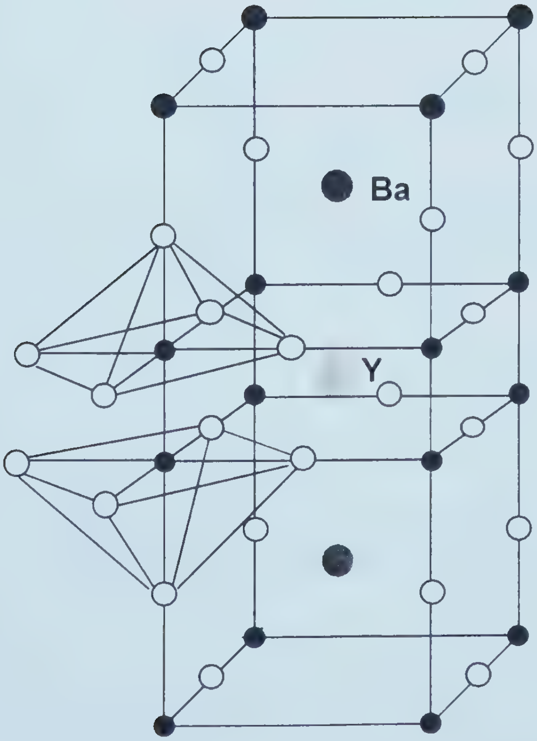

Fig. 1.2 The orthorhombic structure of $YBa_2Cu_3O_{7-\delta}$.

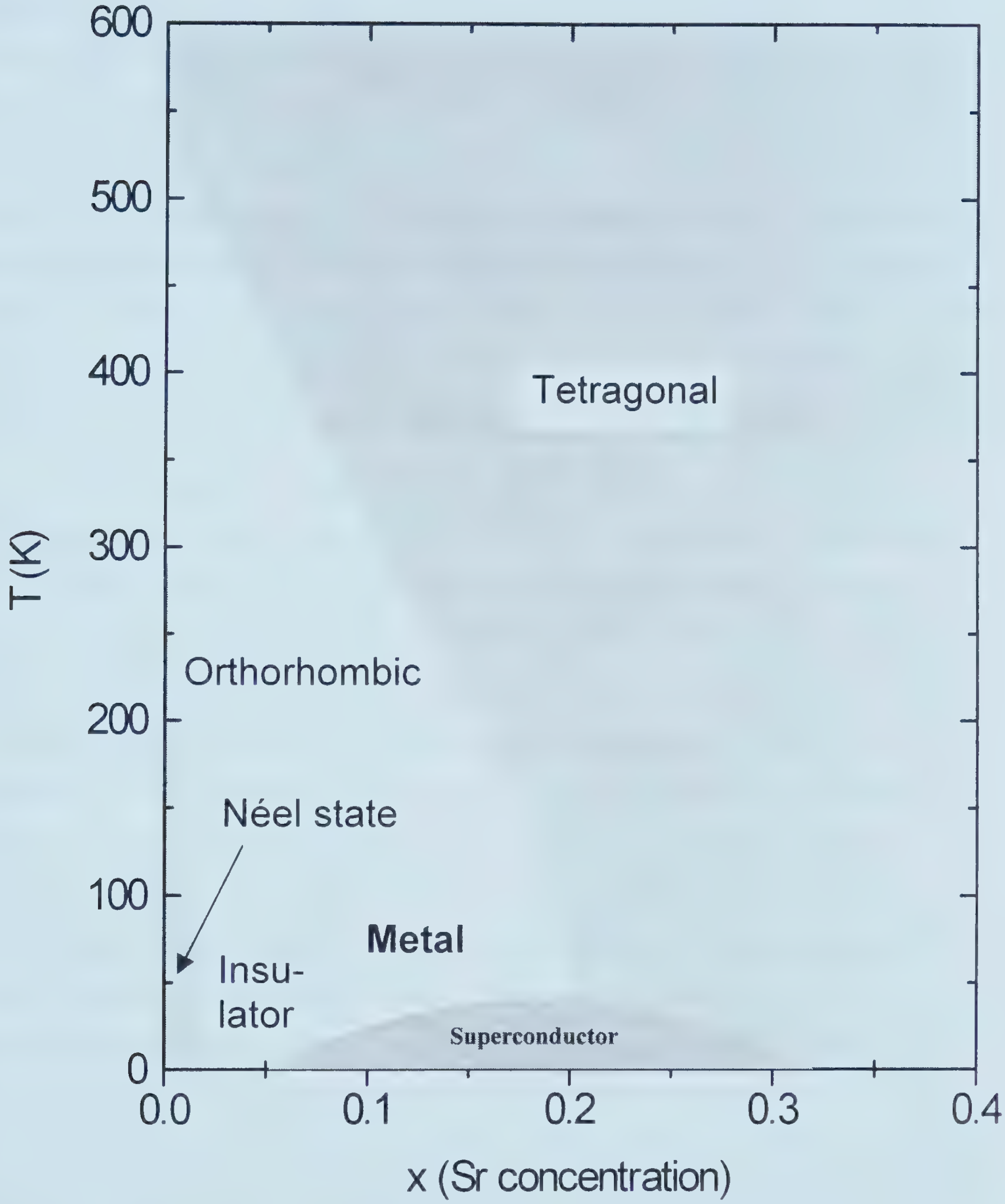

Fig. 1.3 The temperature-concentration phase diagram of $La_{2-x}Sr_xCuO_4$, which schematically shows the different regions of crystal structures and conduction.

stoichiometry in the double chains was not observed as in the single chains of Y-123.

Unsubstituted $La_2CuO_4$ has an A-centered orthorhombic structure. When La is partly replaced by metals, $La_{2-x}M_xCuO_{4-y}$ (La-214, M=Sr, Ba, Ca) forms body-centered tetragonal structure ($K_2NiF_4$ type) [2], which contains sheets of corner-sharing $CuO_6$ octahedra. This material experiences a structural phase transition from the high-temperature tetragonal (HTT) to the low-temperature orthorhombic (LTO) phase as the temperature decreases. Phonon spectrum studies [3] showed the HTT to LTO phase transition is due to the condensation of a soft-titling mode at the Brillouin zone boundary. In the LTO phase, two domains appear which are related to the rotation of $CuO_6$ octahedra around the tetragonal axes [110] or $[\bar{1}10]$, respectively. The HTT to LTO transition temperature $T_0$ rapidly decreases with increasing doping concentration $x$. Fig. 1.3 shows a typical $T_0$-$x$ dependence for $La_{2-x}Sr_xCuO_4$, together with regions of long-range antiferromagnetic (AF) ordering (the Néel state), the superconducting state, spin glass (frozen spin states), and the boundary between the insulating/metallic phases.

The phase transition temperature $T_0$ also shows dependence upon oxygen vacancy $y$. $T_0$ decreases as the charge carriers ($x$-2$y$) in the $CuO_2$ plane increases. This agrees with metal doping in that replacement of $La^{3+}$ by $Sr^{2+}$ increases the number of holes by one, whereas the formation of an oxygen vacancy ($O^{2-}$) increases the number of electrons by two [4]. External pressure suppresses $T_0$, and the orthorhombic phase disappears above a critical pressure $P_c(x)$. Another phase transition from the LTO into the low-temperature tetragonal (LTT) phase was also observed in $La_{2-x}Ba_xCuO_4$ [Refs. 4-8]. $T_c$ exhibits a minimum in this LTT phase near $x$~0.12, which became known as the "1/8 puzzle". Such influence of structural instability of the lattice on electronic properties seems to be a common feature for high-$T_c$ cuprates. This point will be further discussed in the normal-state property measurements (see Chapters 4 and 5).

Bismuth- and thallium-series cuprates have three groups of compounds characterized by single, double, and triple $CuO_2$ planes in their crystal structures (Fig. 1.4). They can be described by a general formula, $A_2Ca_{n-1}B_2Cu_nO_{2n+4}$ with A = Bi (Tl) and B = Sr (Ba). $T_c$ increases with the number of $CuO_2$ planes ($n$ = 1 to 3) from 10 (85), 85(105), to 110(125) K for Bi (Tl) compounds. Four-layer Tl compounds are also obtained. Up to five-layered Tl compounds can be synthesized for $TlCa_{n-1}Ba_2Cu_nO_{2n+3}$ series [9]. The

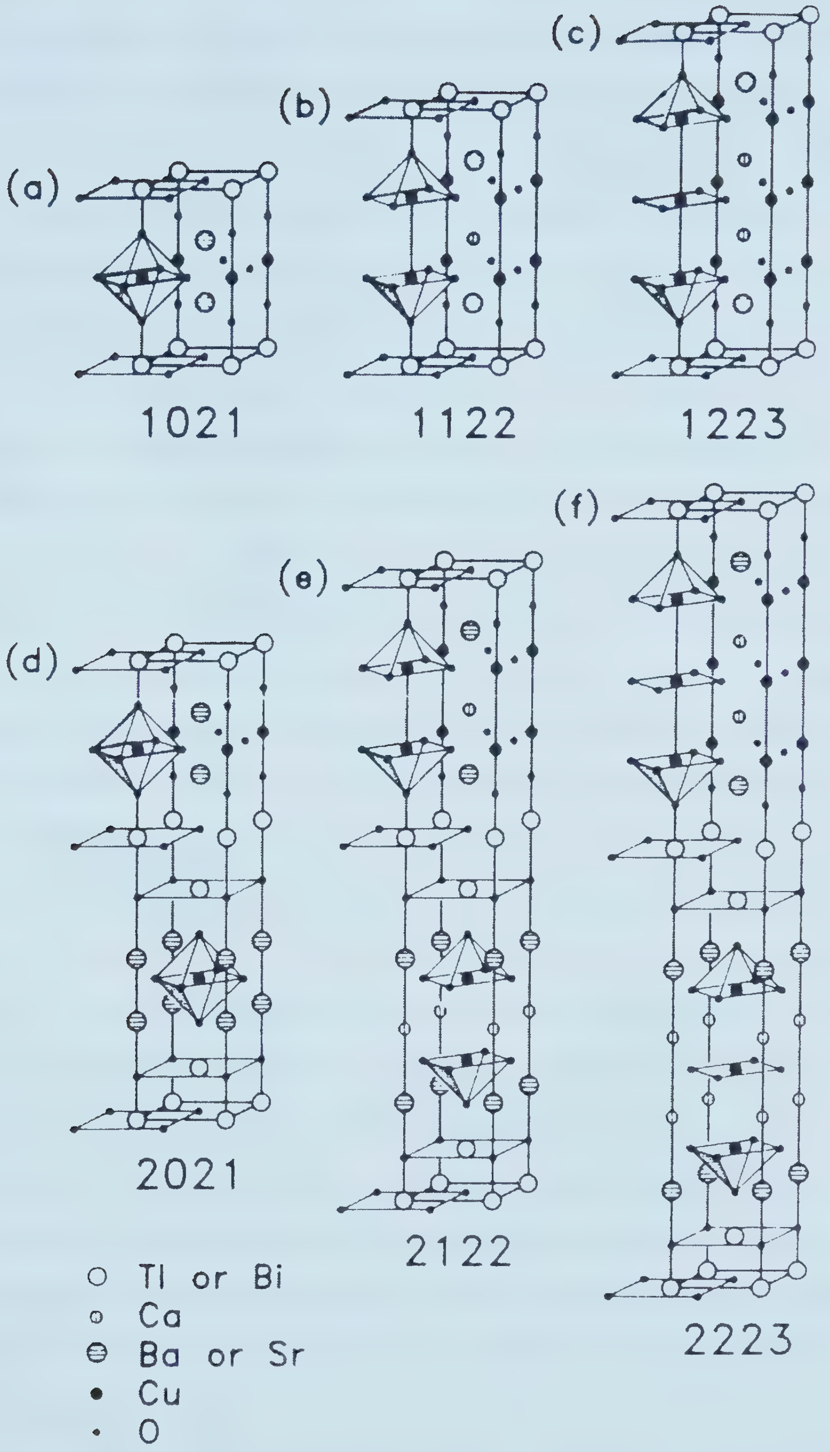
(a)
(b)
(c)
1021
1122
1223
(d)
(e)
(f)
2021
2122
2223
○ Tl or Bi
Ca
Ba or Sr
● Cu
· O

Fig. 1.4 Nominal unit cells for the Bi- and Tl cuprates: (a) $TlBa_2CuO_5$, (b) $TlCaBa_2Cu_2O_7$, (c) $TlCa_2Ba_2Cu_3O_9$, (d) $Tl_2Ba_2CuO_6$, (e) $Tl_2CaBa_2Cu_2O_8$, and (f) $Tl_2Ca_2Ba_2Cu_3O_{10}$. Bi-series only exists in 2021, 2122, and 2223 structures.

simplest pseudo-tetragonal unit of these compounds has the dimension 3.9 × 3.9 Å in the *ab* plane. The lattice constant along the *c*-axis increases with the number of $CuO_2$ planes. For Bi series, $c = 24.4, 30, 37.1$ Å for $n = 1, 2,$ and 3, respectively. The actual structure of Bi compounds has orthorhombic distortions. The pseudo-rhombic elementary cell has the dimensions $a_0 \cong b_0 \cong a_t\sqrt{2} \cong 5.4$ Å and $c_0 \cong c_t$. In Bi cuprates (BSCCO), there exists an incommensurate superlattice structure along the *b*-axis with a periodicity of 4.76 times the lattice constant along the *b* axis [10,11]. Various explanations for this modulation were proposed, such as partial substitution of Sr or Cu for Bi [12,13], ordering of Sr vacancies [14], and insertion of extra oxygen in the Bi-O layer [15,16]. Extra oxygen is most likely the origin since the probability for the former two cases is too small [17]. In these orthorhombic structures (and all other orthorhombic superconductors), atom displacement happens in the Bi-O sheets. "Ladder-like" structures are formed with a Bi-O bond-length of 2.2 Å within the ladder, and a separation of 3.2 Å between them. As a result, the atoms could be clustered to form islands or chains. This gives room for extra oxygen [18]. These compounds can be easily cleaved from the Bi-O layers due to the weaker coupling between them (large separation ~3 Å).

The structure of Tl family compounds possesses higher crystallographic symmetry (tetragonal) with much less lattice distortion. There are atomic displacements in the Tl-O double layers in such a way that Tl-O chains with shorter bond are formed. However, the tetragonal symmetry is maintained due to the short-range order of this modified structure [19]. The $CuO_2$ planes also undergo short-range distortions: the planar oxygen atoms displaced along the *c*-axis at temperatures near $T_c$ [20]. This correlation between oxygen displacement and superconducting transition indicates a strong coupling of the charge carriers with lattice vibrations.

Up to now, the highest $T_c$ (~134 K at ambient pressure; 150-160 K under pressure) is achieved in $HgBa_2Ca_2Cu_3O_8$ (Hg-1223), which has a complex charge reservoir structure consisting of mercury oxide (HgO) layers. The high $T_c$ may come from the effectiveness of charge transfer from the HgO layers. Highly ionic charge reservoirs are less flexible with regards to charge states.

A common feature of layered high-$T_c$ cuprates is oxygen disorder in the buffer layers connecting the $CuO_2$ planes. This affects lattice vibration and may enhance the pairing process. The buffer blocks (charge reservoirs) also determine the oxidation states of the $CuO_2$ planes, resulting in various oxygen-coordination of Cu ions and hence the different series of cuprates. The superconducting properties of cuprates do not solely depend on crystal structures. Other factors such as structural defects and short-range order are crucial for superconductivity, due to the local nature of charge transfer in the $CuO_2$ planes. Finally, structural instabilities typical of perovskite-like compounds are also important in modifying electronic properties of the material.

## 1.2 Antiferromagnetism in high-temperature superconductors

Antiferromagnetic ordering (AF) of the copper spins in the $CuO_2$ planes is another universal feature of high-$T_c$ cuprates. This had led to many theoretical models for electron pairing and normal-state properties. In experimental studies, NMR and neutron scattering techniques also revealed abundant results about the magnetic structure of cuprates. It is clear that the copper spins play an important role in the dynamical processes.

The magnetic properties of the insulating phases of all the high-$T_c$ cuprates are characteristic of three-dimensional S = 1/2 quantum Heisenberg AF correlation between the hole spins of the Cu ions, through superexchange interaction via oxygen ions. This AF ordering can occur at relatively high Néel temperatures $T_N$ = 300 –500 K. Fig.1.5 shows the AF ordering of Cu magnetic moments in the $CuO_2$ plane for $La_2CuO_4$, which has a $T_N \cong 340$ K. For insulating $YBa_2Cu_3O_6$, $T_N \cong 500$ K, whereas Bi compounds can become AF insulating by partially substituting Y for Ca, e.g. $Bi_2Sr_2(Ca_{1-x}Y_x)Cu_2O_8$ with $x \sim 0.5$. When holes are introduced into the $CuO_2$ planes through doping, $T_N$ is reduced dramatically, as shown in the phase diagram of La-214 (Fig. 1.3). Above $x = 0.002$, the long-range magnetic ordering is completely suppressed, leaving only 2-D short-range AF correlations. Even in metallic and superconducting phases, strong spin fluctuations can be observed at high temperature (>100 K). Various scenarios for high-$T_c$

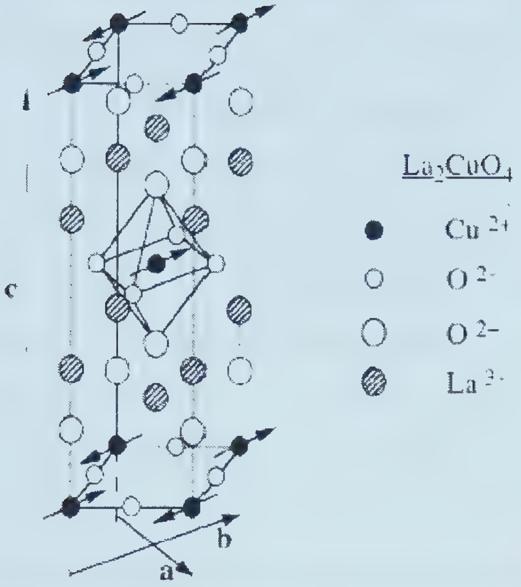

Fig. 1.5 $La_2CuO_4$ unit cell and AF ordering in the $CuO_2$ planes below Néel temperature.

superconductivity, such as spin fluctuations, stripe formation, and spin charge separation (spinon and holon), were proposed based on this point.

The basic magnetic interaction in the insulating phase is well described by the $S = 1/2$ Heisenberg model. The antiferromagnetic exchange interaction $J \sim 1600$ K (or 136 meV) [21]. The Néel temperature $T_N$ is much lower than $J$ because of the strong 2-D nature and quantum fluctuations. Theoretically $T_N$ is zero in a single-layer 2D system. The small interlayer exchange coupling drives $T_N$ to a finite temperature [22]. In the renormalized classical regime, the temperature dependence of AF correlation length, $\xi$, in a 2D quantum spin-1/2 system is given by [23, 24]

$$\xi / a = \frac{e}{8}\frac{\hbar c / a}{2\pi\rho_s}\exp(2\pi\rho_s / k_B T)\left[1 - \frac{k_B T}{4\pi\rho_s} + O\left(\frac{k_B T}{2\pi\rho_s}\right)^2\right], \qquad (1.1)$$

with $\hbar c = 1.657Ja$ and $2\pi\rho_s = 1.131J$ [Ref. 25], where $\rho_s$ is the spin stiffness constant, $c$ is the spin-wave velocity, and $a$ the Cu-Cu nearest-neighbor distance. The Néel temperature $T_N$ can be estimated by a mean-field criterion $k_BT_N = J\alpha_{eff}(\xi/a)^2$, where $\alpha_{eff}$ is related to anisotropy [26].

In the case of $La_{2-x}Sr_xCuO_4$, when Sr concentration is low ($x < 0.05$), the carriers are localized due to disorder and give rise to a typical hopping conductivity: $ln\sigma \propto -$

$(T_0/T)^{1/4}$. At $x > 0.05$, the material becomes metallic because of hole delocalization. The AF correlation length $\xi$ decreases with the increasing of hole concentration: $\xi \sim a/\sqrt{x}$, which also gives the physical meaning of $\xi$ as being the mean hole spacing ($a$ = 3.8 Å) [27]. Spin correlation measurements suggest that holes only affect the correlation of copper spins without changing the value of the localized atomic moment of copper. Moreover, inelastic neutron-scattering experiments show an incommensurate AF structure, i.e. the periodicity shifts from $(\pi, \pi)$ to fourfold-incommensurate wave vectors $[\pi(1\pm\delta), \pi]$ and $[\pi, \pi(1\pm\delta)]$ with $\delta = 0.245$ at low temperatures. This could imply stripe structure of AF fluctuations, or Fermi surface effects [28-31].

NMR is another powerful method for investigating spin correlation [22,32]. The relationship between the longitudinal relaxation time of nuclear magnetization ($T_1$) and the dynamic spin susceptibility is given by

$$\frac{1}{T_1} = \frac{\gamma_n^2 k_B T}{2\mu_B^2} \sum_q \sum_{\alpha=x,y} \left|A_q^\alpha\right|^2 \frac{\operatorname{Im}\chi_{\alpha\alpha}(q,\omega_0)}{\omega_0}, \tag{1.2}$$

where $\omega_0 \to 0$ is the NMR field frequency and $A_q$ is the nuclear form factor. The Knight shift $K$ (the NMR frequency shift caused by nucleus-electron hyperfine interaction) consists of orbital ($K_{orb}$) and spin ($K_{spin}$) contributions. The former is usually assumed to be temperature-independent, and $K_{spin} = \frac{1}{\mu_B} A_{q=0} \operatorname{Re}\chi(q=0, \omega=0)$. The spin-lattice relaxation rate and Knight shift ($K$) can also be expressed by the Korringa law:

$$\frac{1}{T_1 T K^2} = \frac{4\pi k_B}{\hbar}\left(\frac{\gamma_n}{\gamma_e}\right)^2 B, \tag{1.3}$$

where $\gamma_e$ and $\gamma_n$ are the electron and nuclear gyromagnetic ratios. $B$ is a parameter for describing $e$-$e$ interactions and is equal to one for the non-interacting case. If the electron pairing is $s$-wave with a gap ($\Delta$) near the Fermi surface, $1/T_1$ falls exponentially below $T_c$: $1/T_1 \propto exp(-\Delta/k_BT)$; For $d$-wave pairing with nodes in the gap, $1/T_1$ will follow a power-law decay.

Experimental $1/T_1$ data on the insulating $La_2CuO_4$ shows striking enhancement with decreasing temperature, implying the exponential growth of AF correlation length $\xi$. As doping increases, $1/T_1$ crosses over to be nearly $T$ independent for $T > 100 - 200$ K, and eventually to $1/(T_1T) \sim const$ for $x \sim 0.1 - 0.15$. This had been interpreted to follow the Curie-Weiss law: $1/(T_1T) \sim C/(T + \Theta)$, since $\xi \sim 1/\sqrt{T+\Theta}$ from spin-fluctuation theories [33, 34]. The crossover from $T$-independent $1/T_1$ to $1/(T_1T) \sim const$ was attributed to the crossover from incoherent to coherent charge and spin dynamics.

AF ordering of Cu sites in the $CuO_2$ planes occurs in $YBa_2Cu_3O_{6+x}$ for $x < 0.4$. The Cu moments in the adjacent double layers are also antiferromagnetically correlated and there is no moment on the chain, as revealed by neutron scattering [35]. The low temperature value of magnetic moment on the planar Cu ions is $0.64\mu_B$, smaller than the static value due to quantum fluctuations. As in $La_{2-x}Sr_xCuO_4$, the moment and $T_N$ are suppressed by increasing oxygen content, and the local moment remains constant. This indicates the holes are localized in the Cu $3d^9$ state. At the critical oxygen concentration $x_c = 0.41$, long-range AF correlation is completely destroyed. This corresponds to a maximum hole density in the plane: $n_c \sim 0.02$ (since $\xi \propto 1/n^{1/2}$), in agreement with that of $La_{2-x}Sr_xCuO_4$ (see Fig. 1.3). This behavior shows that charge redistribution happens in the chain for $x < x_c$ without affecting the valence of planar Cu ions. At $x \geq x_c$, large number of holes appear in the planes and suppress the AF correlation as well as oxidize the coppers [36].

One of the most important features in the magnetic structure is the "spin gap", which manifests as a suppression in the low energy spin excitation spectrum below some temperature $T^*$ ($>T_c$). Since this does not generate a true gap in the density of states, nor is it accompanied by a clear gap-like structure in the low energy charge excitations, the spin gap is thus also known as a "pseudogap". The suppression of spin excitations indicates the singlet pair formation (total spin $S = 0$). In overdoped or optimally doped samples of $YBa_2Cu_3O_{7-\delta}$, $1/T_1T$ behaves like the case of $La_{2-x}Sr_xCuO_4$; In underdoped samples, however, $1/T_1T$ decreases below 150 – 200 K, signifying a pseudogap behavior. Similar phenomena have been observed in other cuprates, such as $YBa_2Cu_4O_8$ and $HgBa_2Ca_2Cu_3O_{8+\delta}$ [37, 38]. This feature was not evident in $La_{2-x}Sr_xCuO_4$, which

had been attributed to the monolayer structure, in which the lack of transverse AF exchange coupling between adjacent $CuO_2$ layers was thought to prevent the formation of a pseudogap. However, recent data from both underdoped $La_{2-x}Sr_xCuO_4$ [39] and single-layer $HgBa_2CuO_{4+\delta}$ [40, 41] show similar features to those of underdoped $YBa_2Cu_3O_{7-\delta}$. Nevertheless, comparing with the monolayer La compounds, a sharp resonant spin excitation dominates the spectrum in the superconducting state of $YBa_2Cu_3O_{7-\delta}$, but is absent in the former. Recent neutron scattering results showed that the low-frequency magnetic excitations in $YBa_2Cu_3O_{7-\delta}$ are very similar to the case of $La_{2-x}Sr_xCuO_4$ [42]. This suggests the low-energy spin fluctuations found in both single- and double-layer cuprates may be a universal feature. The pseudogap anomaly was also observed in neutron-scattering experiments [43]. Another puzzle comes from the Gaussian decay rate, $1/T_{2G}$, of the nuclear spin-spin relaxation ($exp[-t^2/2T_{2G}^2]$). $1/T_{2G}$ does not show a gap-like decrease, perhaps due to the compatibility of antiferromagnetism and superconductivity [44]. The relation between the pseudogap opening temperature ($T^*$) and hole doping was established experimentally [37, 38], however it is not very clear whether $T^*$ would linearly extrapolate to extremely underdoped levels or saturate, both cases had been proposed by different theories, such as spin-charge separation [45] and spin-fluctuations [46]. There is also ambiguity about possible extension of such a pseudogap into the overdoped regime or even evolution into a superconducting gap, or whether it could be persistent below $T_c$ and independent of the superconducting gap.

The magnetic properties of Bi-series cuprates are mainly studied by neutron scattering and angle-resolved photoemission spectroscopy (ARPES). Inelastic neutron scattering revealed a resonate peak at $\mathbf{Q}_{\|} = (\pi/a, \pi/a)$, the so-called π resonance, and 43 meV in the superconducting state of $Bi_2Sr_2CaCu_2O_{8+\delta}$ [47], similar to the case of $YBa_2Cu_3O_{7-\delta}$. Intensity modulation originated from interlayer magnetic coupling was also observed for the wavevector $\mathbf{Q}_{\perp}$ perpendicular to the $CuO_2$ planes. The resonate peak is believed to be linked with the superconducting condensation energy [48, 49]. Most recent inelastic neutron scattering results from $YBa_2Cu_3O_{6+x}$ [50] showed that the onset temperature $T^*(x)$ of the pseudogap (from NMR and transport measurements)

coincides with the formation of the resonance. This supports the superconducting scenario of spin-fluctuation acting in the role of phonons as in the BCS formalism. In the "shadow band" theory [51], electron scattering by the antiferromagnetic wave vector $\mathbf{Q}_{||}$ produces a shift by $\mathbf{Q}_{||}$ from the original band, causing a "shadow band". Angular distribution of photoelectrons from ARPES showed evidence of "shadow Fermi surfaces" in optimally doped $Bi_2Sr_2CaCu_2O_{8+\delta}$ [52], in which the center of the Fermi surface was moved from (π, π) to (0, 0). A similar study also found the shadow bands [53], but pointed out that the bands could be due to the structure modulation in the BiO planes. Another arising scenario of high-$T_c$ superconductivity is the charge and spin stripe structure in the $CuO_2$ planes, which will be reviewed in the next section.

To briefly summarize, long-range AF ordering exists in the insulating parent compounds with high Néel temperatures $T_N \approx 300 — 500$ K. Hole doping destroys such long-range ordering (at $n_h \approx 0.02$; or $n_e \approx 0.15$ for $Nd_{2-x}Ce_xCuO_4$). However, 2D correlation survives in the superconducting state, whereas in the metallic normal state, a spin gap develops.

## 1.3 The scenario of a stripe phase

There have been a lot of theoretical and experimental studies on the stripe structure of high-$T_c$ cuprates in recent years. This model incorporates electronic and magnetic structural features, and holds the potential as a candidate theory for high-$T_c$ superconductivity. The basic picture of this scenario is the antiferromagnetic antiphase ordering of Cu spins into domains in the $CuO_2$ planes and charge (hole) segregation into the domain walls, forming a striped structure [54-59]. Fig. 1.6 schematically shows such a stripe ordering, where the circles with arrows represent Cu spins and the filled ones are holes. The immediate consequences of this phase formation include low-dimensionality caused by charge segregation and incommensurate magnetic effects due to the AF domains. A few mechanisms for the driving force of stripe phases were proposed. One is the frustrated phase separation [55]: charge stripe orderings were driven by a competition between phase separation (a tendency of hole expulsion from

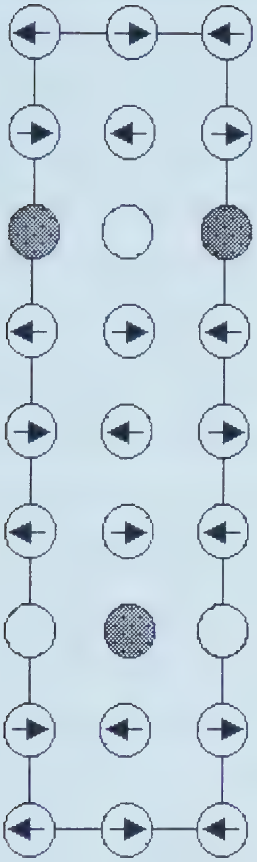

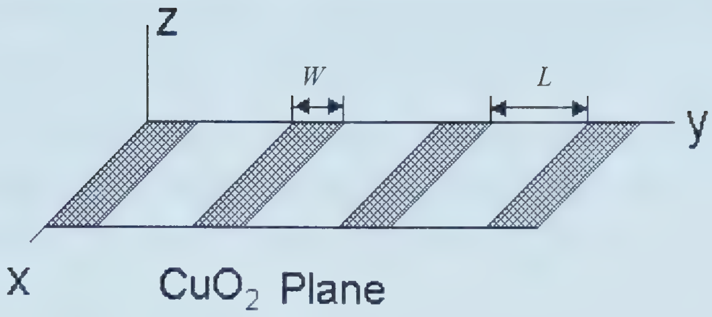

Fig. 1.7 Schematic view of quantum stripes in the $CuO_2$ plane. Blank (shaded) stripes represent LTO (LTT) lattices of widths $L \sim \lambda_F$ and $W \sim \xi_0$, respectively.

Fig. 1.6 (left) Diagram of a stripe ordering in the $CuO_2$ plane. The arrows represent the Cu spins: AF in each strip, and antiphase in the domains separated by the charge strips. The filled circles are charges (holes).

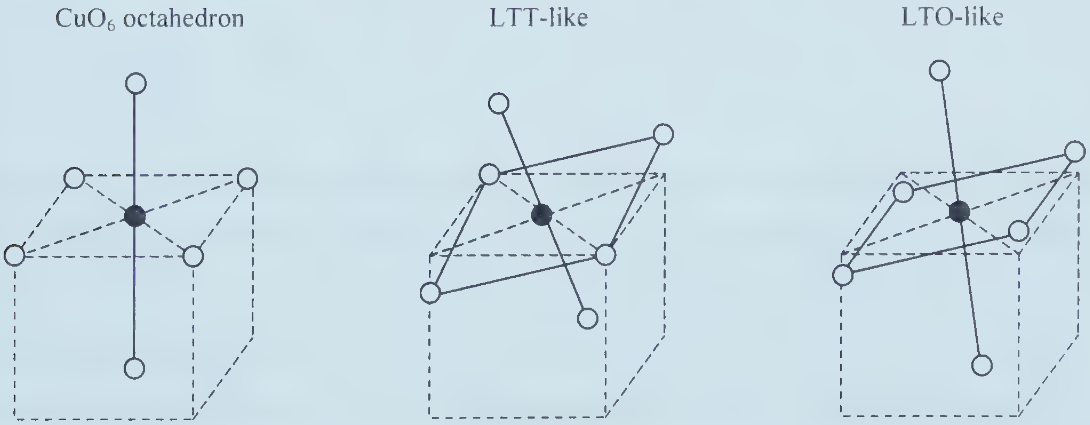

$CuO_6$ octahedron LTT-like LTO-like

Fig. 1.8 Distortion of $CuO_6$ octahedra in the stripes. The shortening of Cu-apical oxygen distance happens in the LTT-like structure.

an AF insulator) and the long-range part of Coulomb interaction. This theory also explains the experimental observation of "flat bands" (nearly dispersionless states at the $E_F$) and "shadow bands" (see the pervious section). However, the driving force for superconducting coherence is still under debate. It could result from stripe correlation through direct Cooper pair exchange between the stripes [59]. Interestingly, this model made many predications such as: $T_c = 569/l$ ($l$ is the inter-stripe distance in Å), $H_{c2} \propto 1/l^2 \sim Tc^2$ and $H_{c2} \propto x^2$ for $La_{2-x}Sr_xCuO_4$, $\xi_s \sim l$, and temperature-dependence of resistivity. It also proposed the existence of normal-state electron pairing in the stripes, without phase coherence, since they are of different origins. The pseudogap was also accounted for in this picture.

Since the transition into the stripe phase significantly changes the electronic structure and breaks the crystal's fourfold rotational symmetry, it should have dramatic influence on many physical properties. Moreover, the stripes are charged and are thus easily pinned by disorder. Indeed, experimental results have been accumulated in favor of this scenario. The neutron scattering data from $La_{2-x}Sr_xCuO_4$ family (and $La_{2-x}Sr_xNiO_{4+x}$) showed evidence of charge and spin orderings [60]. Supporting results also come from muon spin relaxation (μSR) [61] and X-ray diffraction [62] for the same La-series of materials. Following this route, the "1/8 puzzle", i.e. the suppression of superconductivity in $La_{2-x}M_xCuO_4$ at $x \approx 1/8$ (M = Ba) and 0.115 (M = Sr), was interpreted as being originated from the pinning of the dynamic stripe correlations on distortions in the $CuO_2$ plane. In Bi-2212, the APRES studies also revealed features related to fluctuating charge stripes [63]. A modified version of this model proposed an anharmonic 1D modulation of the $CuO_2$ plane [64, 65], consisting of alternated stripes with LTO- and LTT-like distorted lattices (Figs. 1.7 and 1.8). Electron gas condenses into the LTO-stripes, whereas polarons order in linear arrays in the LTT-stripes below a characteristic temperature $T^* \sim 1.4T_c$. The pairing mechanism rests in the interaction of these two components which satisfy a resonant condition: $k_{Fy} \sim 2\pi/L$, where $k_{Fy}$ is the Fermi wave vector normal to the stripe direction and $L$ is the width of LTO-stripes (2D Fermi liquid). In the case of Bi-2212, $L \approx 14$ Å and $W \approx 11$ Å at $T < T^*$. Such an ordering should influence the transport properties of the material, and $T^*$ seems to coincide with the temperature of spin gap opening.

As we can see from the above discussions on the microscopic aspects of the high-$T_c$ cuprates, while the crystallographic knowledge is relatively clear, the electronic and magnetic structures (and related dynamical processes) are very complicated and not fully understood. A few promising high-$T_c$ theories had been "condensed" which covered almost all the ingredients available from experiment, and it may not be surprising that one or some of them will eventually become "the" theory.

## 1.4 Carrier doping

The doping of charge carriers (holes or electrons) in cuprates is crucial in rendering various material properties. The parent compounds are antiferromagnetic insulators. Upon addition of charge carriers, they become superconducting at low temperatures. Carrier doping can be achieved by two ways: changing oxygen stoichiometry or adding metals (such as Pb or Y). The chemical composition of high-$T_c$ cuprates can be represented by a general formula, $(Ln_{1-x}M_x)_{n+1}Cu_nO_{3n+1-m}$, where Ln is a trivalent rare-earth ion, e.g. Y, and M is a divalent alkaline ion such as Ba, Sr, or Ca. $n$ is the number of $CuO_2$ planes and $m$ denotes the oxygen vacancies. Since copper can have 4 to 6 oxygen coordinations to form $CuO_4$ squares, $CuO_5$ pyramids and $CuO_6$ octahedra, a large number of perovskite-like structures with oxygen deficiency can be synthesized from these "building blocks". In these compounds, the copper is usually oxidized in a state of $Cu^{p+}$ with $0 < p < 0.4$, the value of $m$ is thus related to the concentration $x$ of divalent ions M. According to the doping status, a cuprate can achieve three doping regimes: optimal, under- and over-doping. The superconducting transition temperature reaches the maximum value in the optimal doping state, which has *universally 0.2 holes per Cu site*.

In $La_2CuO_4$, holes are created in the $CuO_2$ sheets by substituting lower-valence cations (such as $Sr^{2+}$ and $Na^+$) for $La^{3+}$. It is also possible to oxidize the $CuO_2$ planes by excess oxygen, i.e. $La_2CuO_{4+\delta}$, through annealing. $La_{2-x}Sr_xCuO_{4+\delta}$ has the highest $T_c$ = 40 K in this family when $x = 0.15$. When the doping is near 1/8, $La_{2-x}M_xCuO_{4-\delta}$ (M = Sr or Ba) shows anomalous transport properties: local minimum of $T_c$ and insulating behavior as $x$ is close to 0.125. This is the well known "1/8 puzzle". The origin of these

anomalies may come from commensurate charge and spin orderings as suggested by various theories and experimental results [60, 66, 67].

The most significant macroscopic effects of doping on superconducting properties of cuprates include dependence of transitional temperature $T_c$ upon the doping level and pseudogap behavior in underdoped samples. The experimental studies on the former had successfully built up reliable empirical relations, whereas the pseudogap concept is still under debate in terms of theoretical scenarios and interpretation of experimental data. For Bi-series cuprates, which are the subjects of the present work, a consistent $T_c$-$p$ (hole concentration) relation had been established [68]:

$$\frac{T_c}{T_{c,\max}} = 1 - 82.6(p - 0.16)^2, \tag{1.4}$$

where $T_{c,\max}$ is the maximum $T_c$ at optimal doping: ~ 90 (130) K for Bi-2212 (Bi-2223). This equation is plotted in Fig. 1.9. Similar dependence exists for other series of cuprates with different parameters. One difficulty involved in applying this elegant relation is the precise determination of oxygen concentration (and $T_c$). Usually it is evaluated by wet chemistry method [69] or from empirical relation between thermal annealing temperature and oxygen partial pressure [70].

Also shown in Fig. 1.9 is the doping dependence of $T^*$ (pseudogap opening temperature), which shows a trend of increasing with underdoping level. However, a consensus on this issue has not yet been achieved both in experimental observations and theoretical models: possible extension of the pseudogap into the overdoped regime, saturation of $T^*$ with underdoping, etc. To clarify such controversies, experiments with precisely controlled oxygen content are necessary. Oxygen doping is very tricky, different results easily arise even the samples are treated under the same conditions. For this matter, repeatability and comparison among samples on run to run basis are important. A correlation between $T_c$ and optimum doping can be understood in terms of in-plane bond length dependence upon carrier density [71]. The $CuO_2$ layer loses electrons through oxidation. As the hole density increases, the in-plane Cu-O bond length ($r_{\text{cu-O}}$) is shortened. $r_{\text{cu-O}}$ is also controlled by steric strain associated with the cations located at the 9-coordinate sites adjacent to the $CuO_2$ layers. When the sizes of these cations increase, $r_{\text{cu-O}}$ increases to reduce the steric strain. With various hole

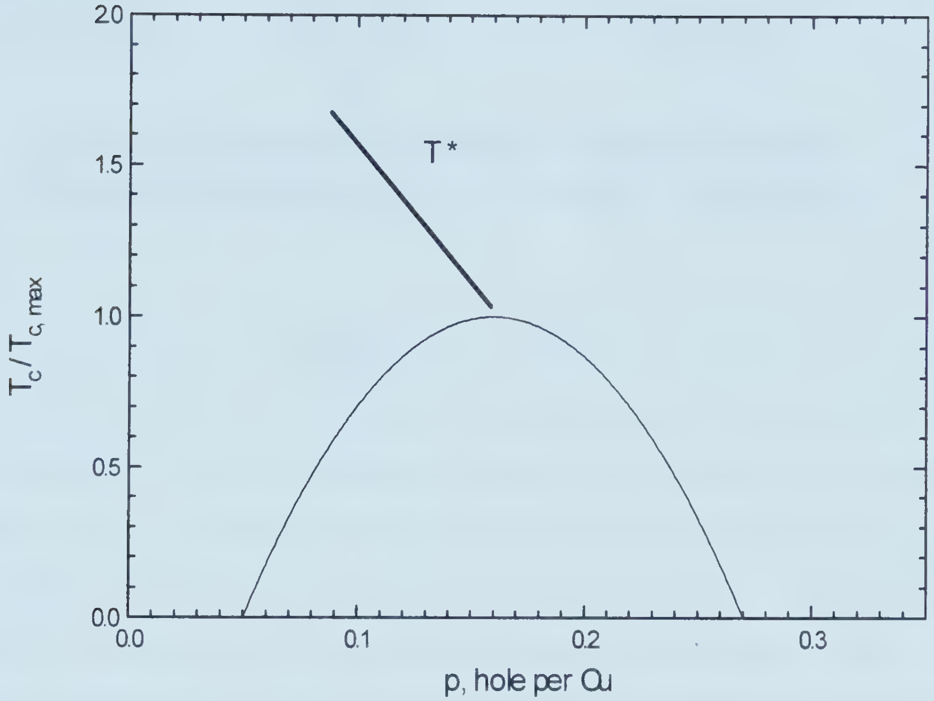

Fig. 1.9 Pot of the parabolic Eq.(1.4). Also shown (schematically) is the pseudogap opening temperature $T^*$, which is only one of the many versions on this topic.

doping. $T_c$ vs. in-plane $r_{\text{cu-O}}$ shows a maximum $T_c$ at an optimum hole density. The apical Cu-O distance is also a crucial parameter, which is involved in the charge transfer process to or from the $CuO_2$ planes. This parameter is related to oxygen deficiency, and hence $T_c$, in that $T_c$ decreases with the increasing apical $CuO_2$ length [72].

Chapter 2

# BSCCO Whiskers: Single Crystal Growth, Thermal Annealing, and Sample Preparation

The materials used in the present studies are BSCCO (both $Bi_2Sr_2CaCu_2O_{8+\delta}$ and $Bi_2Sr_2Ca_2Cu_3O_{10+\delta}$) single crystals. Shortly after the discovery of Bi cuprates [73, 74], Jung and Franck [75, 76] in this Department succeeded in growing single crystalline Bi-2212 whiskers by a sintering method and studied the superconducting transition and elastic properties. The crystals are known as "whiskers" because of their micrometer-sized needle-like shapes, with very high crystalline quality and perfect surface morphology. Occasionally in samples, no twin boundary or stack fault dislocations can be found by scanning and transmission electron microscopy (SEM and TEM). It is even believed that the $CuO_2$ planes are continuous throughout the length in the best-quality crystals. Another important material feature is that all the growth steps, if present, are parallel to the longest dimension (*a*-axis) and continuous throughout a whisker. Obviously, a current flowing in this direction will hardly encounter any dislocation or grain boundary. Therefore, the BSCCO whiskers are ideal for physical property studies, especially transport measurements. The present work was based on the existing expertise on this topic and an extension by adopting other techniques of whisker growth.

## 2.1 Growth of Bi-2212 whiskers

The crystals were grown by a sintering method originated from Jung *et al.* [75]. Raw chemicals of $Bi_2O_3$, Sr-oxalate ($SrC_2O_4$) or $SrCO_3$, Ca-oxalate, and CuO are mixed with various metal ratios, typically Bi : Sr : Ca : Cu = 2.4 : 1.5 : 1.0 : 1.8. The powder (~ 25 g) is thoroughly ground and then pressed into a pellet of 1 inch diameter under a pressure of about 150 bar. Before sintering, the pellet is carved into a "cup" (Fig. 2.1) for the purpose of increasing surface area and possible enhancement of vaporized

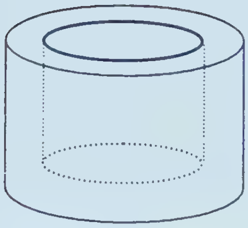

Fig. 2.1 A BSCCO pellet carved into a cup.

elements' concentration in the cup during growth. A "lid" plate pressed from the same powder was also made in hope to enclose a chamber of higher vapor concentration, but without noticeable effect. The pellet is sintered in air at ambient atmosphere at 840 – 870°C for 48 – 100 h. Detailed growth conditions are summarized in Table 2.1. Whiskers grow on the inner surface of the pellet and in the crevices as the pellet usually cracks during sintering. Typical dimensions of the BSCCO whiskers are: 2 - 5 mm ×5 μm × 0.5 μm. The crystalline axes *a*, *b* and *c* align with these three dimensions. This fact makes it very easy to apply the magnetic field along the axes in anisotropy studies.

Table 2.1 Typical growth conditions for Bi-2212 and Bi-2223 whiskers.

| Metal ratio (Bi:Sr:Ca:Cu) | Growth temperature (°C) | Growth time (hours) | Al content (wt.%) | Grown whiskers |
|---|---|---|---|---|
| 2 : 1.68 : 1 : 2 | 870 | 100 | 0 | 2212 |
| 4 : 3 : 2.6 : 5 | 860 | 60 | 0 | 2212 |
| 2 : 1.68 : 1 : 2 | 870 | 100 | 0 | 2212 |
| 4 : 3 : 2.6 : 5 | 860 | 72 | 10 | 2223 |
| 2 : 1.9 : 2.2 : 3 | 870 | 100 | 5 and 10 | None |

Figures 2.2–4 show SEM pictures of two Bi-2212 whiskers grown by this method. These three cases represent the overall surface structure of the BSCCO whiskers. As can be seen in Fig. 2.2, the crystal is perfect without any twin boundary or growth steps throughout the whole length. This sample (BSCCO36) gives very unusual flux flow resistance: depinning happens at extremely low temperature ~5 K! It is obviously a superclean crystal in terms of flux dynamics terminology. More will be discussed in Chapter 9.

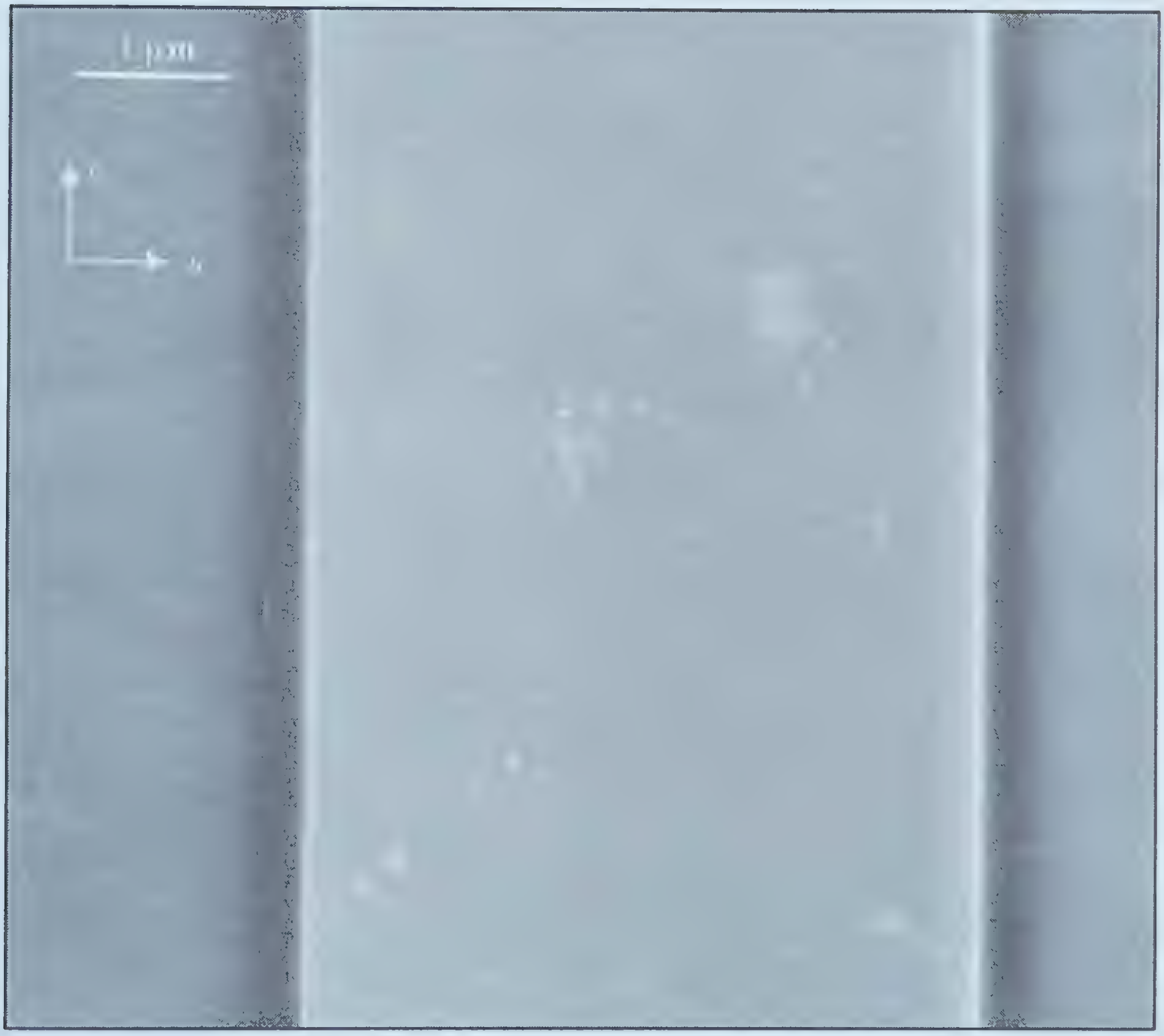

Fig. 2.2 SEM image of a perfect Bi-2212 whisker. The view is *ab*-plane along the *c*-axis. Dirt particles attracted onto the surface are also visible.

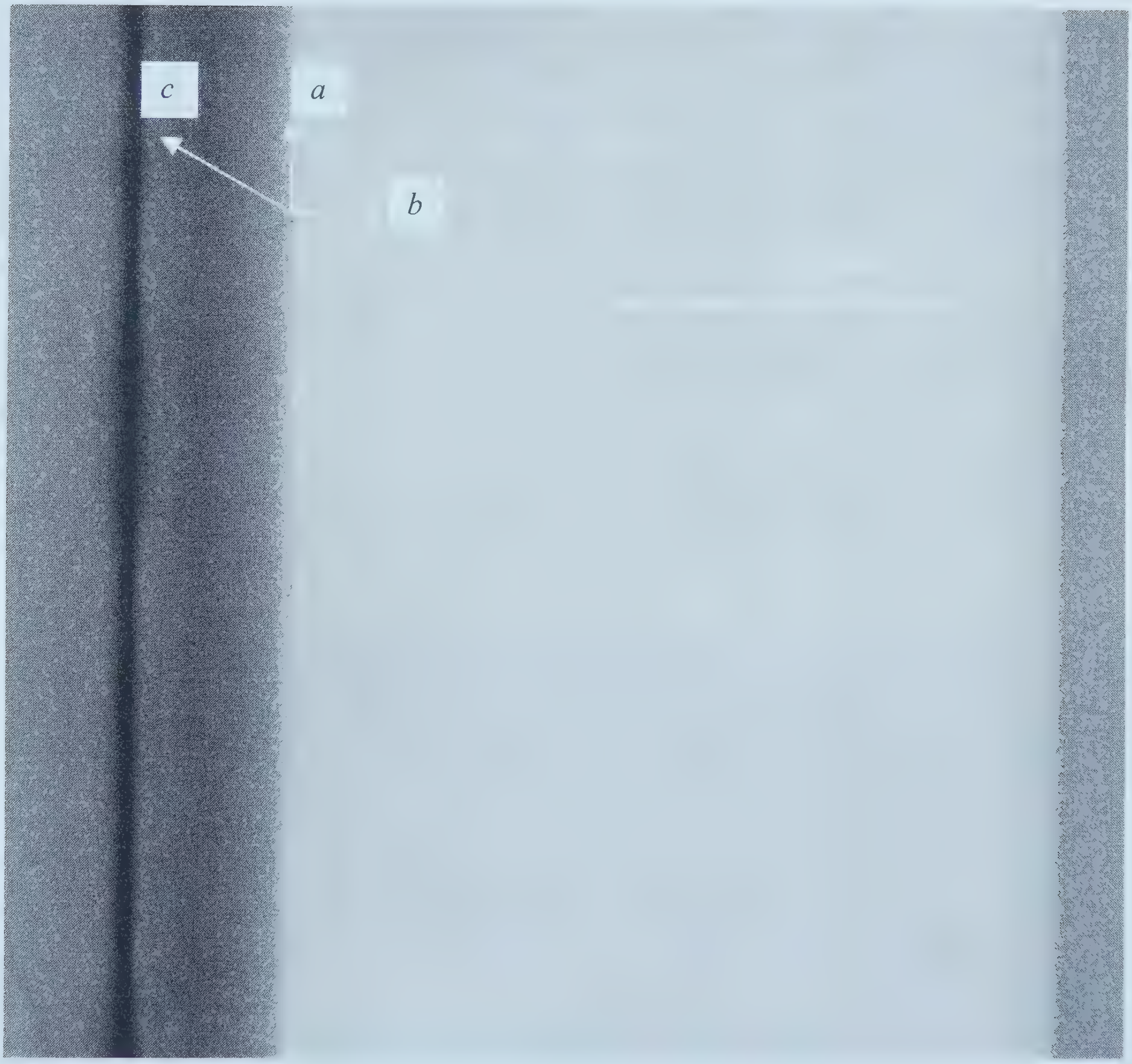

Fig. 2.3 Tilted view of an as-grown Bi-2212 whisker. Note the sharp edges. A terrace runs in the center of the whisker. No difference in the chemical composition on both sides was found.

Figure 2.3 is a tilted view of another whisker showing the sharp natural edges of the crystal. A growth step in the center runs along the length. Fig. 2.4 shows more growth steps near the edge. Timofeev *et al.* [77] systematically studied the growth defects in Bi-2212 whiskers, and showed that such steps approximately have a height of 50 Å, i.e. about the double unit cell parameter $c \approx 30.6$ Å. Twinning is relatively rare in the whiskers. Other defects include dislocations and superstructure defects associated with the perovskite-like structure. Fig. 2.4 shows a whisker with two parallel growth steps along the edge. Occurrence of more growth steps is not common in our whiskers. The lattice constants $a = 5.40$ Å and $b = 5.41$ Å from TEM diffraction measurement. Previous works done by Jung *et al.* [76] determined $c = 30.9$ Å. The common incommensurate modulation along the *b*-axis was also observed from electron diffraction patterns.

To change the doping level, we used thermal annealing in a flowing gas (nitrogen, argon, or oxygen). The temperature was 450°C and the time varied from 2 to 8 hours.

Fig. 2.4 Growth steps (indicated by the arrows) near the edge of a Bi-2212 whisker.

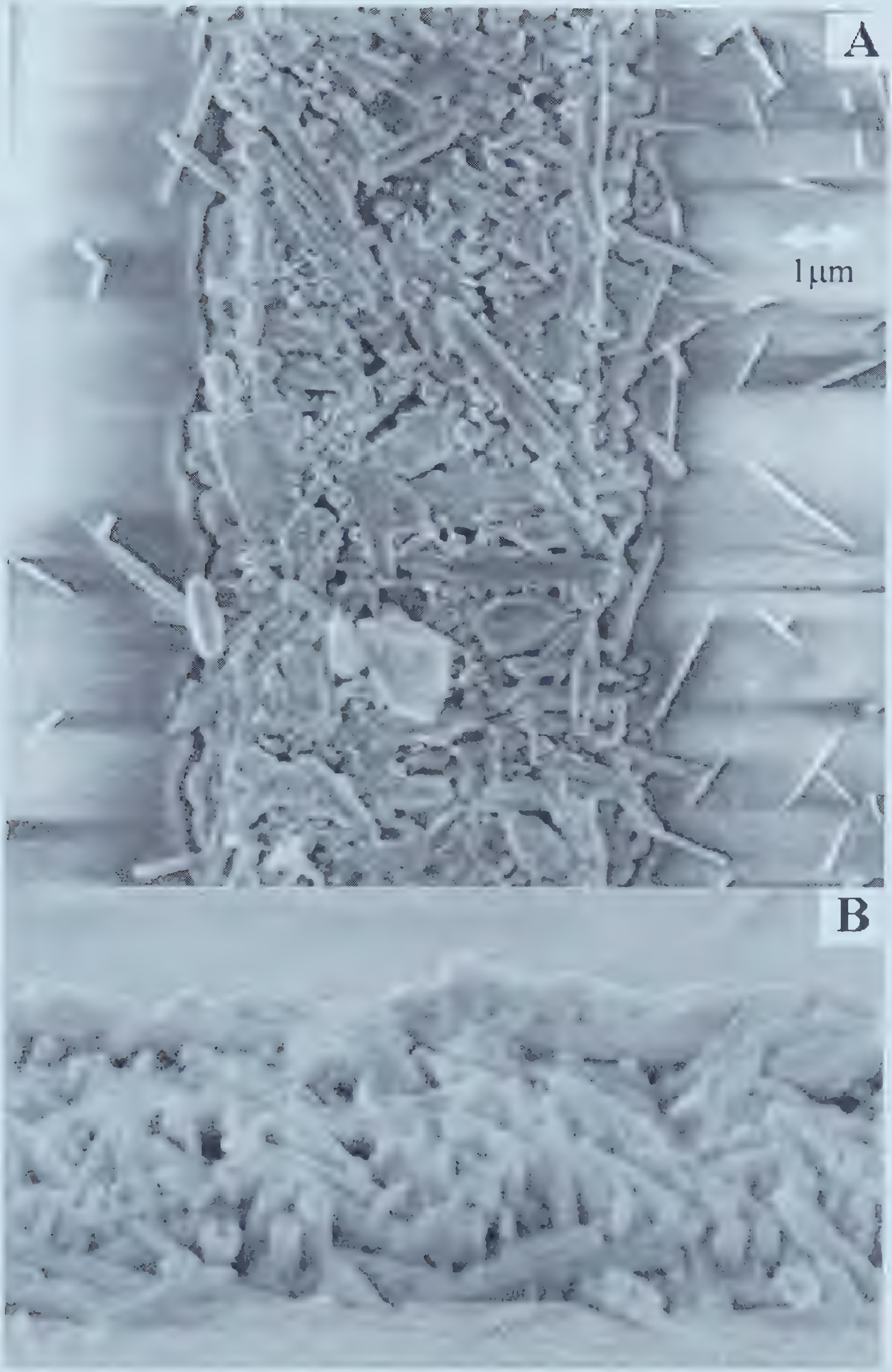

Fig. 2.5 (A) Damage caused by thermal annealing the whisker. (B) is a side-view (Thickness ~ 2.2 μm).

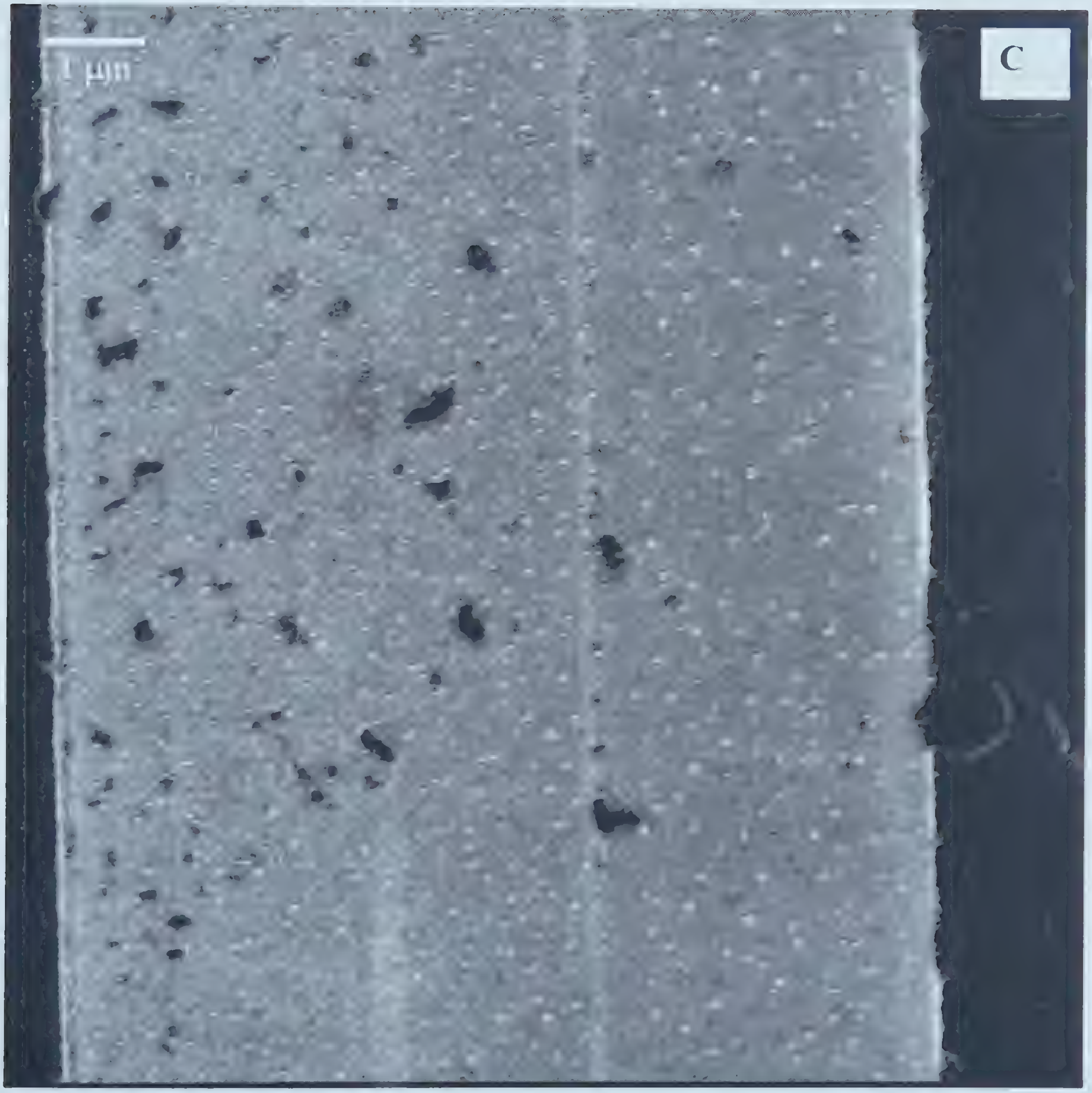

Fig. 2.5C Surface degradation caused by thermal annealing under typical conditions: 450°C and 4 h. The effect is significant in comparison with the as-grown surface morphology.

Higher temperature is likely to cause damage on the sample, as shown in Fig. 2.5. Even under the normal annealing conditions, the surface morphology will suffer degradation. It becomes coarse due to partial evaporation at the surface, as shown in Fig. 2.5C. This could affect flux line pinning environment, which will be discussed in the topic on flux dynamics.

The oxygen content in the sample depends on annealing temperature, time, and, more strongly, on oxygen partial pressure. Annealing at 1 atm and a constant temperature (450°C) will eventually saturate the doping level after about 4 hours. The as-grown Bi-2212 whiskers are consistently overdoped, whereas the Bi-2223 phase is underdoped, which agrees with other studies [68]. The present annealing treatment resulted in a low $T_c \sim 63$ to 70 K on both sides of doping and a maximum $T_c \sim 85$ K close to the optimal doping (refer to Fig. 1.9).

## 2.2 Growth mechanism

Basically there are two models for BSCCO whisker growth: tip versus root growth. The former mechanism was first proposed for Si whiskers [78] and was applied to BSCCO whiskers [79]. According to this model, small liquid droplet first forms on the surface of the base material, it then collects elements from the vapor. A whisker continues to grow by precipitation from the droplet at the tip. Such a picture is unlikely the case for the growth scheme used in this work. Because we never found any sort of droplet solidification at the tip of a whisker. The whiskers also do not join together during growth even though a dense forest of them grows out of a pellet's surface.

A modified picture is based on screw dislocation growth [80], in which vaporized atoms deposit on the screw dislocation at the surface of the base pellet, and provide growth steps. Whisker growth is sustained by continuous deposition of atoms from the vapor onto the edge of the whisker and diffuse to the tip. This seems to be the case for our whisker growth. In fact, growth steps on the edge are commonly seen on the whiskers, and more important, this mechanism assumes *no need of Al* in growth. Al is thought to greatly enhance BSCCO whisker growth speed (further discussed below). As

a result, growth by such scheme yields low speed and output. However, the crystal quality is very high.

A third growth mechanism was proposed by Matsubara *et al.* [81]. In this model, whisker grows from the root, rather than at the tip, out of a small "pool" of Bi-rich molten liquid. A prerequisite for such a growth is the presence of Al, either from the crucible or deliberately added into the starting material. Al doping resulted in the formation of a complex Al oxide (BiSrCaAlO) near the surface, which acts as a "rigid skeleton". The small pools form in this skeleton which acts as micro-crucibles. Further study by Lee *et al.* [82] differs slightly from this picture, in that the formation of BiSrCaAlO lowers the melting point of Bi-2212 phase and enhances the formation of liquid pools. This causes fast growth speed and large throughput. In our growth with doped $Al_2O_3$, sharp contrast results were obtained with respect to Al-free growth (see below).

## 2.3 Growth of Bi-2223 whiskers

Much effort has been devoted to growth and physical properties of $Bi_2Sr_2CaCu_2O_{8+\delta}$ (Bi-2212) whiskers [68, 76, 83-86], however, relatively less work was done on the $Bi_2Sr_2Ca_2Cu_3O_{10+\delta}$ (Bi-2223) system due to the difficulty in material preparation. Ordinary methods for growing Bi-2223 phase include annealing by starting from Bi-2212 [87,88] or by Pb doping [89, 90]. Such schemes are effective in material growth, but generally result in unavoidable mixture of both 2212 and 2223 phases, and undesirable Pb doping in the crystal. Pb-free growth was also explored with various results [91].

In BSCCO whisker growth process, the role of aluminum is believed to be crucial. For this reason, a few groups had studied the effects of $Al_2O_3$ doping in the starting materials [82, 92]. In most cases, whisker output and growth speed were significantly enhanced compared with Al-free growth, although at the price of crystal quality. More important, aluminum seems to only assist growth process without entering the crystals. Previous studies on this issue reported growth of Bi-2212 whiskers [82, 92]. Following

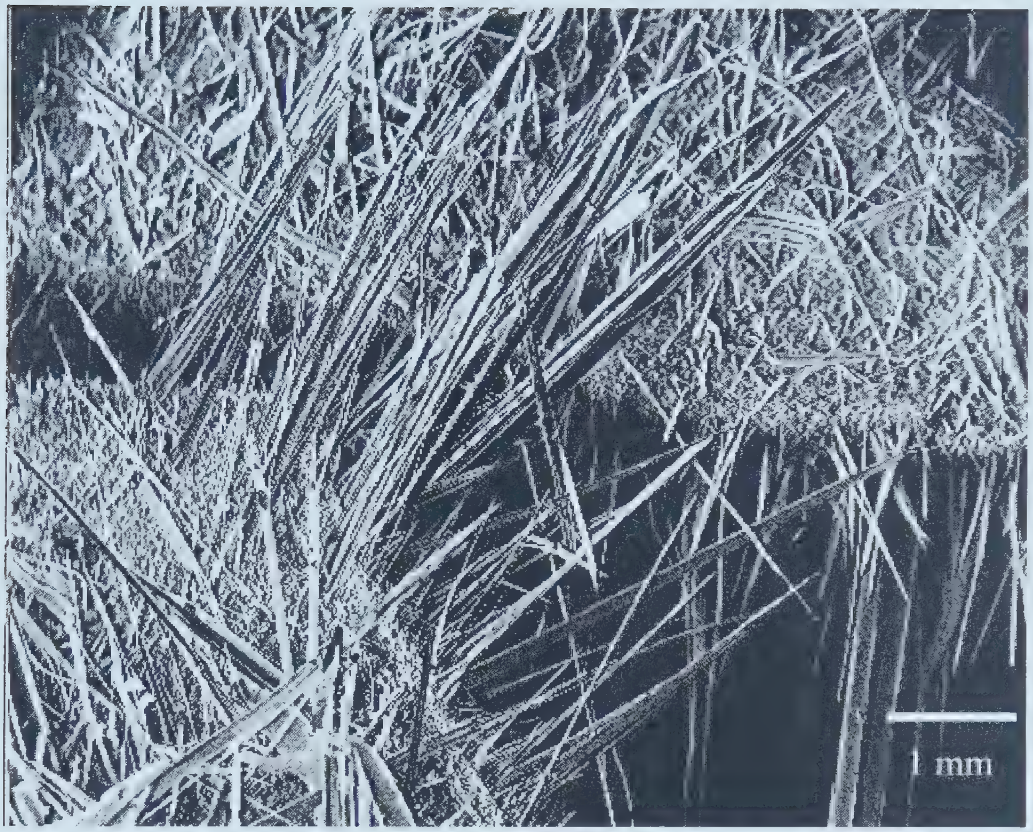

Fig. 2.6 Whisker growth with $Al_2O_3$ doping. Growth speed is profoundly enhanced compared with Al-free growth. The crystals are also highly twinned.

the similar scheme, we had succeeded in growing Bi-2223 whiskers with very high output and good material quality. Although large size whiskers are heavily twinned as usual, the thinner ones (of a few millimeters long) have smooth surfaces. Various characterization techniques also confirmed undetectable content of Al in the whiskers. Moreover, in resistivity measurement, a novel anomalous upward deviation from the linear-$T$ relation appeared below $T^* \sim 250$ K, which might be related to structure transformation or lattice distortion. We also studied the effects of thermal annealing on $T_c$ and normal-state resistivity.

The preparation of Bi-2223 whiskers is detailed below. Chemical powders of $Bi_2O_3$, Sr-oxalate ($SrC_2O_4$), Ca-oxalate and CuO were mixed and thoroughly ground. Typical metal ratio in the starting mixture was Bi : Sr : Ca : Cu = 4 :3 : 2.6 : 5, other ratios were also tried (Table 2.1) with varied results. Before grinding, we added 5 to 10 wt.% $Al_2O_3$

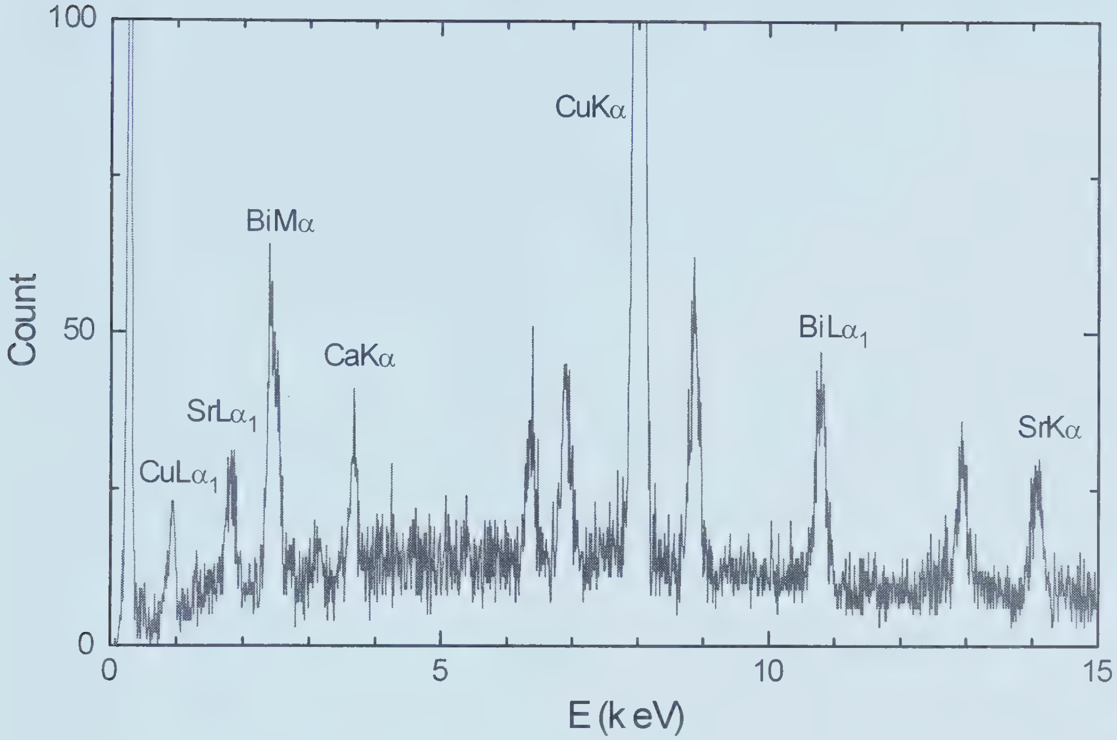

Fig. 2.7 Typical EDX spectrum of a Bi-2223 whisker grown by Al-doping method. No peak structure corresponding to aluminum contamination is identifiable in the spectrum. An upper bound Al-concentration was estimated from the background noise.

into the mixture. The thoroughly ground powder was first melt in an alumina crucible at 1050 °C for 30 minutes, then poured and pressed on a liquid-nitrogen-cooled copper plate; The resultant glassy plates were annealed in air at temperatures between 825 - 860°C for 24 to 100 hours, followed by oven cooling. Large amount of whiskers grew on the surfaces of the plates, with typical dimensions of 1-6 mm × 10 μm × 1 μm (thickness). An extremely fast growth result is imaged in Fig. 2.6. This is in contrast to the growth by the non-aluminum sintering method described in Sec. 2.1. In the Al-free method, long whiskers (~3 mm) were also obtained, but the output and growth speed were far less than Al-doped cases. On the other hand, whiskers from Al-free pellets are long perfect tapes with rectangular cross-section, whereas the large-size whiskers grown on the Al-doped plates have rough morphology, possibly due to different growth

mechanisms. In our measurements, we carefully selected small whiskers with good surface conditions under optical microscope. SEM imaging of these samples also indicated smooth morphology and uniform composition. Accurate sample dimensions were determined by this method.

One noticeable difference, in the present work, between growth with Al- and non-Al doping is that the former consistently produced the Bi-2223 crystals ($T_c$ ~110 K), and the latter always yielded the Bi-2212 phase ($T_c$ ~76 K). This result was not reported in the related studies [82, 92]. The reason for the distinct growth may lie in the different metal ratios, as well as the concentration of Al. The Bi-2223 whiskers were examined by electron microprobe and energy dispersion x-ray spectroscopy (EDX). No peak structure corresponding to Al was identifiable in the spectrum, which agrees with the finding of other groups [82, 92]. A typical EDX calculation using the peak height ratio of background noise to Ca$K\alpha$ gives an upper bound of Al concentration of Al/Ca ~ 0.03. This value is in contrast to the large amount of $Al_2O_3$ added in the starting mixture. Al is believed to mainly assist the unique whisker growth process without entering the crystal. More details were discussed by other groups [82, 88]. This also complies with the usual $T_c$ value, which could have been suppressed by impurity doping, although the exact effect of Al on $T_c$ is not very clear. A typical EDX spectrum is shown in Fig. 2.7.

## 2.4 Sample preparation

Transport measurements were made by the standard four-wire method. All the samples were otherwise randomly picked up from base pellets except care was taken to select tiny-size whiskers with perfect surfaces under optical microscope. The BSCCO whisker was laid on a glass substrate followed by slightly wetting the whisker with methanol. This helps flatten the tiny whisker and firmly fastens it onto the substrate thanks to electrostatic force. Silver leads were sputter-deposited onto the whisker through a mask. Thermal annealing in flowing nitrogen or argon (450°C for 4 h) after sputtering can greatly reduce electrical contact resistance from $10^{-1}$ to $10^{-6}$ $\Omega cm^2$ for a

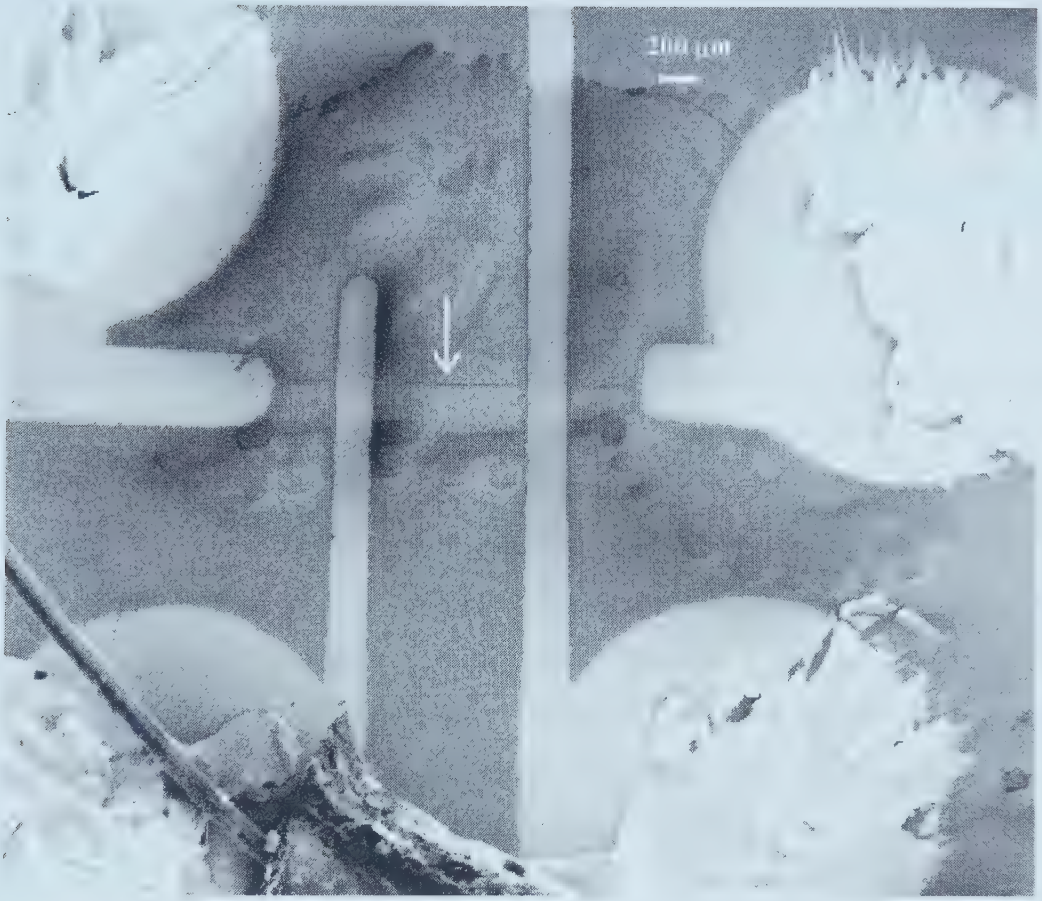

Fig. 2.8 A four-wire configuration for transport measurement. The electrical contacts are magnetron-sputtered silver. Copper wires are attached to the circular silver pads with indium. The arrow indicates the thin whisker.

contact area of 10 × 100 $\mu m^2$. The high contact resistance is caused by the insulating Bi-O layer at the surface. We tried directly applying silver epoxy on the whiskers without any success. The resistance input was always too high for the digital voltmeter. Water-cooling was also used to reduce sample heating during magnetron sputtering.

DC current of 0.5 μA (~ 10 $A/cm^2$) was driven along the length (*a* axis within the *ab* plane) of the whisker, voltage was measured by a nanovoltmeter (Keithley 181). Fig. 2.8 shows such a four-wire configuration, in which the arrow points to the whisker.

## Chapter 3

# The Normal State of High-Temperature Superconductors

The normal state of high-temperature superconductors has been under intensive study for its peculiar properties. Like the general studies of phase transition, in superconducting transition, understanding one phase is helpful for studying the other in the transition. More important, both experiment and theory have shown anomalous properties in the normal state and crucial connections to the superconducting state. Therefore, the study of the normal state is imperative to a solution of the high-$T_c$ superconductivity puzzle. This chapter outlines the most-updated normal-state anomalies, experimental techniques, and various theoretical models. In the next chapter, we present our experimental results that reveal very interesting new features of BSCCO single crystals.

## 3.1 Unusual normal-state properties

Compared with a normal metal, the cuprate exhibits a few unusual properties in the normal state such as anisotropy, pseudogap, and non-Fermi liquid behavior. Accordingly, many scenarios have been constructed to interpret these anomalies. Below is a summary of the major properties found in the normal state.

1. **Anisotropy**. One prominent feature of the high-$T_c$ superconductors is the anisotropic layered structure composing $CuO_2$ planes. The electrical conductivity within the planes is much higher than that in the perpendicular direction. The resistivity ratio, $\rho_c/\rho_{ab}$, can reach to the order of $10^5$ in strongly anisotropic BSCCO materials. This had led to the interlayer tunneling theory of high-$T_c$ superconductivity [93], which assumes that the blocking of $c$-axis conduction in the normal state provides the energy of superconducting condensation. In the superconducting state, the anisotropy is reflected

in the large difference of in-plane and out-of plane magnetic penetration, the anisotropy parameter, $\gamma = \lambda_c/\lambda_{ab} = \xi_{ab}/\xi_c$, is about 7 in YBCO and can exceed 200 in BSCCO.

2. **Anomalous transport properties**. The temperature dependence of resistivity of cuprates is peculiar in term of standard Fermi-liquid theory [94, 95]. In optimal doping regime, cuprates have linear-$T$ resistivity over a wide temperature range from $T_c$ up to 1000 K [96, 97], where a $T^2$ behavior is expected. In the overdoped samples, resistivity takes the form

$$\rho = \rho_0 + AT^p, \tag{3.1}$$

with $1 < p \leq 2$, while in the underdoped regime, $\rho$ is linear in $T$ at high temperature and starts to deviate downward below some characteristic temperature $T^* \sim 200$ K or higher. A typical doping dependent $\rho$-$T$ result in Bi-2212 is shown in Fig. 3.1 [98]. The

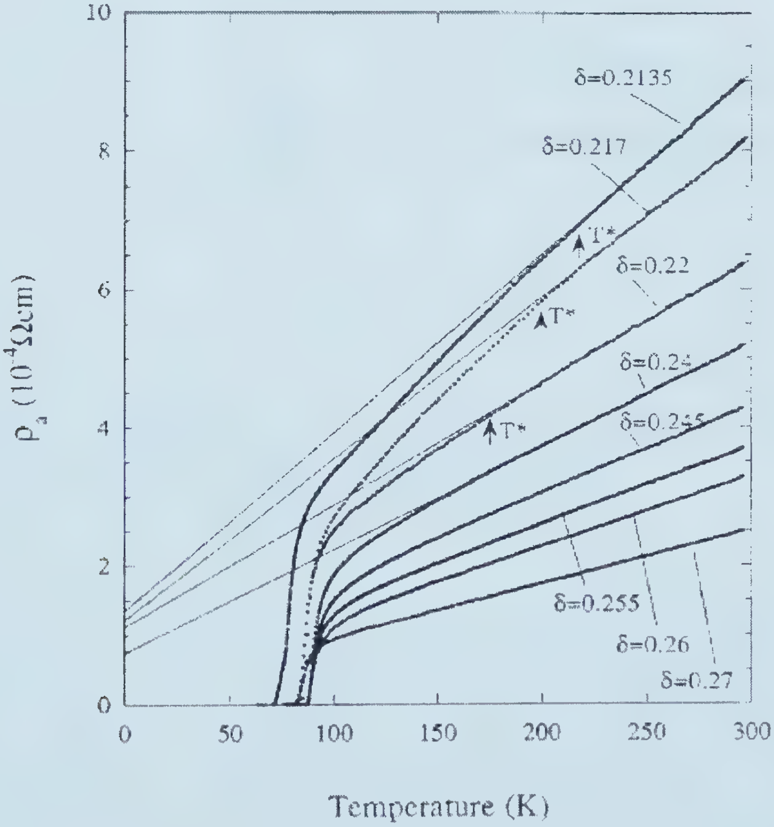

Fig 3.1A Temperature dependence of in-plane resistivity in various doping levels [From Ref. 98 with permission. Copyright 1997 by *The American Physical Society*].

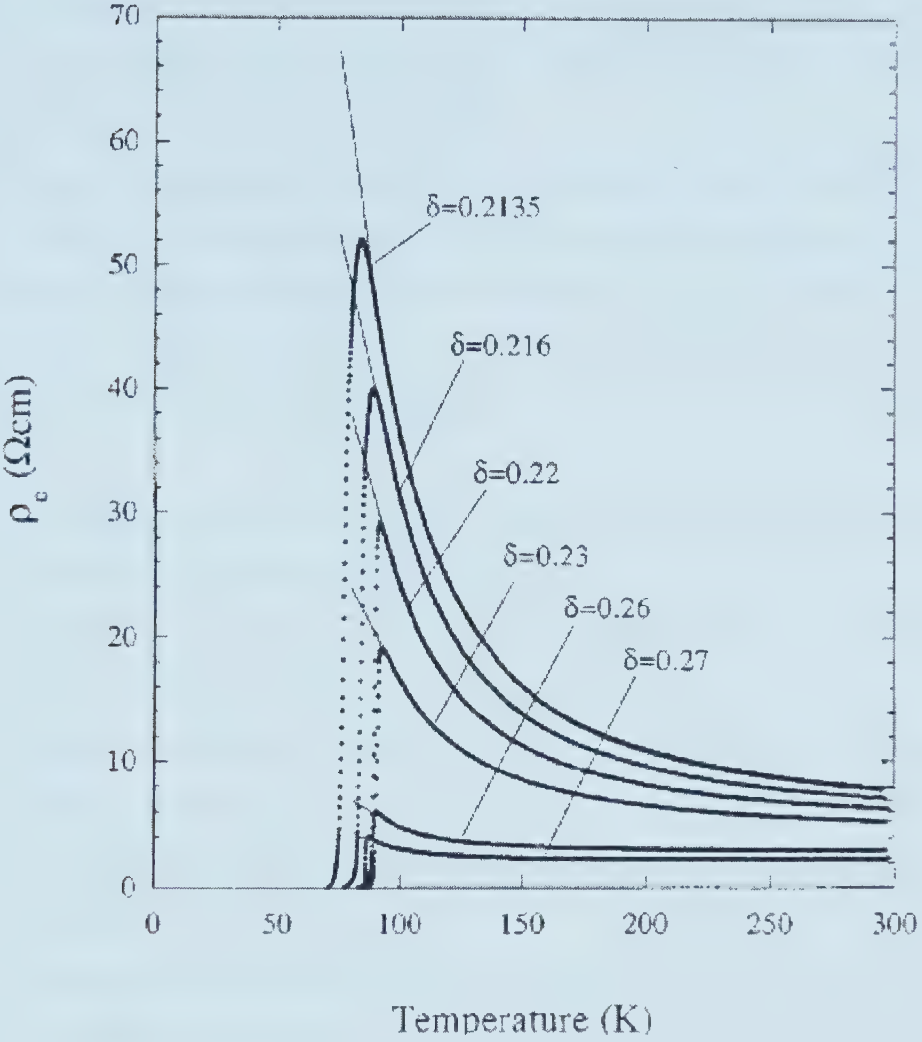

Fig. 3.1B Dependence of *c*-axis resistivity on oxygen doping for samples of $Bi_2Sr_2CaCu_2O_{8+\delta}$ [From Ref. 98 with permission. Copyright 1997 by *The American Physical Society*].

deviation from linear $\rho$-$T$ was believed to be a manifestation of spin-gap opening [97, 98], and has been widely observed in underdoped cuprates. As oxygen doping is further decreased, carrier localization happens at lower temperature and resistivity rapidly increases. For $La_{2-x}Sr_xCuO_4$, a metal-insulator transition takes place for $x \approx 0.07$ [Ref. 96]. The resistivity around the transition ($\rho_{ab} \approx 400$ μΩcm) is roughly the sheet resistance ($4e^2/h$) for a disorder-driven 2D superconductor-insulator transition.

In Hall effect measurement, a $1/T$ dependence of the Hall coefficient $R_H$ is found in optimally doped samples. Deviation from this relation appears below $T^*$ when the

sample is underdoped, and $R_H$ shows a peak at lower temperature. The origin for this anomaly is not fully understood. Thermopower data also exhibits spin-gap-related anomaly where the effect is enhanced below $T^*$.

3. **Spin gap (or pseudogap) phenomenon** As was mentioned in Chapter 1, spin gap refers to a reduction of density of states in the spin excitation spectrum, and is found to be a universal phenomenon of (at least) underdoped cuprates. Many experimental techniques were used to probe spin gap and related effects. Below is a list of these techniques and typical materials investigated:

- ***resistivity***: La-214 [96,99-102], YBCO [102-105,], $YBa_2Cu_4O_8$ (Y-124) [106], BSCCO [98,107,108], HBCCO [109].
- ***NMR***: La-214 [110-113], YBCO [111, 114-116], $YBa_2Cu_4O_8$ [116, 117], Tl-2212 [118], Hg-1201 [118], Hg-1223 [119].
- ***optical conductivity ($\sigma(\omega)$)***:Y-124 [120], Bi-2212 [121], $Tl_2Ba_2CuO_{6+\delta}$ [121], YBCO [120, 122].
- ***angle-resolved photoemission spectrum (ARPES)***: Bi-2212 [123-126], La-214 [127].
- ***neutron scattering***: La-214 [128], YBCO[50, 129, 130].
- ***tunneling***: Bi-2212 [131, 132].
- ***Raman***: YBCO [133], Bi-2212 [133].
- ***uniform susceptibility ($\chi_0$)***: La-214 [134, 135].
- ***other methods (thermopower, heat capacity, etc.).***

In NMR measurement, the antiferromagnetic Cu spin fluctuations enhance the strongly temperature dependent nuclear spin-lattice relaxation rate, $1/T_1T$. A decrease in $1/T_1T$ below $T^*$ signals the opening of a pseudogap in the low energy magnetic excitations. Yasuoka [136] proposed an activating type relaxation rate:

$$1/T_1T = (1/T_1T)_{CW}\,A\exp(-\Delta/k_BT), \tag{3.2}$$

with $\Delta/k_B$ = 145 K, and a linear hole density dependence of gap opening temperature: $T^* = 186 - 388\,p$, where $p$ is the hole number per sheet. Up to now, NMR data on BSCCO is unavailable.

ARPES results from Bi-2212, on the other hand, suggest that the pseudogap seems to be related to precursor pairing rather than being of magnetic origin [125]. Pseudogap in ARPES is identified as a separation of the spectrum's leading edge from the Fermi surface. It is noteworthy to mention that a recent photoemission study had put forward challenge to the interpretation of ARPES results. Joynt [137] pointed out that a photoelectron's energy may well be affected by the sample through "image charge" effect. The energy loss is important in low conductivity materials, which is the case for the *c*-axis of high-$T_c$ cuprates. It is not clear if this effect has any thing to do with the ARPES finding that the pseudogap size is almost independent of doping at least in the underdoped regime [100, 138, 139].

The spin-gap is closely connected to the individual $CuO_2$ plane, and is unlikely to depend on inter-layer coupling. The gap size is $2\Delta_0 \approx 50 - 60$ meV ($\Delta_0$ is the maximum d-wave gap). It is meaningful to compose a "universal" $T^*$-$p$ (doping level) phase diagram using data from as many cuprates as possible. This was partially done by a few groups, and their works are reproduced in Figs. 3.2-3.5. One can conceive the complexity of this issue by taking a glimpse of the various versions of the $T^*$-$p$ diagrams. These also reflect the diversity in theoretical understanding on this issue.

Currently, the controversy over pseudogap in the normal state focuses on the following aspects:

- The relationship between the pseudogap and superconducting gap. There is still debate on whether or not the pseudogap is a precursor of the superconducting gap. For example, from tunneling measurements on Bi-2212, Miyakawa *et al.* [143] claimed that the pseudogap evolves into the full BCS *d*-wave gap, whereas others proposed that the two gaps are irrelevant.
- Dependence of $T^*$ on doping level ($p$). $T^*$ is generally believed to be linearly dependent on $p$, as illustrated in these figures. $T^*$ drops with increasing hole density. It could reach $T_c$ at optimal doping (Fig. 3.2), where the pseudogap

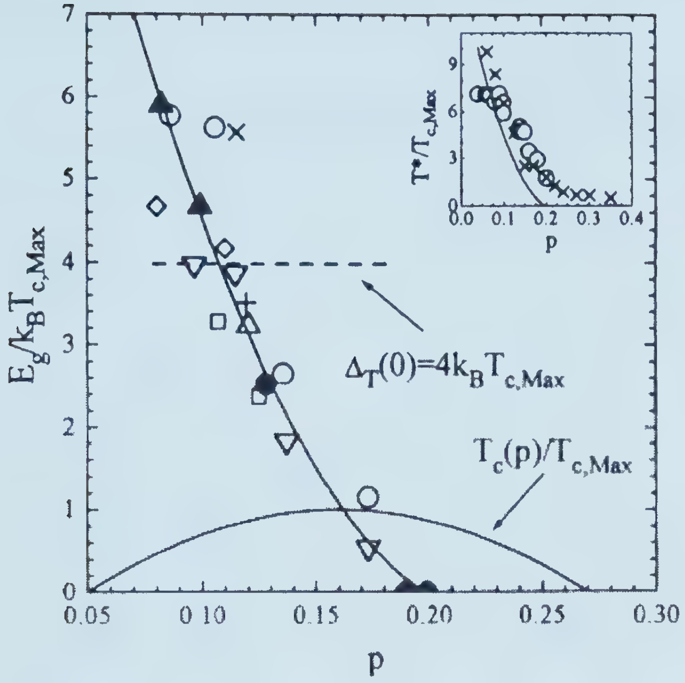

Fig. 3.2 Pseudogap size $E_g$ vs. hole density of various cuprates including single, double, and triple layer series. Inset is $T^*$-$p$ plot for La-214, where the solid curve is that in the main panel. $\Delta_T(0)$ is the zero-temperature total gap, which is assumed to be equal to a *d*-wave superconducting gap: $4k_BT_{c,\max}$, and doping independent across the underdoped region [From Ref. 140 with permission. Copyright 1997 by *The American Physical Society*].

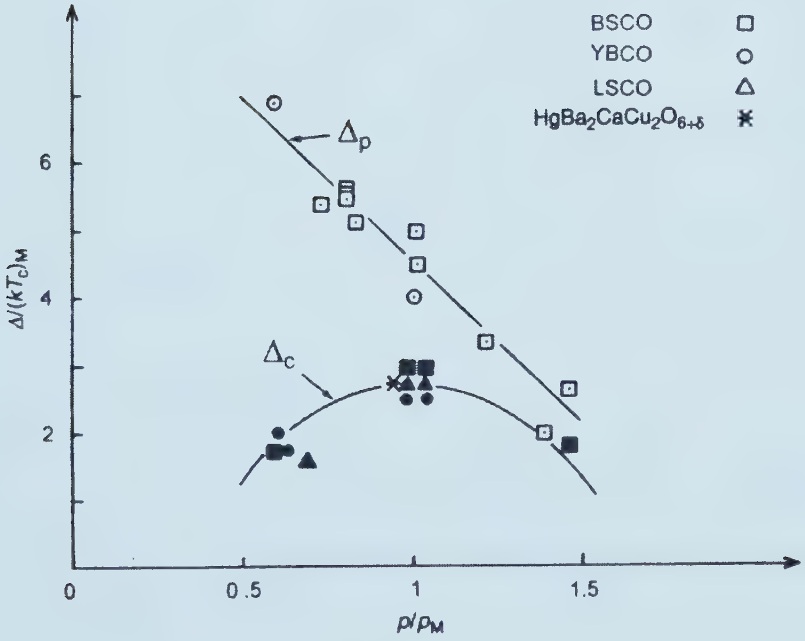

Fig. 3.3 A two-component scheme with $\Delta_p$ being the single-particle excitation energy and $\Delta_c$ the coherence energy range. Both energy scales merge in the overdoped regime, but separate in the underdoped side [From Ref. 141. Reprinted by permission from *Nature*. Copyright 1999 by *Macmillan Magazines Ltd.*]

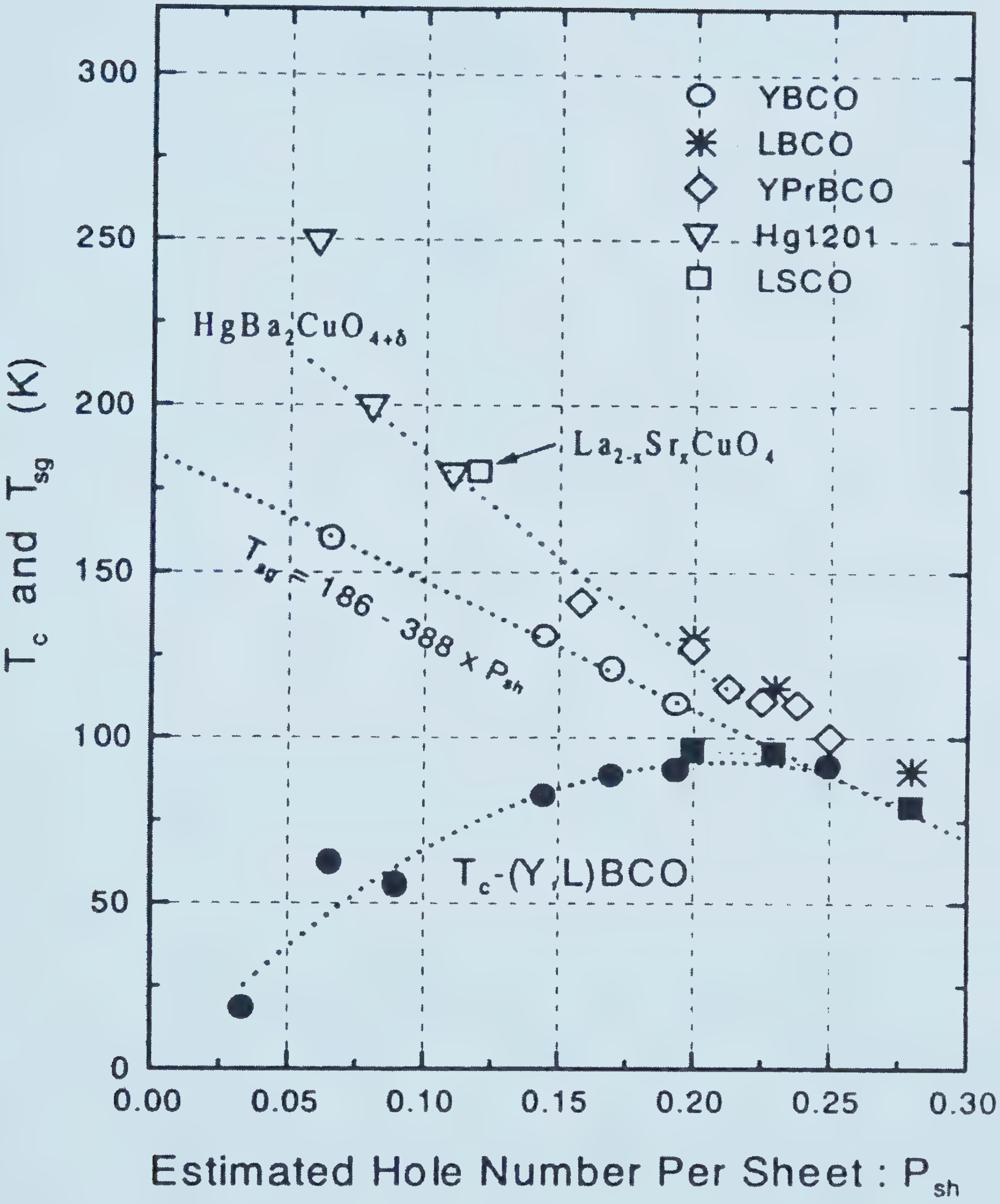

Fig. 3.4 Spin-gap phase diagram. Spin gap temperature $T_{sg}$ was defined from maximum $1/(T_1T)$, [From Ref. 136 with permission. Copyright 1997 by *Elsevier Science B.V.* ].

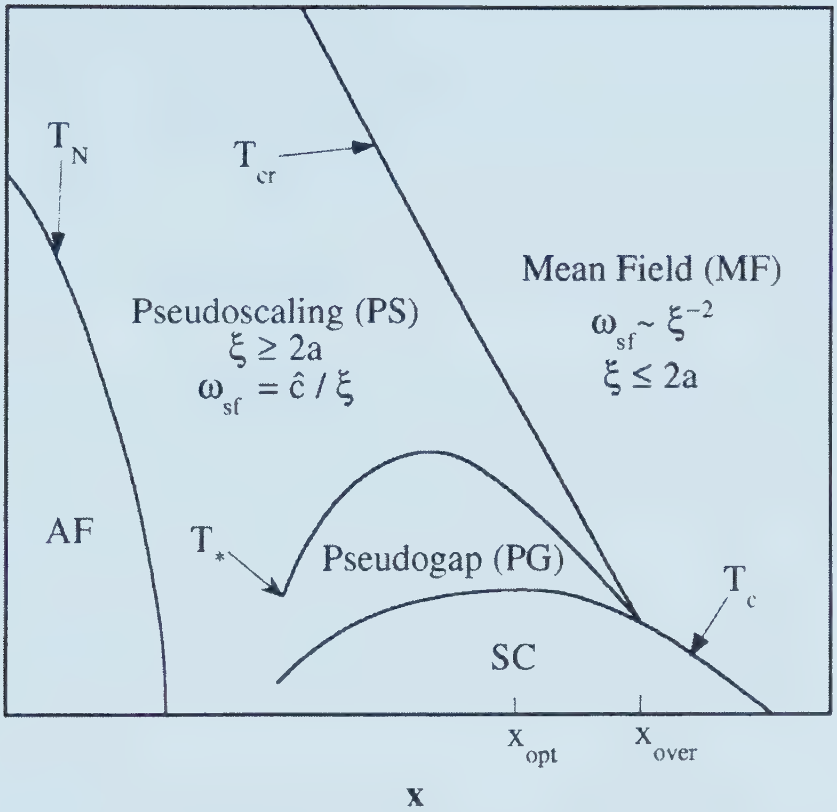

$T_N$
$T_{cr}$
Mean Field (MF)
$\omega_{sf} \sim \xi^{-2}$
$\xi \leq 2a$
Pseudoscaling (PS)
$\xi \geq 2a$
$\omega_{sf} = \hat{c} / \xi$
AF
$T_*$
Pseudogap (PG)
$T_c$
SC
$x_{opt}$
$x_{over}$
x

Fig. 3.5 Phase diagram from the 2D nearly antiferromagnetic Fermi liquids (NAFL) theory: the normal state is divided into three phases.[From Ref. 142. Copyright 1997 by *Springer-Verlag*]

develops into the superconducting gap. On the underdoped side, $T^*$ may be saturated instead of extrapolating to lower doping region (Fig. 3.5).

- Preformed pairing in the normal state. This was proposed based on spectroscopic results [127] that the pseudogap seems to evolve into superconducting gap at $T_c$. In underdoped cuprates, Cooper pairs lose their phase coherence above $T_c$, but may remain bound together, due to large binding energy, well into the normal state ($\sim T_c + 100$ K), as revealed by a recent high-frequency conductivity study [144].
- Spin-charge separation. This scenario assumes that the pseudogap is associated with the pairing of spinons, which are hypothetical charge-neutral

fermions with the electron's spin, whereas the charge is carried by a spinless boson called a holon)

- Magnetic or charge-excitation related origin.
- Existence of pseudogap in the overdoped regime.

## 3.2 Scenarios for the normal state

One of the immense challenges for any high-temperature superconductivity theory is to cover such a broad range of the phase diagram. Many models have been constructed to deal with the normal state behavior, which can be roughly classified into Fermi- and non-Fermi-liquid scenarios. They either assume preformed pairing leading to the superconducting gap (of the same *d*-wave symmetry) or treat the pseudogap separately from the SC gap. Below are some representative theories of the normal state.

1. **Spin-fluctuations**.

This is based on the AF fluctuation scattering. A typical scenario was proposed by Pines *et al.* [142, 145, 146], i.e. nearly antiferromagnetic Fermi liquids (NAFL). NAFL stresses the strong magnetic interaction between planar quasiparticles, which gives rise to the anomalous normal-state behavior and the superconducting transition. Except for the overdoped regime, the normal state is characterized by three magnetic phases [refer to Fig. 3.5]: mean field behavior above $T_{cr}$, pseudogap phase (frozen AF correlations) below $T^*$, and a pseudoscaling region in between ($T_{cr} < T < T^*$) where AF sets in. $T_{cr}$ is linked to the AF correlation length as $\xi(T_{cr}) \approx 2a$, where $a$ is the lattice constant. The linearly increasing $T_{cr}$ with reduced doping is attributed to the increasing AF correlation strength.

One distinct aspect of this scenario is non-pairing in the normal state. The gap is due to a spin-density wave precursor [142]. Along this line, two classes of quasiparticles (i.e. hot and cold) and hence two kinds of energy gaps were proposed for the normal state: $\Delta_{hot}$ and $\Delta_{cold}$. The former is thought to be related to $T^*$, and the latter is proportional to $T_c$, as a result of superconducting pairing of "cold" quasiparticles. Experimental testing of such predication would be interesting.

2. **Stripe phase**

Emery *et al.*[147] and Zaanen *et al.*[148] proposed a different scenario consisting of fluctuating phase-separation and dynamic charge ordering. The picture is as described previously, namely, stripes of AF orderings separated by charge-segregating domain-walls within the $CuO_2$ plane. Non-coherent pairing in the normal state produces the pseudogap. Coherence is established as the temperature approaches $T_c$. Such a scheme complies with the optical and ARPES observations that the transition into the superconducting state is smooth without experiencing dramatic changes. A similar version was constructed by Bianconi [65] with different "ingredients" in the stripes. It is believed that the stripe formation is charge-driven [149]: charge orders at a higher temperature than spin and both are second order transitions.

3. **Spin-charge separation**

This theory originated from the resonating valence bond (RVB) theory [150], and further developed by others [151-153]. In one-dimensional systems, the separation of low-energy spin and charge excitations, due to different propagation speeds, leads to the "splitting" of the electron into a spinon and a holon. The spinon carries the electron's spin and the charge is left for the holon. This idea was applied to the 2D cuprates: pseudogap formation is attributed to the pairing of spinons, while holons (bosons) undergo Bose condensation at the superconducting transition. The linear-$T$ resistivity was explained in terms of holon-spinon scattering. Experimental observation of spinons and holons in cuprates seems scarce. Yasuoka [136] interpreted NMR data in this model. Recently, ARPES evidence of spin-charge separation was reported in 1D $SrCuO_2$ [154].

4. **Bipolaronic conduction**

Bipolarons were initially found in transition metal oxides such as $V_2O_5$, $WO_{3-x}$, and $Ti_4O_7$ [155]. The discovery of high-$T_c$ superconductors renewed the interest in polarons. Alexandrov *et al.* [156-162] investigated the normal-state dynamics using the theory of polarons. The small polarons are paired above $T_c$ to give rise to the pseudogap and other unusual transport behavior, and the superconducting state is a charged ($2e$) Bose-

Einstein condensate of bipolarons. Experimental results in favor of this picture were reported from optical reflectivity [163] and susceptibility measurements [164]. In particular, among the few scenarios which explicitly give the *quantitative* formalism for the normal-state transport properties, Alexandrov *et al.* provided a series of calculations for resistivity, Hall coefficient and angle, and other parameters [156]:

$$\rho = \rho_0 \frac{T + \sigma_b T^2}{1 + bT}, \tag{3.3}$$

$$R_H = \frac{v_0}{2e(n - n_L)(1 + bT)}, \tag{3.4}$$

$$\cot \Theta = \frac{cm^2 C}{2eH}(T + \sigma_b T^2), \tag{3.5}$$

where $n_L$ is the density of localized bosons (bipolarons), $v_0$ the volume of unit cell, and $\sigma_b$ the relative boson-boson scattering cross section; $\rho_0 = m^2 C v_0 / 4e^2(n-n_L)$ and $C$ are fitting parameters. In terms of Bose-Einstein condensation of charged bosons, the superconducting transition temperature was estimated [156]:

$$T_c = \frac{2w(n - n_L)}{L} \qquad \text{for } n - n_L >> 2t_\perp / w, \tag{3.6a}$$

and

$$T_c \approx 4t_\perp \qquad \text{for } n - n_L < 2t_\perp / w; \tag{3.6b}$$

where $L$ is the logarithm of the anisotropic mass ratio; $2t_\perp \approx 45$ K and $w \approx 450$ K are interlayer bipolaron hopping integral and in-plane bipolaronic half-bandwidth, respectively. This gives an estimation of $T_c \sim 90$ K for YBCO.

It is noticeable that the normal-state resistivity of all overdoped cuprates seem to be better fitted to a quadratic relation, $\rho = \rho_0 + aT + bT^2$, than to a simple power-law dependence, $\rho = \rho_0 + aT^\alpha$, with variable $\alpha = 1$ to 2. This is believed to be evidence that linear-$T$ contribution persists into the overdoped regime [165]. However, from the predictions of the bipolaron model, such a temperature dependence is consistently accounted for. Moreover, it was emphasized that a $T^2$ relation, $\rho = \rho_0 + bT^2$, might be preserved even in non-Fermi- liquid-like scattering cases [166]. It should also be pointed out that there exists debate on bipolaron condensation and other issues [167], and the polaronic mechanism of superconductivity does not seem to be widely

appreciated. Nevertheless, we found the fitting of our resistivity data to this model was impressive.

5. **Interlayer tunneling**

The model mainly deals with the superconducting state, and is closely related to the spinon-holon scenario. It is based on the electromagnetic coupling along the *c*-axis [93, 168-170]. The electron transport in this direction is incoherent, as deduced from the semiconducting resistivity. This blocking mechanism in the non-Fermi-liquid normal state provides the superconducting condensation energy. Once pairing happens in the superconducting transition, the *c*-axis transport becomes coherent, which results in Josephson-like or Lawrence-Doniach-like superconducting coupling between the layers (a 2D to 3D crossover). In particular, under the assumption that the Josephson coupling energy is equal to the condensation energy, the theory predicts for the *c*-axis penetration and plasma frequency:

$$\lambda_c = \frac{\hbar c}{2ed}\frac{1}{\sqrt{4\pi E_b^o}}, \tag{3.7}$$

$$\hbar\omega_p^c = \frac{\hbar c}{\sqrt{\varepsilon_0}\,\lambda} = 2ed\sqrt{\frac{4\pi E_b^0}{\varepsilon_0}},$$

where $d$ is the interlayer spacing, and $E_b^o$ is the pairing energy (e.g. $3.5 \times 10^{-6}$ erg/cm$^3$ for YBCO). Good agreement with this scenario had been found for La-214 and Hg-1201. However, direct measurement of vortex dimensions in Tl-2201 [171] differs from the prediction. Metallic resistivity data along the *c*-axis of $YBa_2Cu_4O_8$ [172] and $RBa_2Cu_3O_{6+x}$ [173] also showed that the nonmetallic behavior of $\rho_c(T)$ is not universal in underdoped cuprates. This may change the picture of electron transport in cuprates.

## 4.3 Concluding remarks

The peculiar normal-state properties reflect the exotic charge and spin dynamics associated with the electronic and magnetic correlations intrinsic to the $CuO_2$ planes. After more than a decade's theoretical and experimental exploration, many facts have

been established and issues been clarified. Still, contrasting differences exist among various scenarios in terms of the driven force(s) of electron pairing and superconducting transition. Quantitative calculations for directly verifiable parameters, such as charge transport, are limited. Experimental results reveal both electronic and magnetic origins, presumably because of the different aspects probed by different techniques. Significant concepts around the normal-state anomalies include: formalisms based on Fermi and non-Fermi liquids; preformed pairing without coherence above $T_c$ and its relation with the pseudogap; doping dependence of pseudogap; and the connection between the pseudogap and superconducting gap. Moreover, as suggested by Randeria [174], study of the magnetic field effects in the pseudogap regime and magneto-transport is important. Surprisingly, a recent $^{63}$Cu NMR study did *not* reveal any field effect on the spin gap up to 14.8 T [175], hinting at unrelated nature of superconducting gap and the pseudogap. Finally, if pairing really exists in the normal state, direct experimental probes would be excellent. Further works on these "big rocks" will clear the road to an understanding of high-$T_c$ superconductivity.

Chapter 4

# Unusual Features in the Normal-State Resistivity of Bi-2223 Whiskers†

## 4.1 Introduction

The normal state of high temperature superconductors has been under intensive study for its peculiar properties. From resistivity measurements, some unusual features of the normal state can be revealed: linear-$T$ in-plane resistivity over a wide range of temperature; and a signature of spin gap opening at $T^* >> T_c$ which manifests itself as a downturn in the resistivity from the linear-$T$ relation in underdoped cuprates. These properties are believed to be linked with the superconducting transition. Recently, more and more evidence have been accumulated for spin and charge orderings in a striped phase, in which holes segregate in domain walls separating antiferromagnetic antiphase domains in the $CuO_2$ plane [176-178]. Although experimental work was mainly done on the $La_{2-x}Sr_xCuO_4$ family and related nickelates [see Ref. 178 and references therein], neutron scattering studies on YBCO [129] and ARPES of Bi-2212 [63] also provided evidence for dynamic stripes. The scenario of stripe phase formation in cuprates is supported by theoretical studies [54-58], with such predictions as separated charge and spin ordering at different temperatures.

Obviously, charge ordering and stripe correlation should significantly affect transport properties of the material. Indeed, in Nd doped $La_{2-x}Sr_xCuO_4$ samples, Nakamura and Uchida [177] found resistance jumps both in $\rho_{ab}$ and $\rho_c$ at $T > T_c$, which were interpreted as due to structural phase transition together with stripe correlations. In a recent work on Zn-doped $Bi_2Sr_2Ca_{1-x}Y_x(Cu_{1-y}Zn_y)_2O_{8+\delta}$ [Ref. 179], possible static ordering of holes and spins was proposed in samples with a hole density of $p\sim1/8$.

---

† A version of this chapter had been published: Weimin Chen, J. P. Franck, and J. Jung, *Phys. Rev. B* **60**, 3527 (1999).

Stripe formation must be sensitive to crystalline structure and doping levels, because transport anomalies have not always been found in other cuprates. Such a situation is hard to understand if stripe formation is assumed to be a universal feature of high-$T_c$ cuprates. It is therefore interesting that we have observed novel features in the normal state resistivity of Bi-2223 single crystals.

In this chapter, we report unusual behavior in the normal state resistivity of four Bi-2223 samples ($T_c$ ~110 K). At $T^*$ ~ 250 K, the resistivity starts to deviate from the linear-$T$ relation: while $\rho$ keeps decreasing with temperature, this deviation is upward, rather than the well-known downturn drop in underdoped samples as also found in our Bi-2212 crystals. After a transition region of about 50 K, $\rho$ resumes a nearly linear-$T$ descent again, until $T_c$ is approached. Such a behavior is essentially new for most high-$T_c$ superconductors. We noticed that an up-turn resistivity anomaly was only found in Nd doped $La_{2-x}Sr_xCuO_4$ before [177]. Especially in this and our materials, the resistivity deviations show some similarity in temperature dependence. The fact that resistivity shifts could occur at very similar temperatures (~250 K) may hint at some universal properties related to the specific structures of cuprates. In the light of the transport measurements [177] and recent neutron-scattering results [178], we believe the observed anomalies can be understood in the scenario of structural transformation and charge orderings in the stripe phase.

## 4.2 Experiment

The single crystalline whiskers of Bi-2223 studied here were grown by a sintering method as described in Chapter 2. The typical sample size is 1-6 mm × 10 × 1 μm (thickness). Exact geometrical dimensions were determined by SEM imaging. Resistance was measured by the standard four-wire method. Silver leads were sputter-deposited onto the whisker through a mask. To reduce contact resistance (~ 10 KΩ), the contacts were annealed in flowing nitrogen gas (450°C, 4hrs) after sputtering. This treatment usually results in a low contact resistance of less than 1 Ω for a contact area of 10 × 100 $\mu m^2$. A DC current of 0.5 μA was driven along the length ($a$ axis) of a whisker. Voltage was measured by a nanovoltmeter (Keithley 181). Four samples from

the Al doped plates were measured (hereafter labeled A to D), together with measurements following $N_2$ and $O_2$ annealing. All these samples were randomly picked up from the base pellet, yet their $\rho$-$T$ data showed excellent consistency with each other. To study the influence of doping, the samples experienced different thermal treatments: samples A and B were as-grown in air; C and D were annealed in flowing $N_2$ gas at 450°C for 4 hours.

After the first measurement, samples A and D were annealed in flowing $O_2$ under the same conditions and re-measured with new Ag leads; Sample B consecutively experienced $N_2$ and then $O_2$ annealing, all under the same conditions. Detailed data of $T_c$ and linear-$T$ resistivity fitting for the samples are as shown in Table 4.1. The anomalous features reported here were reproducible after thermal annealing with the Ag leads completely removed (by ammonia +$H_2O_2$), and re-sputtered afterwards.

## 4.3 Results and discussion

Figure 4.1 is a plot of $\rho$-$T$ data of an as-grown whisker (sample A). The other as-grown sample (B) also shows similar result. The mid-point $T_c$ is 110.2 K, as is the case for Bi-2223 crystals. The as-grown whiskers were slightly underdoped [68], as confirmed in later thermal annealing. The transition is narrow (~1.5 K) and sharp, there is no step below $T_c$ which usually shows up in samples mixed with other phases of lower transition temperatures, although resistance data are inadequate to rule out the existence of such phases. $\rho$-$T$ at high temperature (~300 K) follows the usual linearity (the solid line in Fig. 4.1 fitted between 270 to 310 K). While $\rho$ keeps decreasing over the whole temperature range above $T_c$, of significance is the feature below $T^*$~250 K, where $\rho$ deviates *upward* from the linear relation as $T$ decreases, rather than follows the well-known downturn drop found in underdoped single- and double-layer cuprates. As $T$ drops to $T'$~ 203 K, $\rho$ ceases curving up and $\rho$–$T$ resumes a nearly linear-$T$ descent again. This change in the slope of $\rho$–$T$ is more evident in the plot of "excess resistivity" $\Delta\rho \equiv \rho - (a + bT)$ vs $T$ (black-dotted curve, Fig. 4.1), where $\Delta\rho$ is the difference between $\rho(T)$ and the linear line fitted at high temperature and extrapolated to

Table 4.1 $T_c$ and resistivity (fitted from 270 to 310 K) of four single crystalline Bi-2223 whiskers measured in the present work.

| | | $\rho = a + bT$ (μΩ cm) | | |
|---|---|---|---|---|
| Sample | $T_c$ (K) | $a$ (μΩ cm) | $b$ (μΩ cm $K^{-1}$) | $\rho$ (300K) |
| A (as-grown) | 110.2 | -32.88 | 1.23 | 336.1 |
| B (as-grown) | 110.3 | -27.94 | 1.18 | 326.1 |
| C ($N_2$ annealed) | 109.0 | 6.12 | 5.5 | 1656.1 |
| D ($N_2$ annealed) | 109.8 | 15.78 | 1.58 | 489.8 |
| D ($O_2$ annealed) | 111.1 | -19.11 | 1.57 | 457.7 |
| B ($N_2$, $O_2$ annealed) | 110.9 | -34.33 | 1.64 | 452 |

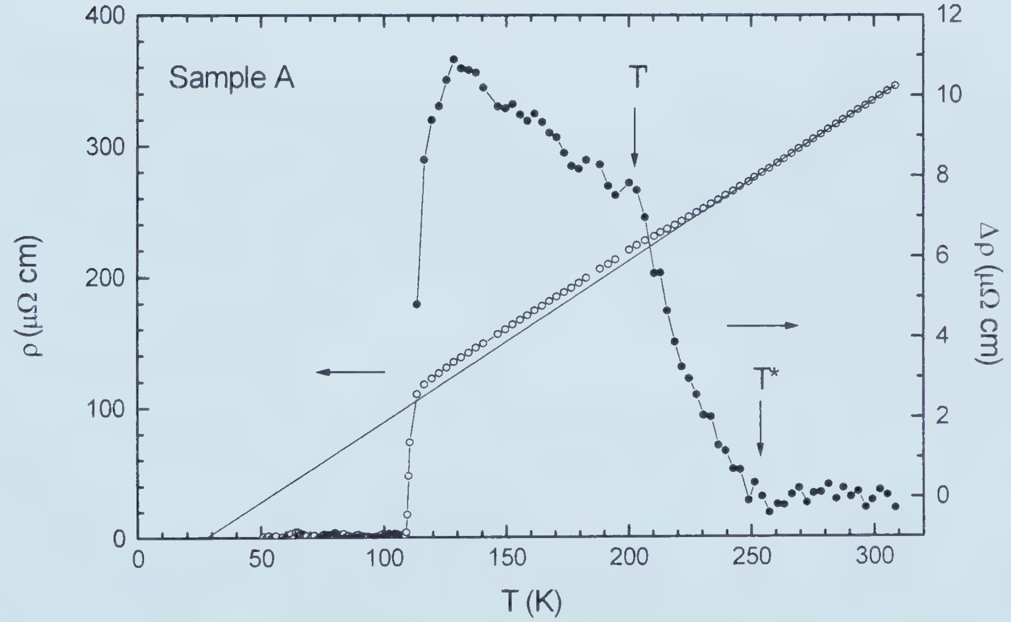

Fig. 4.1 $\rho$-$T$ of an as-grown Bi-2223 whisker. The black-dot curve is the deviation, $\Delta\rho \equiv \rho(T)-(a + bT)$, from the solid line which is linearly fitted between 270-310 K and extended to low $T$. Note the upward shift in $\rho(T)$ and the features below $T^*$ and $T'$, as well as the negative intercept $\rho(0)$. The whisker's dimensions: width: 10.0 μm, thickness: 0.77 μm, and length between voltage leads: 260 μm.

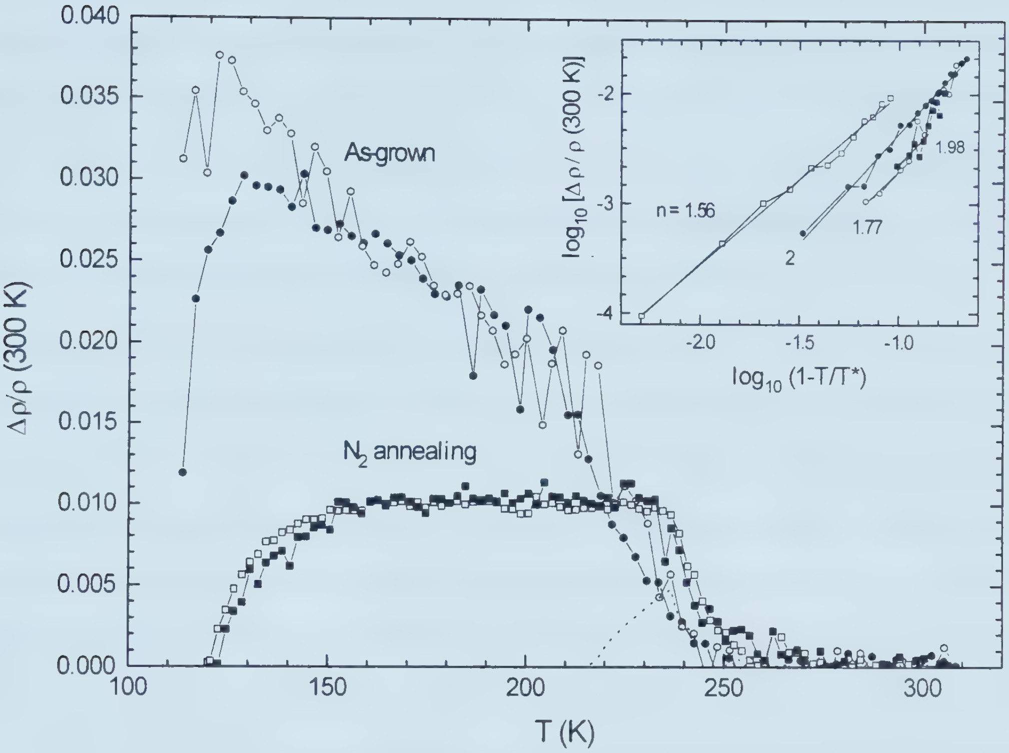

Fig. 4.2 Plots of resistivity deviation $\Delta\rho$ vs. $T$ normalized by $\rho(300)$. Samples A (●) and B (○) are as-grown (in air), whereas C (□) and D (■) were annealed in flowing $N_2$ at 450°C for 4 hours. Also shown for comparison are the data of a typical underdoped Bi-2212 sample (dashed line), which also exhibits a kink below $T^*$. Inset: Fitting of $\Delta\rho \sim (1-T/T^*)^n$ for the region $T<T< T^*$, with $n$ shown by the numbers. Linear fit ranges are as defined by the line segments themselves.

$T = 0$. The "transition region" between the two adjacent segments of $\rho$–$T$ is wide (~50 K), as indicated by the arrows in Fig. 4.1, which excludes the possibility that such a feature could originate from contact leads. In the latter case, $\rho$-$T$ may show irregular change. The anomaly is independent of possible material mixture either, as explained below.

In Fig. 4.2 we plotted $\Delta\rho$-$T$ for four samples: A & B (as-grown in air) and C & D ($N_2$ annealed). The deviation $\Delta\rho$ is as defined in Fig. 4.1 and scaled by the resistivity at 300 K. In all the samples, the anomalous deviation from linear-$T$ dependence around $T^*$~250 K was observed. As $T$ drops below another clearly identifiable temperature

$T$~203 K, $\Delta\rho$ changes to nearly linear-$T$ *increase* until $T_c$ is approached in as-grown samples (A & B). On the other hand, in $N_2$ annealed samples (C & D), $\Delta\rho$ is saturated at $T$ and remains temperature independent over a wide range of temperature above $T_c$. This $T$-independence seems to be a general feature of $N_2$-annealed samples. $\Delta\rho/\rho(300)$ is about 1% and remains the same for both samples even though they have slightly different $T_c$ (hence hole concentration), as shown in Table 4.1.

After we observed the anomalies in Bi-2223 samples, we re-examined our previous $\rho$-$T$ data from underdoped Bi-2212 whiskers, and surprisingly found a similar increase in $\Delta\rho$ around $T^*$~ 250 K. It reaches a maximum just before $\rho$ follows the well-known downward deviation from the linear $\rho$-$T$ line, as shown by the dashed curve in Fig. 4.2. Thus the feature just below $T^*$ seems to be intrinsic to both Bi-2212 and 2223 in the underdoped regime. Details of Bi-2212 results are discussed in Chapter 5. This upward deviation in resistivity mimics the results observed on $La_{2-x-y}Nd_ySr_xCuO_4$ samples ($y$ ~ 0.4, $x = 0.12$-0.2) [Ref.177]. In the latter, $\rho_c$ of a $x = 0.2$ sample showed a kink near 250 K. The kink was attributed to the high-temperature tetragonal (HTT) to the low-temperature orthorhombic (LTO) phase transition. Additional jumps in $\rho_{ab}$ and $\rho_c$ were also observed at a lower temperature (~77 K) due to LTO to LTT transition. It is therefore interesting to compare the very similar values of the high transition temperature (~250 K). Since the structure of Bi-2223 is pseudotetragonal, we are led to interpret the resistivity anomaly in this material as being due to similar structural phase transition. The common temperature may hint at a universal characteristic of such HTT to LTO transition in cuprates. This point of view about structure transformation is further supported by elastic property studies on similar Bi-2212 whiskers provided by Jung and Franck [180]. In the temperature range 270 K < $T$ < 300 K, anomalous peaking of Young's modulus and appearance of hysteresis in stress-strain curves indicated the presence of a phase transition. A further noticeable point in our measurement is the fluctuating signal below $T^*$ compared with the more stable situation above. $\Delta\rho$-$T$ in the transition region ($T < T < T^*$) can be well fitted to an empirical power law:

$$\Delta\rho \propto (1-T/T^*)^n, \tag{4.1}$$

with $n = 1.5$ to 2 as plotted in the inset of Fig. 4.2.

We noticed that a similar resistance kink around $T^*$ in YBCO already exists in the literature. For example, in the systematic investigation on the normal state of underdoped $YBa_2Cu_3O_x$ [Ref.105], a resistivity shift in the $x = 6.85$ sample near $T^*\sim265$ K is clearly visible in the $\rho$-$T$ plot and more so in the $d\rho/dT$ vs $T$ curve. Therefore, we were led to the speculation that the upward curving in resistivity below $T^*$ is universally observable in high-$T_c$ cuprates, and is connected to a structural transformation or lattice distortion. The idea of a structural phase transition followed by charge ordering was confirmed in neutron scattering experiment on La compounds [178].

Now we discuss the feature at lower temperature. The clear turning of the $\Delta\rho$-$T$ curve at $T$ signals a new mechanism. Again in $La_{2-x-y}Nd_ySr_xCuO_4$, the resistivity increase below the transition temperature ($T_0$) was explained to be a possible indication of the formation of a stripe phase: charge segregation within domain walls that separate antiferromagnetic antiphase domains in the CuO planes [178]. Our $\rho$-$T$ data bears close resemblance to this scenario. $\Delta\rho$-$T$ curves of as-grown samples in Fig. 4.2 are very similar to Fig. 12 of Ref.178, which was interpreted as a signature of charge ordering. The neutron scattering data of $La_{2-x-y}Nd_ySr_xCuO_4$ showed approximately linear-$T$ increase for charge ordering intensity below $T_0$ [178]. Thus, our present results fit in this picture. Especially in $N_2$ annealed samples, $\Delta\rho$ saturated right after the first common region. This implies that a reduction in hole concentration may prevent charge segregation from happening due to insufficient holes. As a result, the increase in $\Delta\rho$ with decreasing $T$, caused by continuous charge localization, will not show up. The total resistivity is inherent to the new crystal structure formed around $T$, i.e. a new linear-$T$ behavior. This argument is supported by $O_2$ annealing of one sample previously treated in $N_2$ (sample D). As shown in Fig. 4.3, after $O_2$ annealing, the behavior of this sample below $T$ was completely altered. $\Delta\rho$ no longer saturates as it does in Fig. 4.2, rather, it shows similar $T$ dependence as those grown in air. This clearly demonstrates that the increase in $\Delta\rho$ at low temperature is solely caused by increased hole concentration compared with $N_2$ annealed samples. As reference, sample B (as-grown) was also annealed successively in $N_2$ and $O_2$ under the same conditions. Its $\Delta\rho$-$T$ agrees well

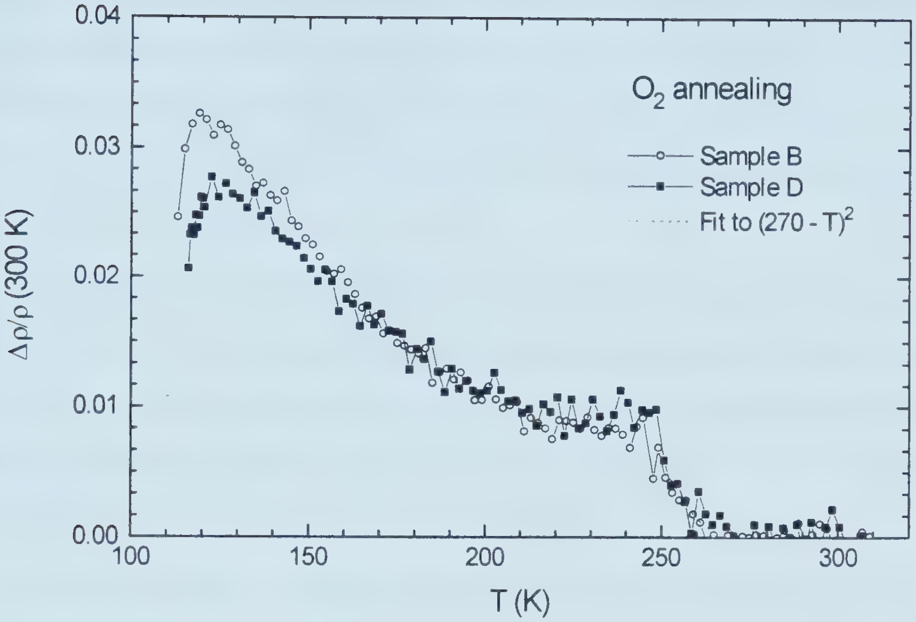

Fig. 4.3 Effect of $O_2$ annealing on the "excess resistivity" $\Delta\rho$ scaled by $\rho(300)$. The $T$-independence of $\Delta\rho$ for sample D as a result of $N_2$ annealing is completely altered to agree with the other sample when they were annealed in $O_2$. $\Delta\rho$ behaves in the same way as that of as-grown samples below ~215 K, refer to Fig. 4.2. Between 215 - 250 K, there is a $T$-independent plateau.

with sample D (Fig. 4.3).

Further proof of hole density dependence of such distinct $\Delta\rho$-$T$ behaviors comes from the influence of thermal treatment on the residual resistivity. We found that both as-grown and $O_2$-annealed samples had negative axis intercepts ($T = 0$) for the linear $\rho$-$T$ relation fitted to the high-$T$ portion (between 270 to 309 K); On the contrary, the similar $\rho$-$T$ fittings of $N_2$-annealed samples consistently yield small positive $\rho(T = 0)$, as detailed in Table 4.1. The residual resistivity (both its magnitude and sign) is believed to be related to carrier density in the normal state [181]. The present annealing result clearly demonstrates this idea and supports the interrelation between carrier density and distinct $\Delta\rho$-$T$ behaviors below $T'$. Bi-2223 whiskers grown in air are slightly on the underdoped side according to the $T_c$-$p$ (hole concentration) diagram [68], as opposed to the overdoped case of as-grown Bi-2212. Annealing the samples in $N_2$ brought the residual resistivity to a small positive value, $\rho(0)/\rho(300K) = 3\%$ for sample D as shown

in Fig. 4.4. After annealing in flowing $O_2$, the residual resistance was brought back to be negative as expected, as well as the switchover of $\Delta\rho$ from saturation to weakly linear-$T$ dependence below $T'$. This property seems to be significant in near-optimally doped Bi-2223 samples, because we did not find similar sign change in our extensive Bi-2212 results, which further proves that the normal state features reported here can be attributed to the Bi-2223 phase.

The contrasting behaviors of Bi-2212 and Bi-2223 below $T'$ may explain the situation that none of the spin-gap induced signatures have been observed so far in Bi-2223 by the standard techniques (R-T, ARPES, NMR, etc.). Our results indicate that the triple-layer system (at least Bi-2223) may follow a different "route" in its normal state dynamics, compared with its double-layered counterpart.

It is true that there may be a mixture of Bi-2212 and Bi-2223 phases in our samples, as shown in the inset of Fig. 4.4, where another tiny step appears at a lower temperature (~80 K) signaling the Bi-2212 phase. However, we argue that the anomalous features around 250 K are not a result of such phase mixing, since, as was found in other works [182], the normal state resistivity can still be completely linear above $T_c$, even though the samples contained both phases. We also found similar results in a $T_c = 100$ K sample from a pellet intended for growing Bi-2212 whiskers. It is interesting to notice the opposite effect of thermal annealing on the $T_c$'s of the two phases: $O_2$ annealing following $N_2$ annealing increased the $T_c$ of Bi-2223, but lowered that of Bi-2212. This clearly showed that $N_2$ treated Bi-2223 and Bi-2212 phases in the sample were on the opposite sides of the inverted parabola of the unified $T_c$-$p$ (hole concentration) relation [68]:

$$T/T_{c,max} = 1 - 82.6(p - 0.16)^2. \tag{4.2}$$

Since $N_2$-annealing the as-grown samples would only shift the $T_c$ by a small amount (<3 K), $O_2$ annealing under the same conditions (450°C and 5 hours) should not carry the doping level over the optimal point and onto the overdoped side. Thus the as-grown Bi-2223 is slightly underdoped whereas the as-grown Bi-2212 is overdoped, the latter was always the case when we tried to grow Bi-2212 whiskers.

It is not clear why the observed resistivity anomalies were not detected in other

groups' Bi-2223 materials. One answer may come from the significant dependence of the sign of $\rho(0)$ on different thermal annealing conditions. That the sign can be relatively easily switched in our samples by annealing implies that the hole concentration in the samples must be near some critical value which causes the anomalous $\Delta\rho$-$T$ just below $T^*$. This point was supported in the case of underdoped $YBa_2Cu_3O_x$ [Ref.105], in which the anomaly only appeared in a very narrow doping window (less than $\delta x = \pm 0.1$) around the oxygen content $x = 6.85$. As we have seen in the previous discussion, hole density is crucial in determining the subsequent temperature dependence of $\Delta\rho$. The specific whisker growth method in this work may have set the samples around the critical hole density range, i.e. slightly underdoped. Annealing the samples under the present conditions could not carry the samples too far away in terms of hole concentration, which is mainly dependent on annealing

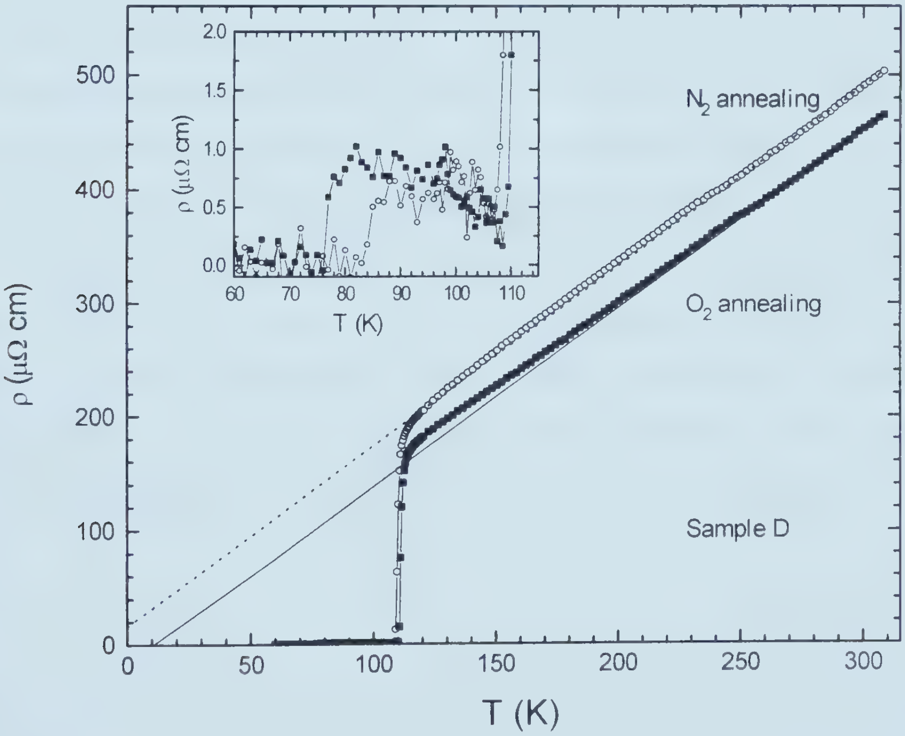

Fig. 4.4 Influence of $N_2$ and $O_2$ annealing on $T_c$ and normal resistivity. The inset is a detailed view of the low temperature tail, showing the mixing of Bi-2212 phase. Note the opposite effect of thermal annealing on the $T_c$'s of Bi-2223 and Bi-2212 phases.

temperature and oxygen partial pressure. This explains why the feature below $T^*$ appears in all the samples. Another factor may come from material quality. Bi-2223 is usually prepared by starting from Bi-2212 phase, which frequently resulted in a mixing of both phases. Comparing the distinct behaviors of our Bi-2212 and Bi-2223 whiskers in terms of $\rho(0)$ and normal state resistivity, we can assert the samples studied here consist mostly of Bi-2223, if not as a pure phase.

## 4.4 Conclusion

In conclusion, we have observed new anomalous features in the normal state resistivity of single crystalline Bi-2223 whiskers, in which $\rho$-$T$ starts to deviate *upward* from the linear-$T$ relation at $T^*$~250 K. This anomaly seems to be universally observable in high-$T_c$ cuprates, and thus might be closely related to the unique structure of this type of material. Even in our resistivity measurement of underdoped Bi-2212 samples which exhibit the well-known down-turning $\rho$-$T$ below $T^*$ (~200 to 250 K), a slightly upward curving in resistivity over a temperature interval of about 30 K appears just before $\rho$-$T$ deviates downward from the linear relation. This is consistent with the picture of a structure transform or lattice distortion followed by charge or spin excitations as established by neutron scattering studies [178]. As the temperature further decreases to about 50 K below $T^*$, the deviation reaches about 1-2% of the room temperature resistivity and distinctly turns to either $T$-independent ($N_2$ annealing cases) or weakly linear-$T$ (as-grown and $O_2$-annealed samples) behavior. This behavior can be understood in the scenario of stripe formation within the $CuO_2$ planes.

## Chapter 5

# Signatures of Exotic Electronic Scattering$^\dagger$

## 5.1 Structural instabilities in the normal state of cuprates

The normal state of high-$T_c$ cuprates provides rich information for an understanding of superconducting mechanism. Two of the many interesting normal-state properties are the pseudogap opening and crystal structural transformation. In resistivity ($\rho$) measurement, the former was believed to manifest itself as a downturn deviation from the linear $\rho$-$T$ relation below some characteristic temperature $T^* > T_c$ in underdoped samples. Evidence due to crystal structure transformation (or lattice distortion) is more difficult to detect because of such factors as crystal quality and the weakness of its physical effects. Structural transformation is generally studied by elastic and acoustic methods [183]. In most of the cuprates, anomalous features corresponding to structural instabilities in the normal state have been observed. In $La_{2-x}Sr_xCuO_4$, a tetragonal to orthorhombic structure transition upon cooling occurred at 220 K [184]. Around the same temperature for $YBa_2Cu_3O_{7-\delta}$, the sound velocity showed a step-like change and was associated with the instability corresponding to a structural order-disorder transition [185]. A step-like change in Young's modulus (hysteresis) also appeared in elastic measurements of single crystals at 200 - 240 K [186, 187]. In Bi cuprates, similar evidence was also accumulated. Dominec *et al.* [188] reported sound velocity deviations around 240 K in $Bi_2Sr_2CuO_6$ (Bi-2201). Acoustic studies revealed sound velocity softening along the *a*-axis around 250 K in $Bi_2Sr_2CaCu_2O_8$ (Bi-2212) samples [189, 190]. In elastic property measurements of similar Bi-2212 whiskers as discussed below, Tritt *et al.* [180] found anomalous peaking of Young's modulus and stress-strain hysteresis near 270 K, and interpreted it as evidence for a phase transition. Similar results were also obtained from $Bi_2Sr_2Ca_2Cu_3O_{10}$ (Bi-2223) [191]. More directly, by using acoustic and x-ray diffraction methods, Titova *et al.* [192] consistently found a small

---

[†] Weimin Chen, J. P. Franck, and J. Jung, http://xxx.lanl.gov/cond-mat/9906079; Submitted to *Phys. Rev. B.*

increase of lattice dimensions at $T \sim 190 - 270$ K for the cuprates: YBCO (1213 and 124), Bi-2201, 2212, and 2223, and Tl-series compounds.

The structural instabilities of the cuprates observed at comparable temperature ranges (about 200 to 300 K) demonstrate common features consistent with their similar crystalline structures. Obviously, structural transformation affects transport properties of the material and should be detectable by resistivity measurement. Indeed, resistivity jumps were observed above $T_c$ in $La_{2-x}Sr_xCuO_4$, which are caused by structural phase transition [177]. However, few results were reported for other cuprates in the temperature regions where lattice instabilities were found by mechanical methods described above. This situation can be understood in two ways. First, the influence of structural instabilities on sample resistivity is small, because at such structural transformation, the crystal symmetry usually remains the same and only the lattice parameters change (distortion), leaving weak traces on electron scattering. Secondly, the small change in resistivity can be easily covered up by effects such as percolation, and is undetectable unless the crystal is of very high quality. Therefore, in the present work on pure single crystalline Bi-2212, it is interesting that we observed unusual features in the normal-state resistivity in temperature regions where x-ray and mechanical studies had revealed anomalous structural properties. This is a clear indication of correlation between these features probed by different methods. Moreover, drastically different temperature dependence of resistivity appeared below these anomalies, showing crucial connections between the phenomena in these temperature regimes.

In our extensive resistivity measurement of both Bi-2212 and Bi-2223 whiskers, we often noticed the data were fluctuating in a temperature region between 180 and 270 K. Outside this window, the signal is much more stable. Since this temperature range corresponds to the important regime where resistivity shows dramatic changes and is central in the normal-state theory, we were motivated to check the resistivity in this region more closely. In this work we report five samples selected from many others which exhibit anomalous behavior in this temperature window.

## 5.2 Evidence of exotic electronic scattering

Samples of Bi-2212 whiskers were grown by a sintering method [75], as is detailed in Chapter 2. The single crystals have typical dimensions: 3 mm × 10 μm × 0.5 μm along the *a*, *b*, and *c* axes, respectively. Before making the first measurements, some samples were annealed in flowing nitrogen at 450°C for 4 h, making them slightly underdoped. The resistivity was measured by the standard four-wire method. The electrical leads were made by magnetron sputtering of silver through a mask. A DC current (0.5 μA) was driven along the *a*-axis and voltage was also measured in this direction.

Figure 5.1 shows the resistance ($R$) data of one whisker (sample A, as-grown), together with a segment of $R$ above 200 K. At high temperature, $R$-$T$ is well fitted to a linear line (fitting range: 260 - 308 K) with $R(\Omega) = 129.62 + 2.475T$. As the temperature is further lowered, $R$ shows a clear upward curving just before it follows the well-known downward deviation. To examine the curve in more detail, we plotted the temperature dependence of the resistance deviation $\Delta R \equiv R - (a + bT)$, where $(a + bT)$ is the high temperature fit as

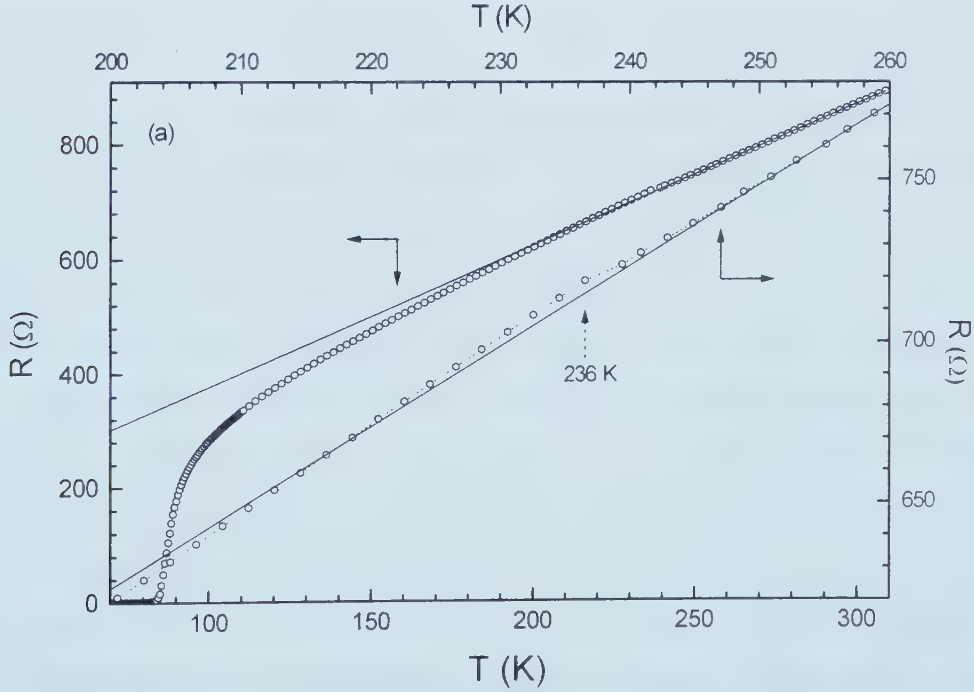

Fig. 5.1 Resistance of one Bi-2212 whisker with $T_c = 86.6$ K (obtained from the maximum $dR/dT$). The lower curve is a detailed view for $T = 200$ to 260 K. The jump in slope is evident near 236 K as indicated by the arrow. The solid line is a linear-$T$ fit at high temperature (250 to 310 K).

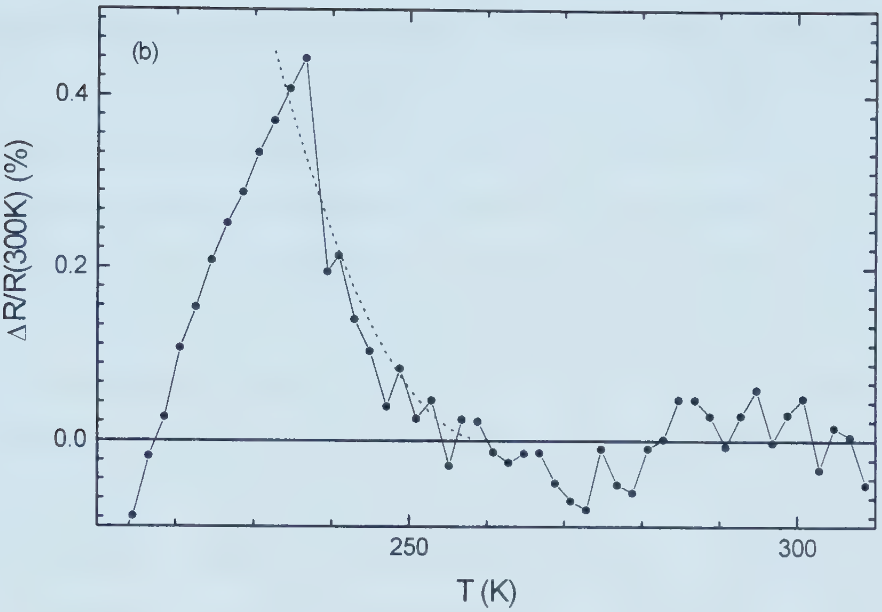

Fig. 5.2 Resistance deviation, $\Delta R \equiv R - (a + bT)$, where $(a + bT)$ is the linear-$T$ fit in Fig. 5.1. The dotted line is a power-law fit: $\propto (260 - T)^2$.

described. The sharp turning point and the slope change is more evident in the plot of $\Delta R$ as shown in Fig. 5.2. We can see that, while $R$ keeps decreasing with $T$, $\Delta R$ starts to deviate *upward* at $T_0 \sim 260$ K and reaches a maximum at $T^* = 236$ K, it then falls and becomes negative, i.e. $R < a + bT$. The peak $\Delta R/R(300\text{ K})$ is about 0.5%. Although the choice of fitting range of temperature may slightly affect the kink, the two major features that $R$ curves upward from linear-$T$ dependence and reaches a sharp turning point are clearly identifiable. Such small bumps could be easily smeared out in samples with defects such as grain boundaries, where percolation is not negligible, to yield a fully linear-$T$ resistance. In our twinned samples, which have a two-step superconducting transition, linear-$T$ dependence was observed without any feature in the normal state. This agrees with the studies by Gorlova and Timofeev [193] who made combined electron diffraction and resistivity measurement on the same sample, and showed that a wider portion of linear-$T$ resistivity appears in twinned whiskers or samples covered with a polycrystalline film than in purer samples. This explains the often-observed discrepancy in bulk materials between transport and other measurements in which the sample's polycrystalline nature is not important. The small change in resistivity puts a high requirement on sample quality to

observe these anomalies. The feature was identified only after more significant kinks around this temperature region were found in our Bi-2223 single crystal samples, as studied in the previous chapter [see also Ref. 194]. The kink in $\Delta R$ seems to follow a power-law relation $(1-T/T_0)^2$ (dotted line in Fig. 5.2, where $T_0 = 260$ K). However, it could also fit to a weak exponential increase of the form: $\Delta R = R_0 exp[c(T_0 - T)]$, with $c = 0.1$ to 0.2.

In Fig. 5.3 we plotted $\Delta R/R(300)$ vs. $T$ for four more samples plus sample A from Fig.5.2. The annealing status of these samples are as follows: A and B: as-grown in ambient pressure; C: annealed in flowing $N_2$ (450°C, 8 h); D: flowing $N_2$ annealing (450°C, 4 h); and E: flowing $O_2$ annealing (450°C, 10 h). The doping level may not solely depend upon the annealing conditions because the sample size varies. Nevertheless, data from long-time annealed samples are reliable. Two cases in the temperature dependence of $\Delta R$ can be classified, as shown in the separate panels of Fig. 5.3. In the lower panel, $\Delta R$ reveals one kink as discussed. $\Delta R$ falls steeply right after the sharp peak, which gives rise to the

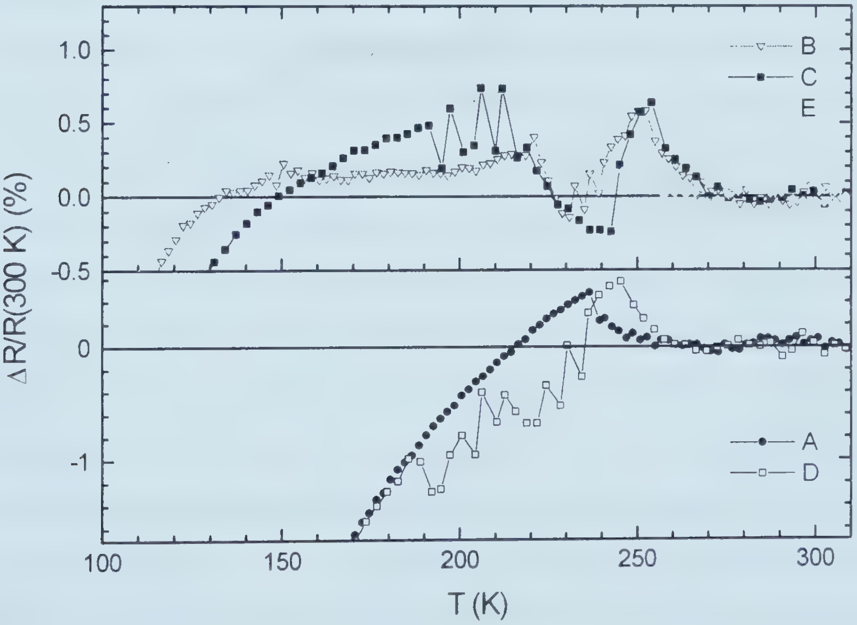

Fig. 5.3 Temperature dependence of $\Delta R$ as defined in Fig. 5.1. The annealing status of samples is as the following: A and B: as-grown; C: $N_2$-annealed (450°C, 8 h); D: $N_2$-annealed (450°C, 4 h); and E: $O_2$-annealed (450°C, 10 h). Note the noisy signal just below the kinks.

well-known downward turning *R-T* in underdoped cuprates. Our identification of this transition temperature is much clearer than the data available in the literature [70], as determined from, for example, 10% deviation. The curves in the top panel show another kink following the first one (samples B and C), which resulted in an S-shaped feature in the *R-T* curve. At the end of this curving, *R* nearly resumes the previous linear-*T* descent. The origin of this anomaly is unclear. It does not show up in the underdoped cases. For the sample annealed in oxygen (E), the kink around 250 K is absent, but the kink at lower temperature (~ 220 K) is consistent with the second kinks in the other two samples. A very similar single kink was also found in the as-grown data of sample C (refer to the inset of Fig. 5.4), which is also oxygen overdoped. These features in the normal state thus seem to be intrinsic to the Bi-2212 samples. This result joins our previous results from Bi-2223 samples to give a consistent picture about the anomaly around this characteristic temperature region in Bi-series cuprates. The peaking temperature $T^*$ shows a trend to increase with the extent of underdoping. $T^* = 254$ K is the highest for sample C which experienced the longest $N_2$ annealing, whereas the oxygen-annealed sample E showed the lowest $T^*$ (220 K). The temperature $T_0$, at which $\Delta R$ starts to climb up, also shows the similar dependence. The detailed characteristic temperatures for the samples are listed in Table 5.1. In light of thermal and elastic measurement results in the literature, which showed evidence of structural phase transformation around the same temperature region as is reported here, we interpret such upward deviation as due to structural transformation or lattice distortion. Similar kinks in resistivity had been observed in La-214 due to structural transformation [177]. The signal is often fluctuating immediately following the kink, in the region around 200 K as shown by the oscillating $\Delta R$. This is obviously correlated to the $\Delta R$ jump, and may well mean an influence on electron scattering due to structural instabilities.

The peak temperature $T^*$ clearly separates two regions in which different mechanisms are switched on. Especially for the noisy region below $T^*$, if it is caused by the opening of a pseudogap in the spin excitation, the initial fluctuating *R* data may be a clue for this mechanism, when the antiferromagnetic correlation is gradually frozen out. In the scenario of stripe phase formation, on the other hand, the stripe phase may be triggered by the lattice distortion. Charge or spin excitation following a structure transformation (or lattice distortion) was established by neutron scattering studies [178]. Bianconi *et al.* [64] have

Table 5.1 Characteristic temperatures of the samples: $T_c$ (from the maximum $dR/dT$), $T^*$ at the $\Delta R$ peaks, and $T_0$ where $\Delta R$ starts to deviate upward. The thermal annealing conditions are shown with the all temperatures set at 450°C.

| Samples | $T_c$ (K) | $T^*$ (K) | $T_0$ (K) |
|---|---|---|---|
| A (as-grown) | 87.5 | 236 | 263 |
| B (as-grown) | 85 | 252 | 275 |
| C ($N_2$/8 h) | 76 | 254 | 278 |
| D ($N_2$/4 h) | 70 | 245 | 262 |
| E ($O_2$/10 h) | 76 | 220 | 246 |

showed for Bi-2212 that 1D modulation of the $CuO_2$ plane is formed by alternating stripes of low temperature orthorhombic and low temperature tetragonal lattices. However, our $T^*$(~ $3T_c$) is higher than their data (~ $1.4T_c$). Whatever the model will be, the present result shows that the lattice structure undergoes some change in all the samples, which initiates new resistive mechanisms. The subsequent dynamics, however, depends on the oxygen doping level, not on this structural change.

The upward deviation is not due to thermal stress in the sample, which is anchored onto the glass substrate by silver leads. We estimate the thermal stress to be a small value ~ 0.018 GPa at 250 K, by taking the Young's modulus $Y = 20$ GPa [180], the thermal expansion coefficient along the *a*-axis $\alpha = 14.4 \times 10^{-6}\ K^{-1}$ [195], and a length between voltage leads of about 0.3 mm at room temperature. Chen *et al.* [196] had measured the effect of uniaxial stress (strain) on the resistivity of similar whiskers, and found that the influence is very small (~ 1/12000 at room temperature). Moreover, the pressure generally causes a decrease in resistivity.

To further study the influence of doping on $T^*$, we annealed one sample (C) successively in flowing nitrogen. The resistance data from this sample are as shown in Fig. 5.4. The result from the as-grown sample shows a slope change near 200 K. $R$-$T$ is linear above this temperature. After one annealing, a new feature appeared around $T^*$ ~ 220 K, while the slope change around 200 K remains. After the second annealing, $T^*$ shifted to 245 K, as indicated by the arrows, showing the tendency that $T^*$ increases with further underdoping, which agrees with the widely observed behavior of resistivity anomaly and the pseudogap.

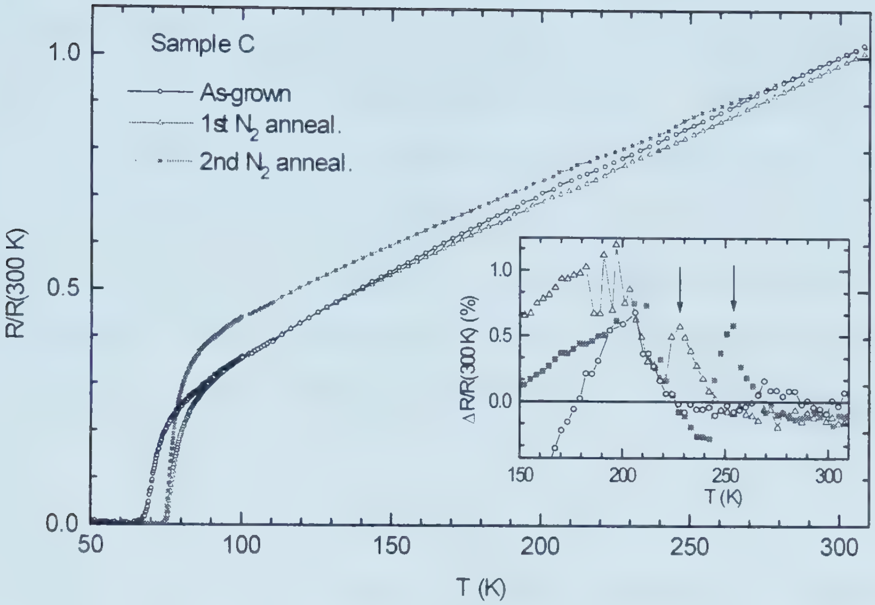

Fig. 5.4 Influence of repeated thermal annealing on the resistance of one sample (C). Inset: $\Delta R/R$(300 K) vs. $T$. For clarity, some fluctuating data points just below the kinks near 200 K were taken off, refer to the raw curve of open triangles. The arrows indicate the new kinks at increasing $T^*$ after successive $N_2$-annealing.

All the above discussion is based upon crystal structure instability in the normal state. In light of the magnetic structure of the $CuO_2$ planes, an alternative interpretation may come from the competition between quasiparticle scattering and the increasing correlation with AF ordering as the temperature is decreasing. It is interesting to compare the present results with the anomalous resistivity of magnetic materials [197-200]. In fact, resistivity kinks were commonly found near magnetic phase transitions in the latter. For example, in dysprosium single crystals [197], a kink in the linearly decreasing $\rho$-$T$ appears near the Néel point when the sample transforms from the paramagnetic into the AF state. Similar anomalies were also reported in europium chalcogenides [198]. It is interesting to notice that the Néel temperature of perovskite $KNiF_3$ is about 253 K [200], very close to the anomalous temperatures in the present work. This may point to a common origin of the resistivity kinks for the materials with similar crystal structures.

In the scenario of free electron scattering with spin excitations, the total resistivity consists of three additive terms: the $T$-independent residual resistivity $\rho_0$ due to elastic impurity scattering, the lattice contribution (phonon) $\rho_L \propto T$, and the spin-disorder resistivity $\rho_M$. The resistivity kink (exponentially increasing with decreasing $T$) is associated with the spin-disorder resistivity ($\rho_M$). In the critical region of magnetic transition, the behavior of $\rho_M$ reflects the strongly temperature dependent short-range spin-spin correlation. This is in the regime of spin-disorder due to the large long-range magnetic fluctuations near the transition temperature [200]. The resistivity thus takes the form:

$$\rho(T) = \rho_0 - b|t-1|\,\ln|t-1|^{-1},$$

where $t = T/T_c$. For $b>0$, $\rho(T)$ shows a concave cusp at the magnetic transition temperature $T_c$. If this idea is valid, then the observed anomaly near $T^*$ ~250 K must come from the antiferromagnetic ordering of the $CuO_2$ planes. Especially, the sharp turning point in all the curves may well signify a similar magnetic phase transition. Currently only the spin fluctuation theory [46, 146] is a close approach to this picture.

In conclusion, an upward deviation from the linear-$T$ dependence was observed around $T^*$ ~250 K in the normal-state resistivity of Bi-2212 single crystals. This is usually followed by a fluctuating region near 200 K. We interpret such behavior as due to structural instabilities in accordance with many results from other measurement techniques (thermodynamic, elastic, acoustic, and x-ray). A peak in the resistance deviation ($\Delta R$) is clearly identifiable. Below this sharp turning point, resistivity drops more steeply, signifying new mechanism in underdoped samples. This turning in resistivity had been widely identified as pseudogap opening. However, the scenario of stripe formation preceded with lattice instabilities was also proposed [178]. The result shows that the lattice instability exists in all the samples regardless of their doping level. The same result was also found in our Bi-2223 samples. This gives a consistent picture intrinsic to similar crystal structures of Bi-cuprates. Although structural transformation seems to trigger new mechanism, it is the oxygen doping which controls the subsequent behavior of $R$-$T$. It is noticeable that our $T^*$ data are consistently higher than the literature values (typically 120 -165 K, with the highest for Bi-2212 being 220 K [70]). There is no

identifiable feature (smooth *dR/dT*) in our *R-T* curves below 180 K. An alternative interpretation of the resistance kinks is the correlation between electrons and AF spin fluctuations. Similar mechanisms in magnetic materials are known to give rise to the kinks in the resistivity curves at magnetic phase transition. Our work should stimulate theoretical interest in this direction.

## 5.3 The scenario of bipolaronic conduction

The origin of normal-state resistivity of high-$T_c$ cuprates is still unclear although various scenarios had provided different interpretations based on Fermi and non-Fermi liquid approaches. This issue is further complicated by the pseudogap phenomenon, which manifests as down-turning deviation in resistivity. Much remains controversial on such fundamental issues as relationship between pseudogap and superconducting gap, whether the former evolves into the latter at the superconducting transition; existence of preformed pairing and its effect on transport; and whether the pseudogap persists into the overdoped region. In the normal-state resistivity measurement, it is noticeable that, very often, the $\rho$-$T$ plot is curving at least below $T_c$ +100 K, and a forced linear-$T$ fitting is tentative and contains randomness in selecting the lower-end temperature.

The bipolaronic model [156], on the other hand, is one of the few theories that give *quantitative* explanations of normal-state properties, including the non-linear-$T$ resistivity. It is thus inspiring to check the normal-state resistivity along this line and test the validity of bipolaronic scenario. We found the data can be fitted to this model over very wide temperature ranges. In some samples, this fitting range extends from $T_c$ + 40 K up to 300 K. This raises the interesting question that the down-turning resistivity, which is labeled as a spin gap signature, is unified into a single curve covering almost the whole normal state! If the fitting correctly reflects the theory, the spin gap (in the sense of resistivity deviation) just disappears in this picture. Moreover, since the fitting extends down to lower temperatures near $T_c$, the superconducting fluctuation range is largely reduced. These results provide alternative interpretations of the peculiar behavior in resistivity.

Figure 5.5 shows a typical resistance data of a Bi-2212 sample. The dotted line is a linear-$T$ fitting at high temperature, and the solid line is a fit to the polaron model [156]:

$$R = R_0 \frac{T + \sigma_b T^2}{1 + bT}, \tag{5.1}$$

where $\sigma_b$ is the relative boson-boson scattering cross section; $b$ is related to Hall coefficient

$$R_H = \frac{v_0}{2e(n - n_L)(1 + bT)}, \tag{5.2}$$

with $(n\text{-}n_L)(1+bT)$ being the number of delocalized carriers in the unit-cell volume $v_0$ ($5.40\times5.41\times30.9$ Å$^3$), and $R_0$ is fitting parameter. To perform the fitting, the value of $b$ or $\sigma_b$ is needed. Since it is difficult to measure Hall effect on the whiskers, we use the Hall coefficient data from Ref. 201: $R_H$ ($10^{-3}$ cm$^3$/C) = 2.5, 2.3, 2.1, and 1.9, for $T$ = 150, 200, 250, and 300 K, respectively. Fitting these data to Eq. (5.2), we have $b$ = 0.003 K$^{-1}$ and $(n - n_L) = 0.076$. This results in $\sigma_b \approx 0.0011$ to 0.0016 from experimental fittings.

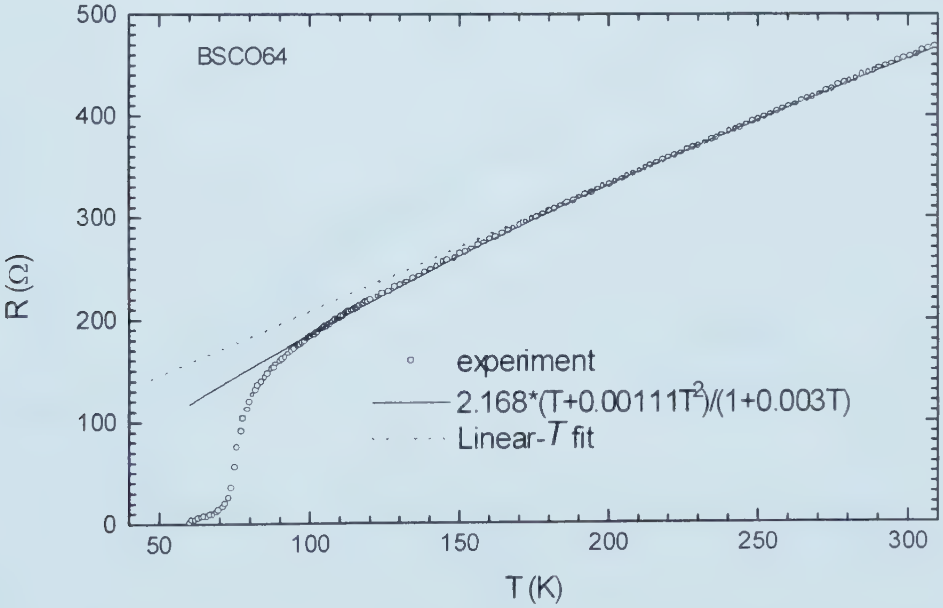

Fig. 5.5 Linear-$T$ (dotted line) and bipolaronic (solid line) fittings to the normal-state resistivity of a Bi-2212 sample.

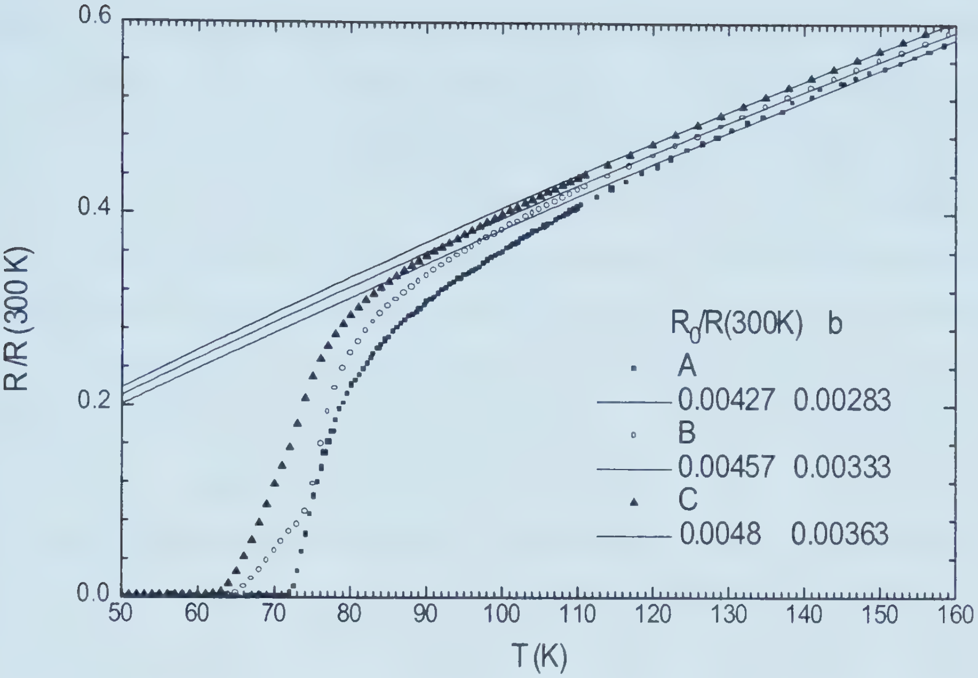

Fig. 5.6 Fitting of resistance data to polaron model for three Bi-2212 samples. The numbers are fitting parameters of $R_0/R(300\text{ K})$ and $b$.

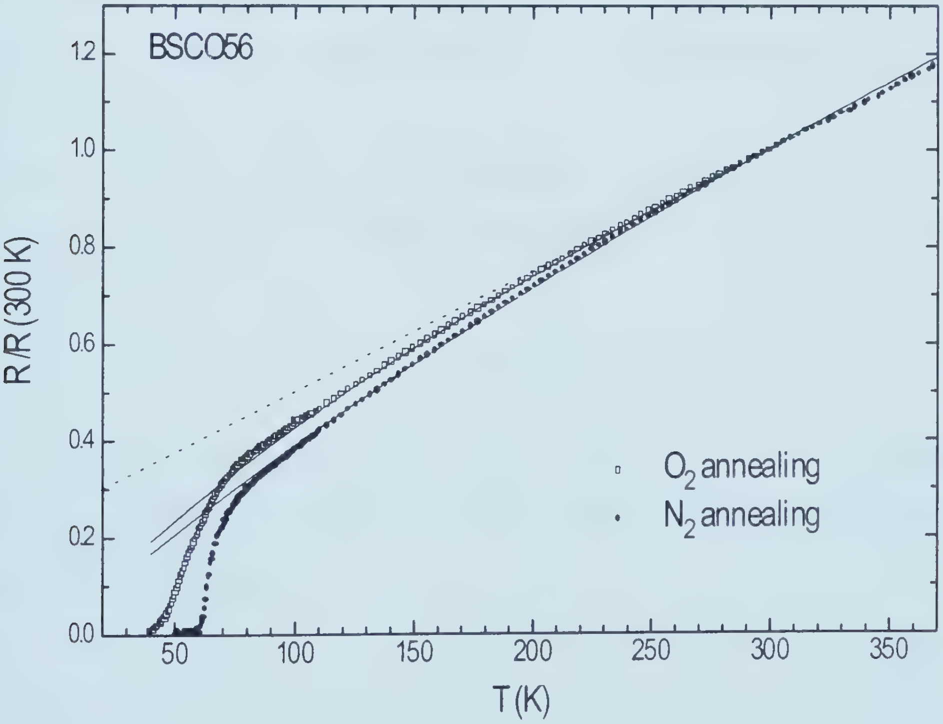

Fig. 5.7 Fittings (solid lines) for one sample after $N_2$ and then $O_2$ annealing. The dotted line represents linear-$T$ fit.

Suppose $\sigma_b$ is less sensitive to oxygen doping than $b$, so we set $\sigma_b = 0.0015$ in the fitting. As can be seen in the plot, the data closely agrees with this model over a wide temperature range. For comparison, a linear-$T$ fit to the high temperature part (~230-300 K) was also given. Two features in Fig. 5.5 are noticeable: (1) While resistance deviation from the linear-$T$ fitting is evident, it is well accounted for in the polaron model; and (2) Superconducting fluctuation is seen only very close to $T_c$ in the polaron fitting compared with the much higher onset temperature in the linear-$T$ case. The former can be understood in terms of single polaron conduction[‡], which involves scattering by phonons ($1/\tau_{\mathrm{ph}} \propto T$) and disorder-localized polarons ($1/\tau \propto T^2$). The total carrier density is temperature dependent due to disorder, $n \propto const. + bT$. Therefore, the resistance has the form of Eq. (5.1). The pseudogap could be too small to affect the scattering.

The results for three samples are shown in Fig. 5.6, all yielded mutual agreeable values of $b$. Fig. 5.7 shows the resistance data of one sample successively annealed in nitrogen and then oxygen atmosphere. $b$ was found to be 0.00286 and 0.00434, respectively, in agreement with the increasing of carrier density after oxygen annealing. In samples which exhibit anomalous kink near $T^* \sim 250$ K, similar fitting applies to the resistivity below the kink.

To further check the validity of this approach, we calculate the effective in-plane boson mass [156], $m = \pi\hbar^2/wa^2$, where the lattice constant $a$ =5.4 Å, $w$ is related to $T_c$ through

$$T_c = \frac{2w(n - n_L)}{\log \gamma^2}. \tag{5.3}$$

Take $T_c = 75$ K, $\gamma = 183$, and $(n - n_L) = 0.076$, we have $w = 2232.7$ K. Therefore, $m = 3.889 \times 10^{-30}$ kg $= 4.27\ m_e$. For YBCO, $m = 10\ m_e$. Thus, the present result may correspond to single polaron conduction.

---

[‡] I benefited from discussions with A. S. Alexandrov on this topic.

# Chapter 6

# Superconducting Fluctuation

The superconducting fluctuation above the transition temperature has been extensively studied [202-216]. In BSCCO whiskers, compared with YBCO, this phenomenon is especially significant because of the small sample dimension (~ 0.5 μm) along the *c*-axis, high anisotropy, and high crystalline quality. From resistivity measurement, superconducting fluctuation manifests as the rounding off transition onset and "excess conductivity" compared with linear-*T* high-temperature extrapolation. The theoretical basis for the analysis is the two-dimensional fluctuation theory proposed by Aslamazov and Larkin [202]. The excess conductivity is attributed to the fluctuating pairing above the mean field $T_c$ and is given by

$$\Delta\sigma = C\varepsilon^{-x}, \tag{6.1}$$

with

$$C = \frac{e^2}{16\hbar d}, \quad x = 1 \quad \text{for 2D}, \tag{6.2}$$

and

$$C = \frac{e^2}{32\hbar\xi_c(0)}, \quad x = \frac{1}{2} \quad \text{for 3D}, \tag{6.3}$$

where $\varepsilon = (T-T_{c0})/T_{c0}$ is the reduced temperature and $x$ the critical exponent. $T_{c0}$ is the mean field transition temperature. A dimensional crossover is expected at some characteristic temperature, although the width of the 3D region is narrow due to high anisotropy.

For layered superconductors with Josephson coupling between the planes, the in-plane excess conductivity due to thermodynamic fluctuation is given by the Lawrence-Doniach expression [217]:

$$\Delta\sigma_{LD} = \frac{e^2}{16\hbar s}\frac{1}{\sqrt{\varepsilon}\sqrt{\varepsilon+4J}}, \tag{6.4}$$

with $J = (\xi_c(0)/s)^2$, and $s$ is the interlayer spacing. The above equation suggests a dimensional crossover from 2D to 3D as $T$ decreases and approaches $T_{c0}$ at $T_0$:

$$\varepsilon_0 = (T_0 - T_{c0})/T_{c0} = 4J. \tag{6.5}$$

Thus, from the experimental values of $T_0$ and $T_{c0}$, we can find the coherence length, $\xi_c(0)$.

In performing fittings of resistivity data to the above models, two difficulties had been generally recognized: (1) identifying the mean field transition temperature, and (2) determination of normal-state resistivity $\rho_n$. $T_{c0}$ was defined by various methods such as midpoint transition, maximum of $d\rho/dT$, or resistance onset. Han *et al.* [215] adopted a scheme of plotting $\Delta\sigma^{-2}$ versus $T$ and finding $T_{c0}$ by extrapolating the linear-$T$ portion. $\rho_n$ is widely calculated by linearly fitting the resistivity at high temperatures and extrapolating to the lower range. This method is problematic when applied to samples which exhibit deviation at very high temperatures around 200 K. If pseudogap interferes between $T_c$ and room temperature, resistivity must change dependency on temperature above and below the anomaly, and such extrapolation is unjustified. In samples that possess linear-$T$ resistivity down to within a few tens of degrees of $T_c$, on the other hand, superconducting fluctuation is much less significant, meaning the sample quality is reduced. This problem is further complicated by the scenarios of the normal state, such as preformed pairing [218], which may influence the resistivity.

In good quality BSCCO whiskers, resistivity deviation often happens around 200 K, which makes linear extrapolation unacceptable. A careful check of many of our resistivity data shows that $d\rho/dT$ approximately follows a linear-$T$ relation over a sample-dependent temperature range of about 150 to 250 K. We therefore use a phenomenological polynomial fitting of the normal-state resistivity in this temperature region, avoiding the pseudogap anomaly. The $T_{c0}$ is determined from the maximum $dR/dT$. As it turned out, such a treatment resulted in good agreement with theoretical calculations, as well as $\xi_c(0)$ values very close to literature data.

Figure 6.1A shows a typical resistance result, together with linear-$T$ fitting near 300 K (dotted line) and polynomial fitting between 150 – 230 K (solid line): $R_N(\Omega)= -25.2 +3.667T - 2.21\times10^{-3}T^2$. A plot of $dR/dT$ vs. $T$, together with the linear-$T$ segment, is presented in Fig. 6.1B. Superconducting fluctuating appears at ~ 135 K if we adopt the polynomial $R_N$. This temperature is much lower than that in the linear fitting case, although it is still much higher than $T_{c0} = 87$ K. Fig. 6.2 gives plots of $\Delta\sigma/\sigma(300\ \text{K})$ vs.

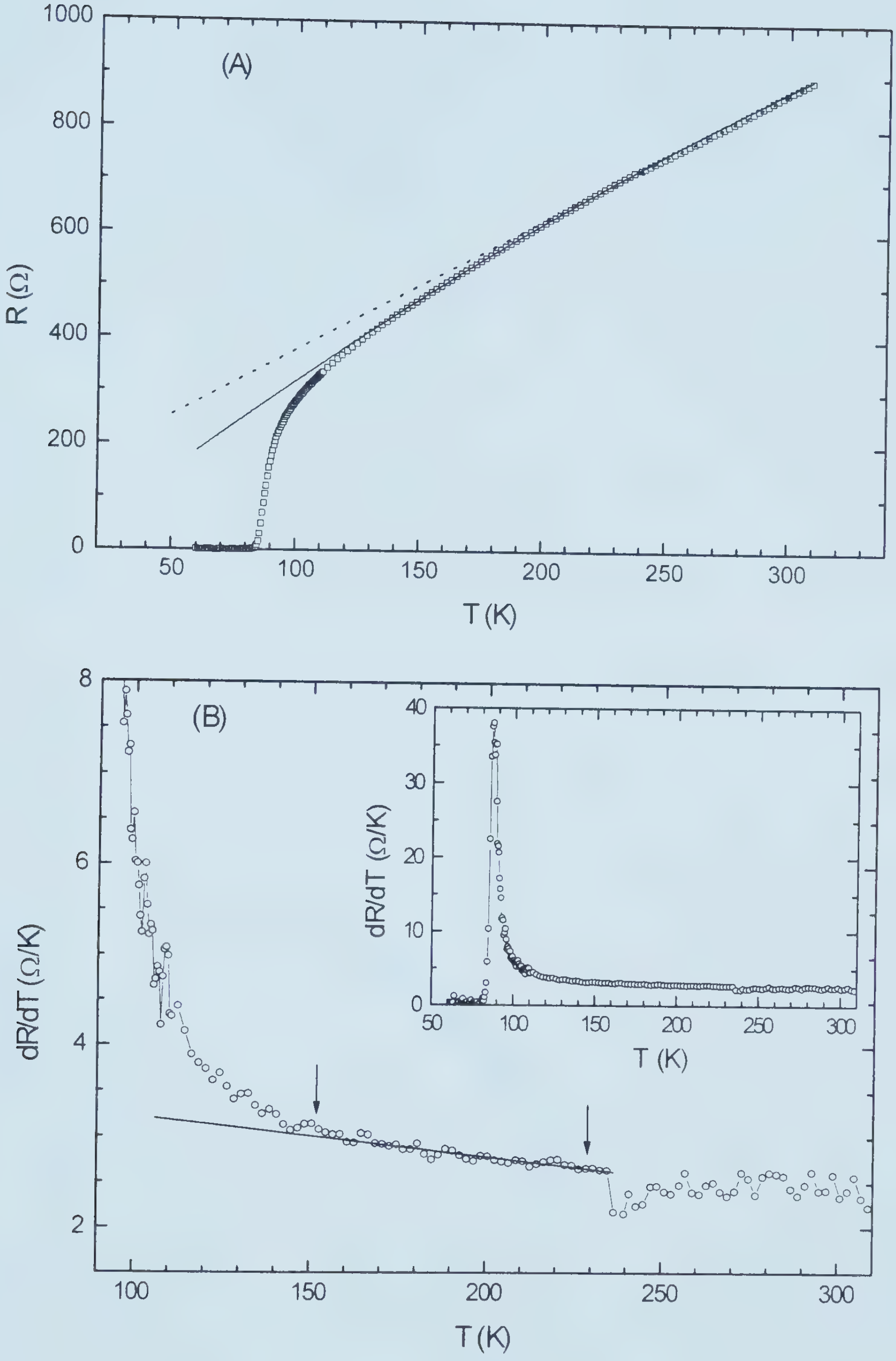

Fig. 6.1 (A) Resistance of a Bi-2212 sample. The dotted line is a linear fit at high temperature (260 – 310 K), and the solid line represents a quadratic fitting (150 – 230 K): $R(\Omega) = -25.2 + 3.667T - 2.21 \times 10^{-3}T^2$. (B) Plot of $dR/dT$ vs. $T$ for the data in (A). The arrows indicate the linear portion for the quadratic fitting. The anomaly near 235 K is evident. Inset: plot on full $T$ scale.

$\varepsilon$ for this and other samples. $\Delta\sigma$ is calculated from $\Delta\sigma = 1/\rho - 1/\rho_N$, where $\rho_N$ is the normal-state resistivity fitting as described. The two dashed lines of slope -1 and –1/2 correspond to fittings to Eq. (6.1) for x=1 and 1/2, respectively. As can be seen, there is a good agreement with the 2D fluctuation theory between $-3.8 \leq ln\varepsilon \leq -2.2$, i.e. $88.9 \leq T \leq 96.6$ K with $T_{c0}$ = 87 K. From exact resistivity measurement, we found the 2D fluctuation happens within a layer of effective thickness $d \sim 6$ Å, which is consistent with the thickness of the double $CuO_2$ layer (≈ 7 Å). A crossover to the very narrow 3D region ($x = 1/2$) is indicated by the arrow, where $ln\varepsilon \approx -4.11$. Thus $J = 4.096\times10^{-3}$ from Eq. (6.5), and we have $\xi_c(0)$ = 0.96 Å, in excellent agreement with the data from a sample of similar $T_c$ [215]. Since $\xi_c(0)$ is an important parameter and is usually difficult to determine, we perform similar fittings for five other samples. The result is listed in

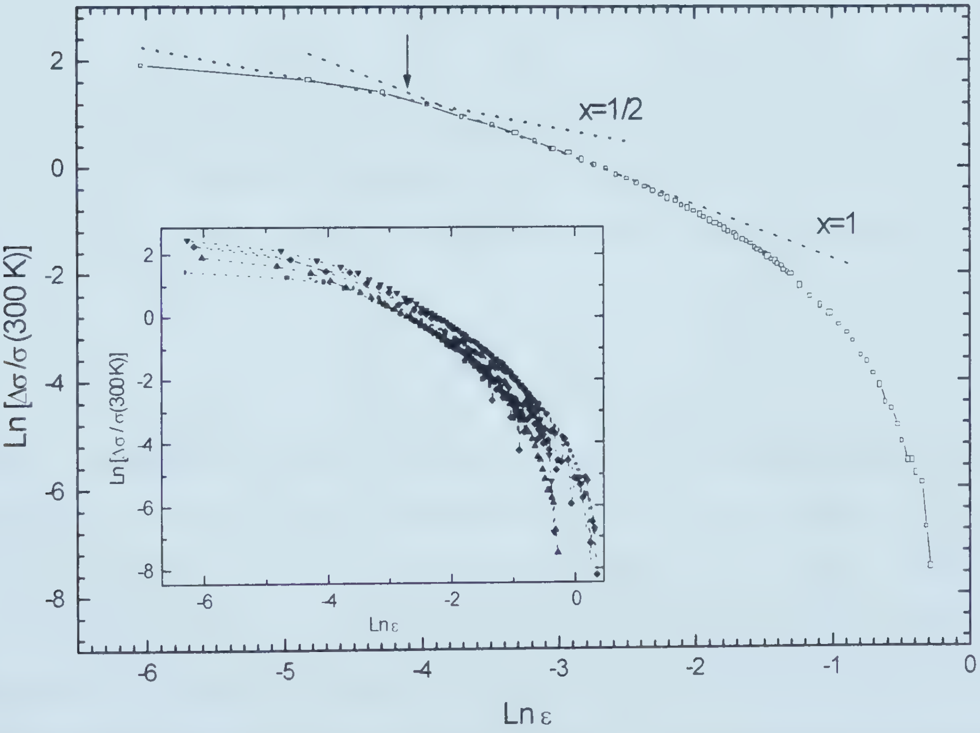

Fig. 6.2 Excess conductivity scaled by $\sigma$(300 K) versus reduced temperature for the sample in Fig. 6.1. The dashed lines are fittings of slope -1 and –1/2 to the relation: $\Delta\sigma \propto \varepsilon^{-x}$. The arrow indicates the dimensional crossover. Inset: five other Bi-2212 samples.

Table 6.1 $\xi_c(0)$, $T_{c0}$, and doping status of Bi-2212 samples.

| $T_{c0}$ (K) | $\xi c(0)$ (± 0.10 Å) | Doping status |
|---|---|---|
| 63 | 1.21 | Underdoped |
| 69 | 1.16 | Underdoped |
| 71 | 1.41 | Underdoped |
| 74 | 1.12 | Overdoped |
| 76 | 1.12 | Overdoped |
| 87 | 0.96 | Near-optimal |

Table 6.1. Also shown is the doping status deduced from annealing history. $\xi_c(0)$ seems to reach a minimum optimal $T_{c0} = 87$ K.

When the same procedure was applied to one Bi-2223 sample ($T_{c0}$ = 109.6 K), we found a linear region on the curve with a slope of –3/2, as shown in Fig. 6.3. The linear segment corresponds to the temperature range pointed by the dashed arrows in the inset plot of *R-T*. The solid arrow indicates the mean-field $T_{c0}$. In the Aslamzov-Larkin theory, the –3/2 exponent would correspond to one-dimensional fluctuation [219]:

$$\Delta\sigma = \frac{\pi e^2 \xi_0}{16\hbar S}\varepsilon^{-3/2}, \tag{6.6}$$

where $S$ is the cross-sectional area of the 1D wire. Such 1D fluctuation behavior had been reported in Bi-2223 [210] and Bi-2212 [220]. It was attributed to possible percolation path of Bi-2223 within the Bi-2212 matrix. However, this can not explain the same behavior in pure Bi-2212 crystals. An alternative interpretation is the incommensurate structure modulation along the *b*-axis in BSCCO materials [220], which results in 1D channels along the *a*-axis. Such 1D signature was only observed in perfect Bi-2212 crystals, as also confirmed in some of our samples.

We estimate the cross-sectional area of the 1D channel from the intercept of the linear line: $S = 0.1\ \xi_0\ \rho(300\ \text{K})$. If $\rho(300\ \text{K}) = 350 \times 10^{-8}\ \Omega$ m and $\xi_0 \approx 0.1$ Å, then $S$ = 350 Å$^2$. This area agrees with that of the superstructure channel ($4.7b$ × thickness of triple CuO$_2$ layer). Therefore, the 1D fluctuation seems to reflect the structure

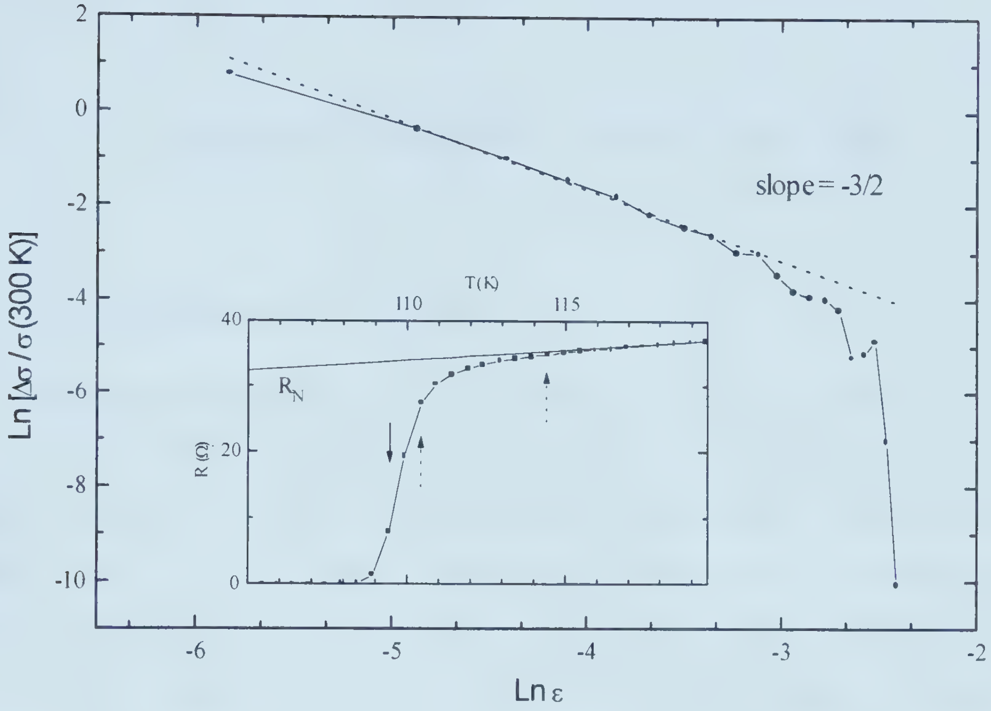

Fig. 6.3 Excess conductivity of a Bi-2223 sample. The dotted line is a linear fit of slope –3/2. Inset: $R$-$T$ data and the normal-state extrapolation ($R_N$) near the fluctuation region. The solid arrow points to the mean-field $T_{c0}$ and the dashed ones show the temperature range corresponding to the linear segment in the main panel.

modulation. However, there is an ambiguity in assigning the value of $\xi_0$, and if the cross-sectional area is much larger that the estimated value, the percolation picture can not be ruled out.

In summary, the superconducting fluctuation was analyzed using the classical theory of layered superconductors. A clear 3D fluctuation regime appears above ($T_{c0}$ + 2 K) on an interval of less than 10 K. Above this region, the fluctuation is two-dimensional. From the crossover temperature, the out-of-plane coherence length was calculated. The 1D behavior was observed in a Bi-2223 sample and some other good quality Bi-2212 samples. This seems to be associated with the superstructure along the $b$-axis which gives rise to one-dimensional channels. Finally, since the coherence length data is scarce in the literature, superconducting fluctuation thus provides another method to determine this important parameter.

Chapter 7

# Transport Properties of the Mixed State

## 7.1. General features of the mixed state

A type-II superconductor enters the mixed state when the external magnetic field exceeds the lower critical field ($H_{c1}$). According to Abrikosov theory, the field penetrates the superconductor in the form of flux lines, each of them carrying a flux quanta, $\Phi_0 = 2.07 \times 10^{-7}$ G cm$^2$. Supercurrent circulates around the normal core (of radius $\xi$) like a vortex. Spatially, the flux lines (vortices) form a triangular or square lattice. The imperfections in the material, such as dislocations, vacancies, grain boundaries, etc., can act as pinning centers for vortices and thus maintain the zero-resistance state. The depinning of flux lines due to increased Lorentz force above the critical current, or as a result of thermal activation, invokes energy dissipation and hence onset of resistance.

The flux dynamics has been greatly enriched with the discovery of high-$T_c$ cuprates.

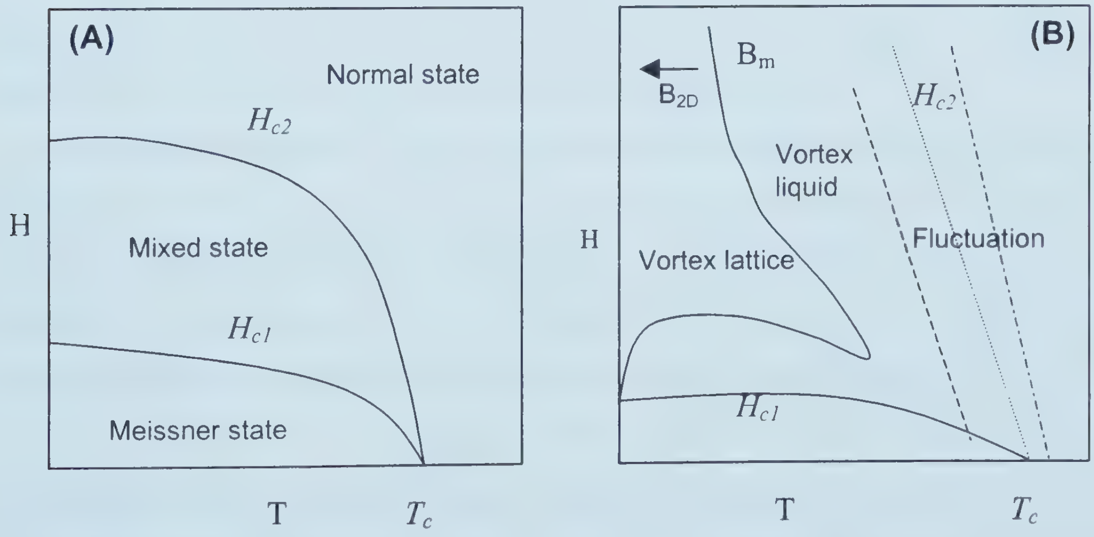
(A)
Normal state
$H_{c2}$
H
Mixed state
$H_{c1}$
Meissner state
T
$T_c$
(B)
$B_m$
$B_{2D}$
$H_{c2}$
Vortex liquid
H
Vortex lattice
Fluctuation
$H_{c1}$
T
$T_c$

Fig. 7.1 (A) Phase diagrams of conventional, and (B) high-$T_c$ (BSCCO) superconductors.

because of the layered structure (anisotropy), new pinning mechanisms, higher $T_c$ and $H_{c2}$, and small coherence length (profound fluctuation and transition broadening). The novel features give rise to a much more complex phase diagram in the mixed state than that of conventional superconductors [221-227]. Figure 7.1 schematically shows a comparison of the phase diagrams of conventional and high-$T_c$ superconductors. In addition to the Abrikosov lattice (vortex solid), there exist two regions of vortex liquid bordering with the $H_{c1}$ and $H_{c2}$ lines in the $H$-$T$ phase diagram for cuprates (e.g. BSCCO and YBCO).

Determined from the Lindemann criterion $\left\langle u^2(T_m)\right\rangle_{th} \approx {c_L}^2 {a_0}^2$, the melting line in the intermediate-field range ($H_{c1} \perp B \perp H_{c2}$) takes the form [222]

$$B_m \approx (5.6c_L^4 / G_i) H_{c2}(0)[1 - T/T_c]^2,$$

where the Ginzburg number $G_i = (T_c \gamma / H_c^2 \xi^3)^2 / 2$, and the Lindemann number $c_L = 0.1 - 0.4$. It is very interesting that the vortex lattice can melt not only in the conventional sense (rising temperature) but also at low fields close to $H_{c1}$ (Fig. 7.1B). As the field decreases, the inter-vortex distance ($\propto 1/\sqrt{H}$) increases and eventually exceeds the London penetration depth $\lambda$. On the other hand, the vortex-vortex interaction is exponentially small in this region, consequently the shear modulus $c_{66} \propto exp(-a_0/\lambda)$ decays rapidly, leading to the melting of the flux-line lattice [222].

A dimensional crossover is also proposed for the melting transition [222] at a characteristic field ($H_{c1} \perp B \perp H_{c2}$): $B_{2D} \approx (\pi\Phi_0 / \Lambda^2)\, ln(\Lambda/\xi)$, with $\Lambda = \gamma s$ denotes the Josephson screening length. At low fields ($<B_{2D}$), the vortices retain as line-objects and the melting is of the 3D type ($G_i \sim 1$). At high fields $B > B_{2D}$, the melting transition is quasi-two-dimensional and approaches the field independent temperature:

$$T_m^{2D} = \varepsilon_0 d / 4\sqrt{3}\pi \approx 25\ \mathrm{K}.$$

The layered nature of cuprates further modifies the structure of a vortex: for H// $c$, it is composed of pancake vortices residing in the $CuO_2$ planes and threaded by the flux line. The thickness of such a pancake vortex is about $2\lambda_{ab}$. The vortices in the same

layer repel each other, and those in adjacent planes attract each other. When the field is perpendicular to the $c$-axis, the vortex core runs between the $CuO_2$ layers, forming the so-called Josephson vortices or Josephson strings because the circulating supercurrent occurs through Josephson tunneling. The width of a Josephson vortex core is $\lambda_J = \gamma s$, and thickness $s$ = layer spacing. The ratio $\lambda_J/s = \gamma = \xi_{ab}/\xi_c$ is equal to the anisotropy factor.

The actual vortex state is more complicated than the above picture, which involves such concepts as flux entanglement (flux-line cutting and rejoining at different $CuO_2$ planes), vortex glass, multi-critical points, etc. The phase diagram had been extensively explored by various experimental techniques including magnetization [228-233], transport [234-240], thermodynamics [241-244], mechanical methods [245-247], NMR [248], μSR [249, 250], and direct observation of melting [251-253].

In resistivity measurements, the nature of the flux matter and pinning mechanisms play important roles in shaping the temperature and field dependence of magneto-resistance. Some typical transport behavior can be identified in the mixed state. Resistivity jumps appear at the first-order melting of vortex lattice [234] in high quality crystals. For strong pinning materials, thermally activated flux flow (TAFF) [254] occurs when the pinning potential is overcome as the temperature is increasing. The resistivity is well described by the Arrhenius law: $\rho = \rho_0\, exp(-U/k_BT)$. Free flux flow [255] behavior happens in vortex liquid or when the flux lines are depinned and undergoes a viscous flow. The flux flow resistivity follows the Bardeen-Stephen theory, $\rho_f = \rho_n H / H_{c2}(T)$. This simple relation shows that the dissipation is due to the normal-state vortex core (single core area ($\Phi_0/H_{c2}$) multiplies the vortex density ($H/\Phi_0$)). The viscous drag due to the induced electric field is expressed in terms of a viscosity $\eta = B_{c2}\Phi_0/\rho_n$.

Transport measurements ($R$-$T$ and $I$-$V$) were carried out on both Bi-2212 and Bi-2223 whiskers. Because of high sample quality, i.e. single crystalline nature and very low defect concentration, we had obtained many good results, especially clear signature of free flux flow that is otherwise very hard to observe. Temperature dependence of critical current was also studied.

## 7.2 Activation energy

Figure 7.2A shows a typical set of $R$-$T$ data for fields applied along the $c$-axis of a Bi-2212 whisker ($T_c \approx 76$ K). Fig. 7.2B is the Arrhenius plot of the same data. The dashed lines in both graphs represent the fitting to the TAFF model: $R=R_0exp(-U/T)$, with $U = 1000 \times$ slope. As can be seen from the figures, $R$-$T$ follows the thermal activation behavior over a wide temperature range. Above some temperature, near the "elbow" of the transition, the thermal energy exceeds pinning potential and dissipation rapidly increases with temperature. Free flux flow behavior is expected to dominate in this regime, which will be discussed later. As usual, $U$ decreases with increasing field. Fig. 7.3 shows the $U$-$H$ dependence for the data in Fig. 7.2, which confirms the power-law relation: $U \sim H^{-\alpha}$. A crossover near 0.5 T is evident, which separates two segments of field dependence: $\sim H^{-1/3}$ and $\sim H^{-1/6}$. This is in good agreement with the reported results [254,256-258].

The fitting in Fig. 7.2B shows that $U$ is *unlikely* to be temperature dependent. In the pinned-liquid theory proposed by Vinokur *et al.* [259], the activation barrier $U_{pl}$ of TAFF behavior is dependent on both $T$ and $H$ since the TAFF mechanism is caused by entanglement of vortices. The flux cutting and rejoining result in a highly viscous plastic motion and the activation barrier does not depend on the pinning potential. Thus the result in Fig. 7.2 can be interpreted as due to the thermal depinning of vortices and $U$ is related to the pinning potential. This situation should apply to samples with high density of pinning centers. In fact, the samples studied here had been thermally annealed which could cause surface degradation as examined by scanning microscopy. Such surface defects (submicrometer-sized pits) may act as effective pinning centers. Indeed, in some other samples, we found that a constant $U$ cannot give satisfactory TAFF fitting. Moreover, in as-grown whiskers of very high crystalline quality, TAFF behavior similar to that in Fig. 7.2 is far less significant, which further proves the pinning origin of the observed flux motion. It is interesting to identify the depinning temperature $T_p$ where resistance starts to appear. The $H$-$T_p$ data are plotted in Fig. 7.4, which well fits to a power-law relation: $H = H_0(T_p/T_c)^{-n}$, for $H \sim 1$ $T$ with $H_0$ and $n$ being sample (hence pinning) dependent. At low field, the curves tend to merge which

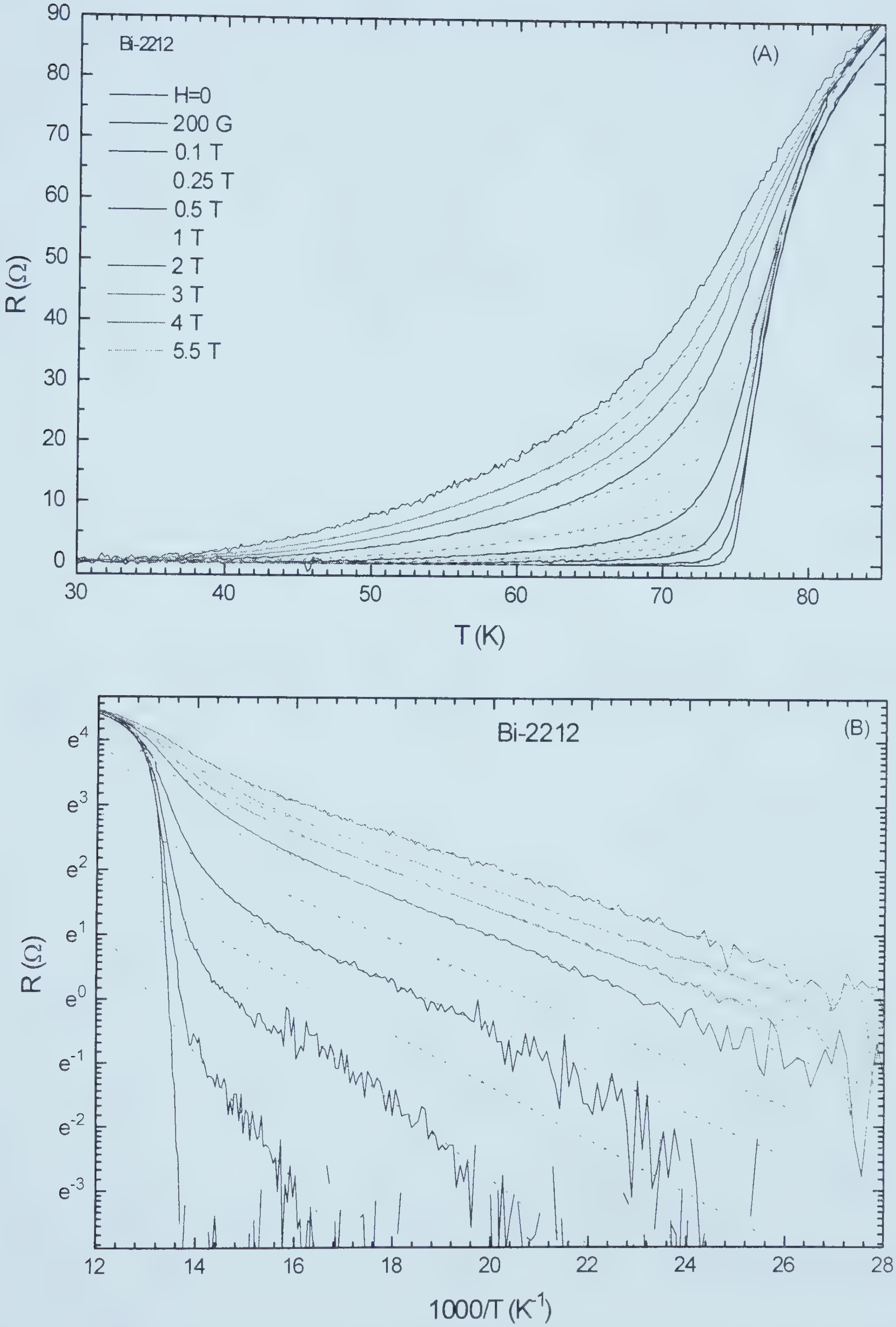

Fig. 7.2 (A) Mixed-state resistivity of a Bi-2212 sample in fields applied along the *c*-axis. (B) The Arrhenius plot of the data in (A) and the TAFF fitting (dashed lines): $R = R_0 exp(-U/T)$.

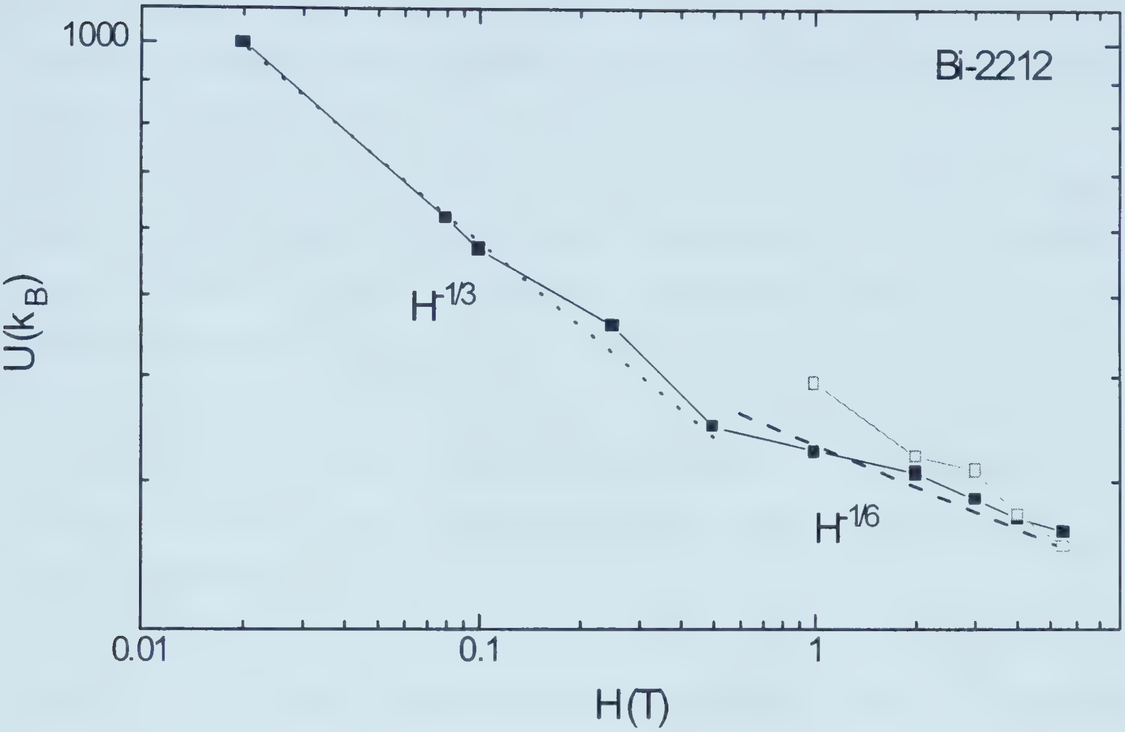

Fig. 7.3 Field dependence of the activation energy $U$. The two dashed lines represent $U \propto H^{-1/3}$ and $H^{-1/6}$ relations, respectively. Open symbols are from another sample.

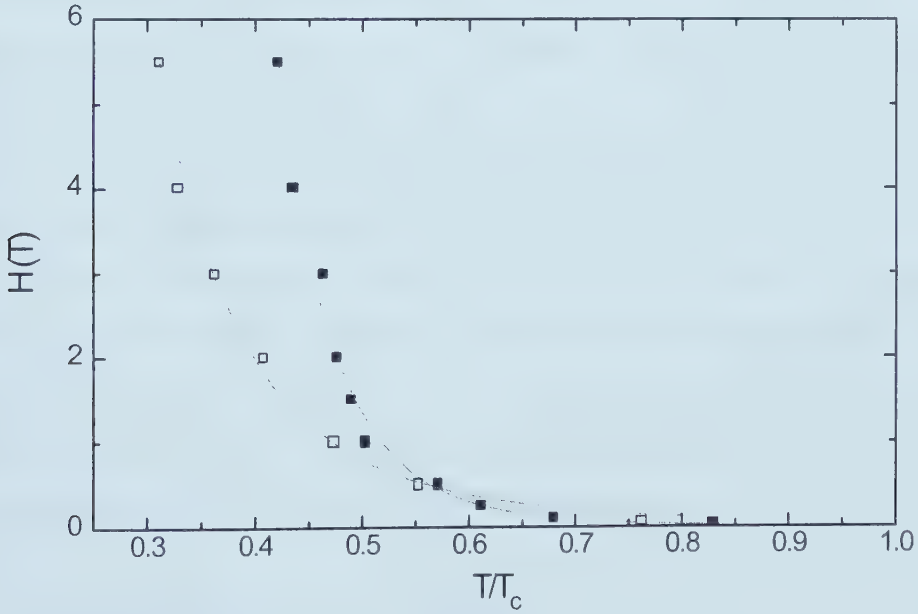

Fig. 7.4 Field-dependent resistance onset temperature where vortices start to move. Solid lines are fits to $H \propto (T/T_c)^{-n}$.

means depinning is mainly caused by thermal fluctuation without much influence from inter-vortex interaction. This $H$-$T_p$ dependence is different from the case of vortex-solid melting [260], where $T_p \sim (\Phi_0^3 Hm/M)^{1/2}/(2\pi\kappa)^2$.

Next we show the similar measurement results from Bi-2223 whiskers. Again for thermal annealed samples, $R$-$T$ exhibits TAFF behavior with $U \sim H^{-1/2}$, as shown in Figs. 7.5 A and B. Obviously $U$ is related to the inter-vortex spacing. The same field dependence was also found for $H//ab$ in Bi-2212 [254] and in Bi-2223 [257, 258]. With the decreasing of field, TAFF becomes less and less dominant and is limited only to the low temperature tip. This can be understood in terms of the much higher $T_c$ and the softening of the vortex lattice with decreasing $H$. The latter point is consistent with the $U \sim H^{1/2}$ dependence.

A general form of field dependent activation energy had been established, $U \sim H^{-\alpha}$, with $\alpha = 1/6, 1/3, 1/2$, and 1 depending on pinning mechanisms. The $1/\sqrt{H}$ dependence was associated with the plastic deformation of the dislocations in the flux line lattice [261], $U = \mu_0 H_c^2 4\pi\xi^2 ln\kappa(\Phi_0/B)^{1/2}$. Tinkham [262] interpreted the $1/H$ dependence in YBCO in terms of shearing of the vortex lattice, instead of plastic deformation. Such $1/H$ behavior seems to be common in YBCO [263].

Since the intrinsic pinning energy is smaller in cuprates with higher anisotropy and shorter coherence length [262], thermally activated flux motion happens down to the lowest temperature in highly anisotropic Bi and Tl cuprates. This explains why vortex lattice melting, manifested as resistivity jumps, is difficult to observe in these materials than in YBCO (with about ten times higher $U$). If *weak* pinning is introduced by ion irradiation, such resistivity jump due to sudden increase of shear viscosity in the vortex liquid can be observed in Bi-2212 [264]. In clean samples, one often sees a thermal activation and crossover to flux flow due to vanished pinning energy as the temperature keeps increasing. Such behavior is discussed below.

## 7.3 Crossover behavior in flux motion

As was mentioned, in as-grown Bi-2212 whiskers which are in the clean or

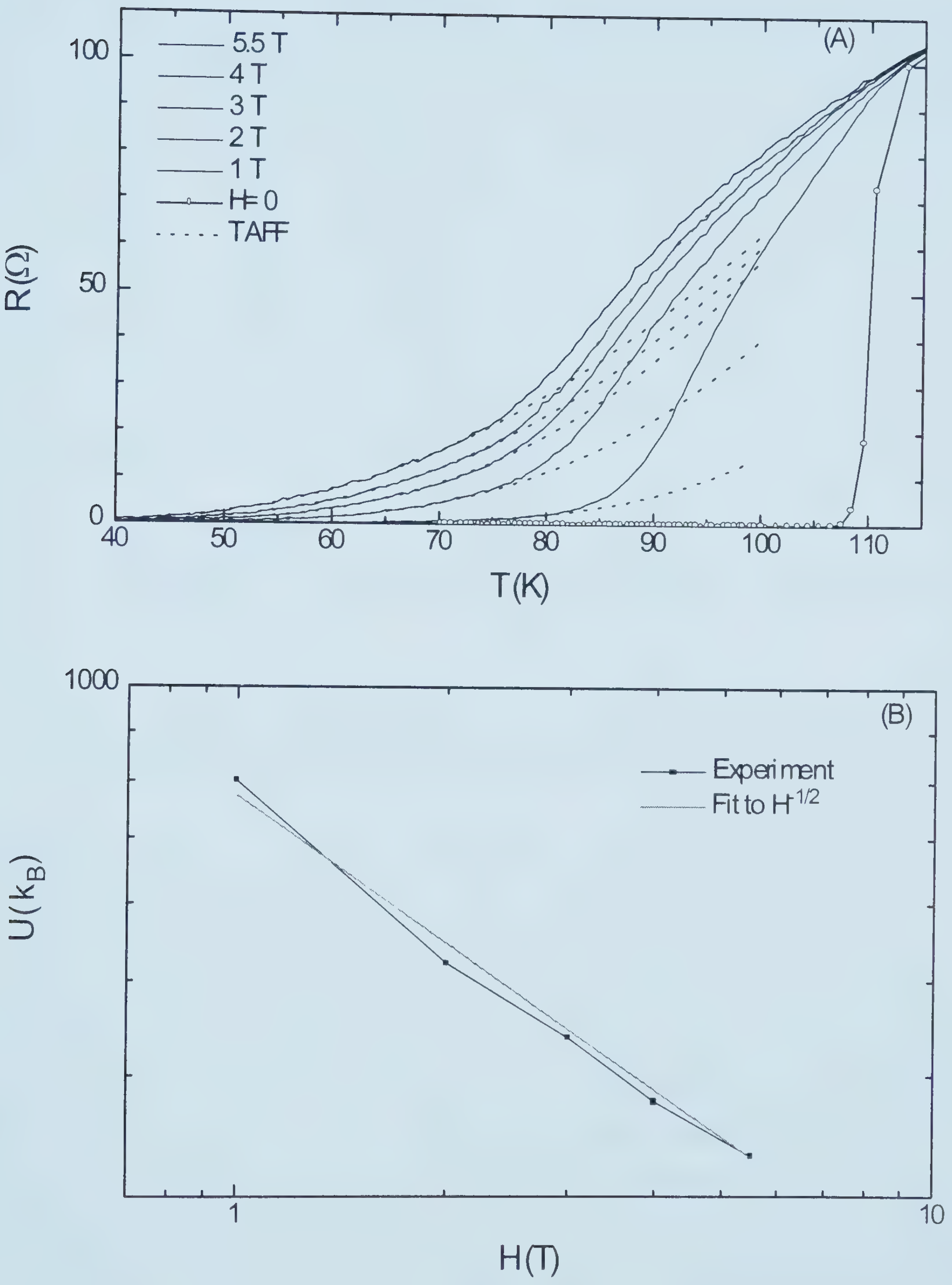

Fig. 7.5 (A) Magnetoresistance and TAFF fittings (dashed lines) of a typical Bi-2223 single crystal. (B) Field dependence of the activation energy.

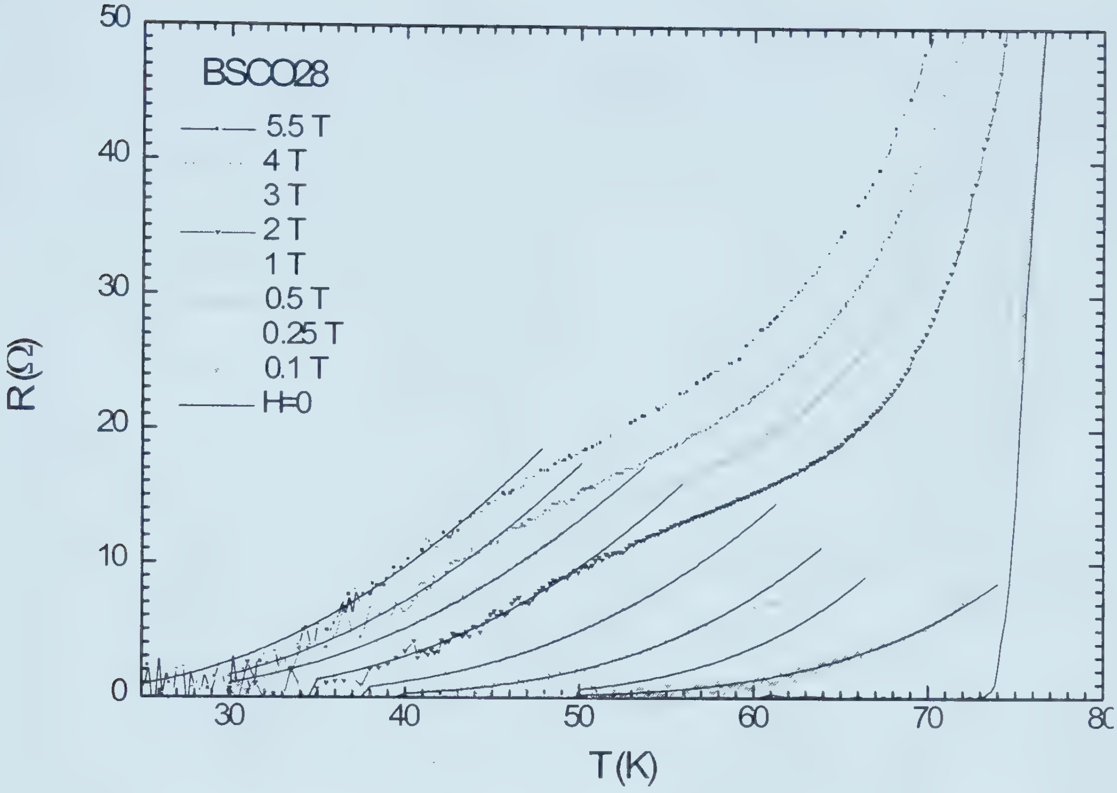

Fig. 7.6 Mixed-state resistance of an as-grown Bi-2212 whisker. Crossover in flux motion is evident as temperature increases. The solid lines are fittings to activation-type flux flow with temperature and field dependent barrier $U(T,H)$ (see text).

superclean regime in terms of vortex dynamics, TAFF behavior with $T$ and $H$ independent activation energy is not common. A crossover in $R$-$T$ at low temperatures is often observed, as shown in Fig. 7.6. As $T$ increases, vortices start depinning and resistance appears. $R$ seems to follow an activation behavior up to a characteristic temperature, $T_x$, above which $R$ bends down to a smaller slope, resulting in a "foot" near $T_x$. Such a crossover is more evident in the semilogarithmic plot of another as-grown sample in Fig. 7.7. Similar phenomena have been analysed by Batlogg *et al.* [265], who ascribed the "foot" to TAFF with temperature dependent activation energies. $U(T)$. Above the crossover temperature, the pinning potential vanishes ($U < k_BT$) and free flux flow is expected. We tried to fit the resistance to the Bardeen-Stephen theory of free flux flow: $R_f = R_N \, H/H_{c2}$, where $R_N$ is the normal-state extrapolated linear-$T$ resistance and $H_{c2} = \beta \, (T_c-T)$. The result is shown by the dashed lines in Fig.7.7. The fitting is excellent over a very wide temperature range (51 – 78 K for $H$ = 5.5 T). The value of $\beta$ is about 0.8 to 1.4 T/K increasing with field, which agrees with liteature data

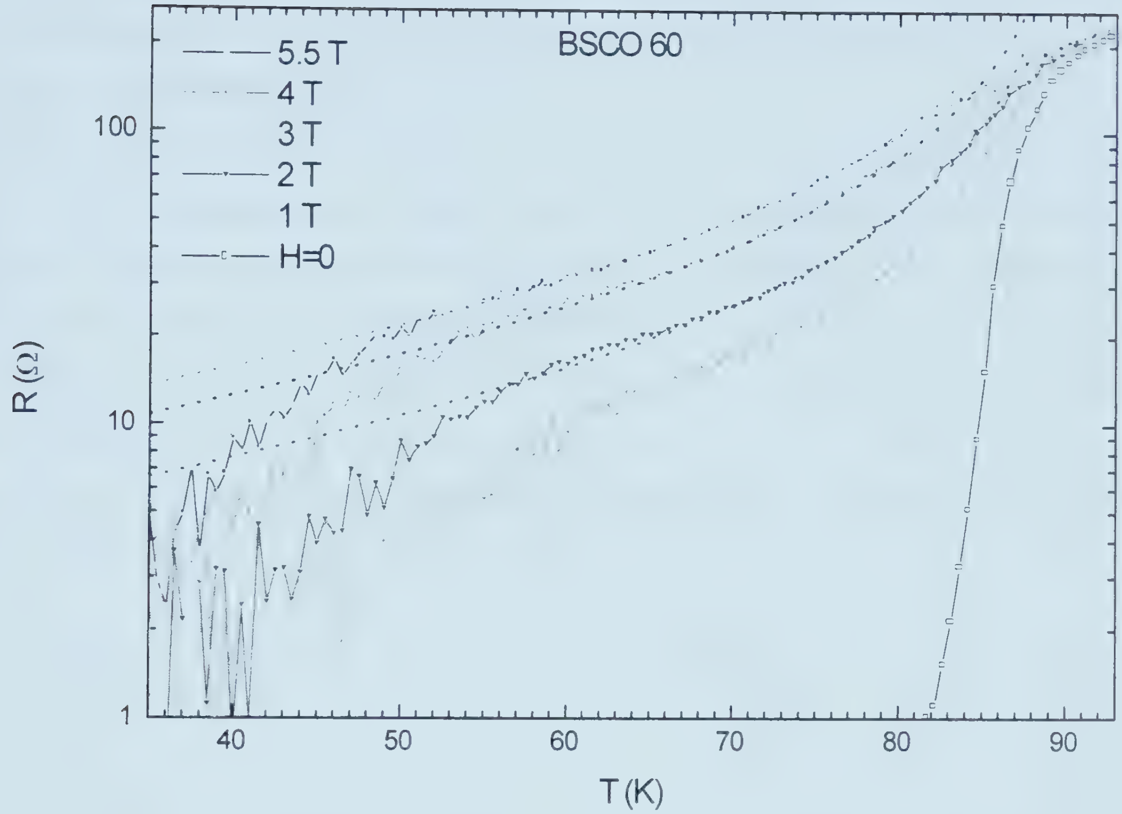

Fig. 7.7 Crossover behavior in flux motion of a Bi-2212 sample. The dashed lines are fittings to the Bardeen-Stephen free flux flow model: $R_f = R_N H / H_{c2}$.

(0.75 T/K) [266]. The fact that one single $\beta$ is not good for all fields further shows the more realistic temperature dependence of $H_{c2}(T)$.

When a similar fitting procedure was applied to the data in Fig. 7.6, pure free flux flow fitting was not achieved. This suggests that the vortex liquid is entangled and results in effective pinning in the liquid state as proposed by Vinokur *et al.* [259]. We notice the $T_c$ of this Bi-2212 sample is about 78 K, lower than that of the sample in Fig. 7.7, which is near the optimal 90 K. The difference in oxygen content may also cause the different pinning in the samples.

The pinned-liquid scenario [259] predicts a TAFF-like resistivity at low temperature:

$$\rho_{pl} = \rho_0 \exp(-U_{pl}/k_B T),$$

with a plastic barrier, $U_{pl} \sim \Phi_0^2 a(1-T/T_c)/8\gamma\pi^2\lambda_L(0)^2$, where $a \sim (\Phi_0/H)^{1/2}$ is the intervortex spacing. The effective pinning arises when the characteristic "smoothing time", $\tau_{pl}$, of plastic deformation becomes longer than the characteristic pinning time

$\tau_{pin}$. The liquid nature of very viscous system manifests only at time scales larger than $\tau_{pl}$. As temperature increases, $\tau_{pl}$ drops exponentially, $\tau_{pl} \sim \tau_{ph} exp(-U_{pl}/T)$, and crossover to unpinned state happens when $\tau_{pl} \approx \tau_{pin}$.

The low temperature tails in Figs. 7.6 and 7.7 were fitted to this model and the result is as shown by the solid lines. Indeed, the *R-T* data agree with this picture of highly viscous vortex liquid. Moreover, the plastic barrier shows a nearly $H^{-1/2}$ dependence as is expected. The extracted $U_{pl}$-$H$ data is plotted in Fig. 7.8. At higher fields, a good fit was obtained for $U_{pl} \propto H^{-\alpha}$ with $\alpha = 0.42$. Similar behavior and crossover at low fields were reported for Bi-212 [267] and Bi-2223 films ($\alpha$ = 0.5) [268]. In electron-inradiated YBCO, $\alpha = 0.7$ [269, 270], whereas more stronger $1/H$ depedence was found in samples containing columnar defects [271].

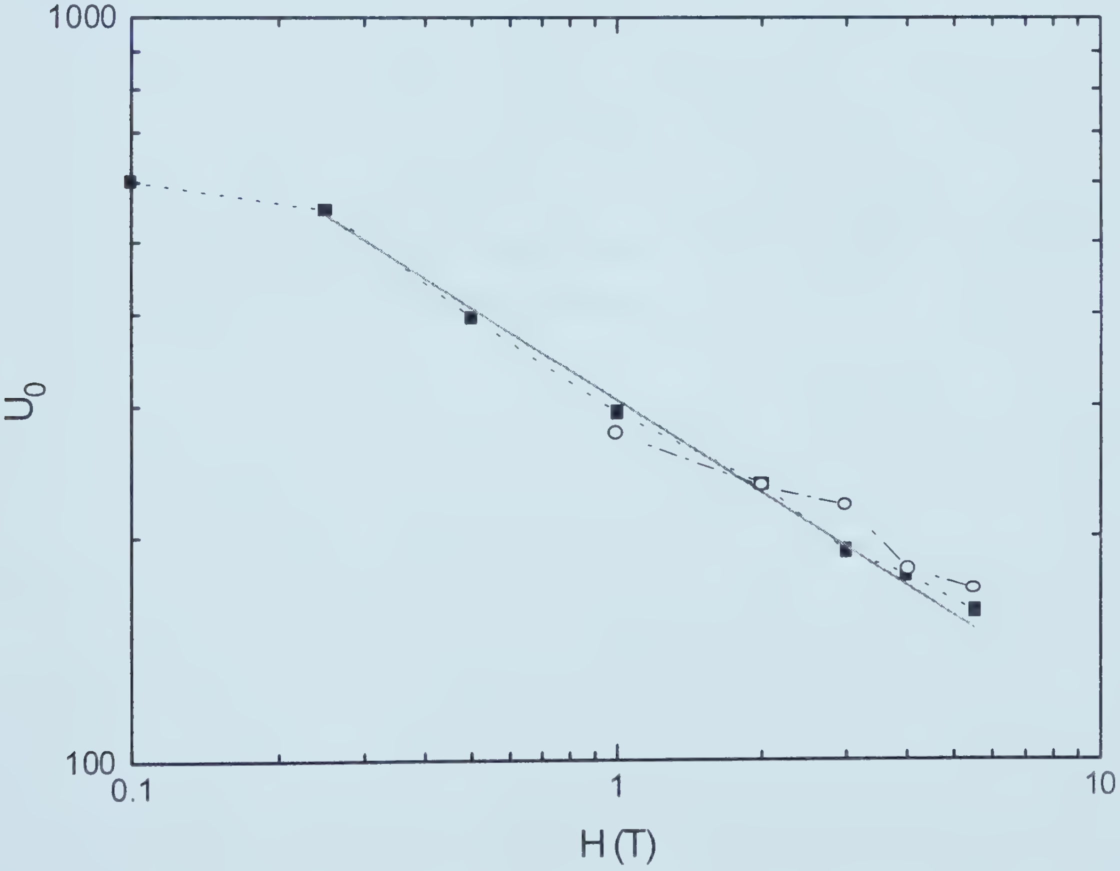

Fig. 7.8 Field-dependent activation energy $U_0$ in $U(T,H) = U_0(H)(1-T/T_c)$, fitted from the data in Fig. 7.6 (solid squares) and Fig. 7.7 (circles). The solid line represents a fit to $H^{-0.42}$, and the dashed lines are guides to the eye.

For cleanYBCO, it had been shown that the resistivity of vortex liquid follows this viscous behavior [272]. However, in similar vortex melting transition of untwinned YBCO [234], it was demonstrated [273] that the vortex liquid obeys the Bardeen-Stephen model. This discrepancy may come from the slightly different melting temperatures in the two works. Oxygen vacancies in clean samples had been shown to be important pinning centers [274-276]. The same situation explains the various observations in the present work. For the sample in Fig. 7.6, the resistance above the crossover may consists of both contributions of free flux flow and of activation of the entangled liquid.

In summary, various flux flow regimes had been observed from Bi-2212 and Bi-2223 single crystals. When the pinning density is high, usually in thermally annealed samples with evaporated pits on the surfaces, activation type flux flow dominates a wide range of the mixed state. In as-grown samples, on the other hand, an intrinsic TAFF-like behavior first appears at low temperatures, which was interpreted by the activation in the highly viscous vortex liquid. The dissipation then crosses over to another regime as temperature increases. This regime can either be fitted to the pure free flux flow behavior (the classical Bardeen-Stephen model) or possibly a combination of free flux flow and activation of the pinned liquid.

## 7.4 Critical current measurement

To gain some understanding of the curent-carrying capability and pinning mechanism of BSCCO whiskers (cross-section area less than 10 μm$^2$), $I$-$V$ characteristics were measured over wide temperature ranges. The very low contact resistance (< 1 Ω) makes it possible to accurately measure the voltage with a resolution better than 0.1 μV. Therefore, the ambiguity in selecting a criterion (usually 1 μV) for determining the critical current is eliminated. The lowest $I_c$ measured is 10 nA which is the limit of the current source.

Figure 7.9 shows the result of $J_c$-$T$ measurement in zero field. At $T$ =74 K, $J_c \approx 3.5 \times 10^8$ A/m$^2$, which is comparable with that of YBCO thin films [277]. The resistivity data revealed the sample is composed of two phases corresponding to Bi-2212 and Bi-2223 ($T_c$ = 82 and 98 K, respectively). Therefore $J_c$-$T$ dependence is limited by the Bi-2212 phase as shown in the figure. The irregular change of $J_c$ with $T$ reflects the

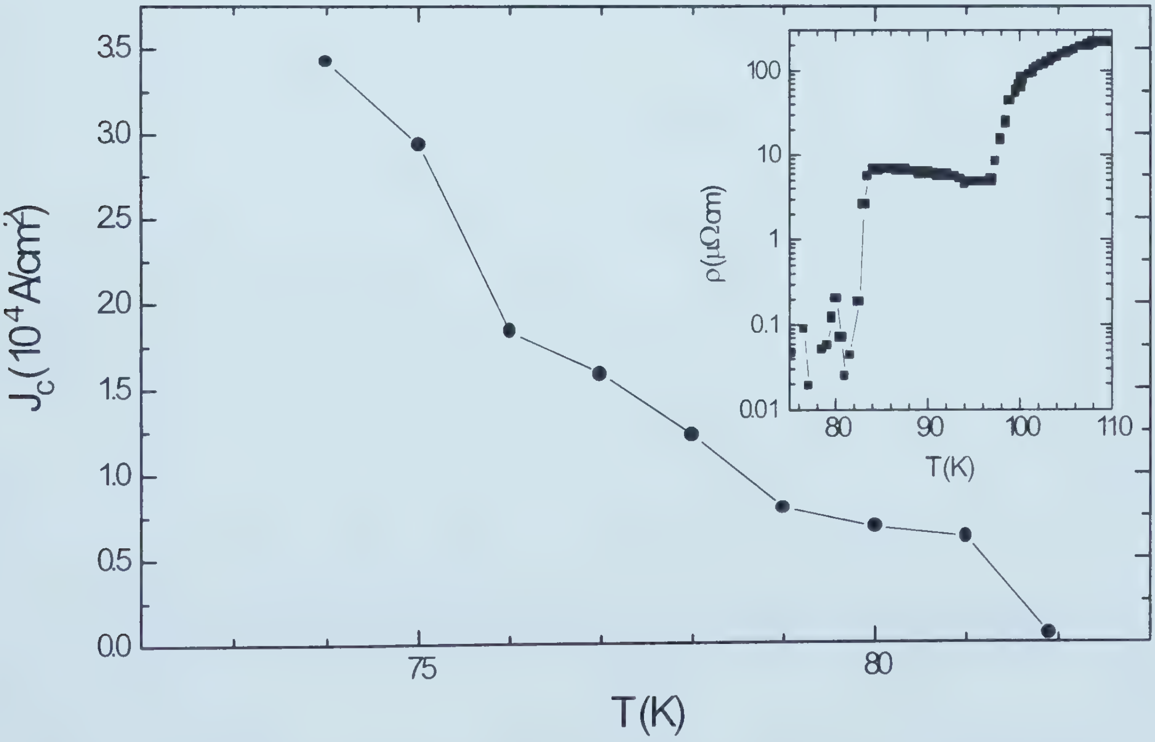

Fig. 7.9 Temperature dependence of critical current of a BSCCO whisker. The resistivity data (inset) reveals a mixing of Bi-2212 and 2223 phases.

filamentary structure. Nevertheless, the "concave" feature of $J_c(T)$ near $T_c = 82$ K is evident. This seems to agree with the Ginzburg-Landau-like behavior, $J_c \propto (T_c - T)^{3/2}$. In another pure Bi-2212 whisker ($T_c = 74$ K), $I_c$ was precisely measured from 2.2 mA down to 10 nA in the temperature range 25 – 75 K and a field of 200 G, together with zero-field data down to 5 K. The result is presented in Fig. 7.10. The $I_c$-$T$ curve is composed of segments and an overall fitting is not straightforward. At temperatures below 60 K, $I_c$ follows the GL depairing critical current very well. The dotted line in Fig. 7.10 shows the fitting of $I_c(\mathrm{mA}) = 6.14\,(1-T/T_c)^{3/2}$ for $H$=0. A crossover to $I_c \propto (1-T/T_c)$ below ~ $0.4T_c$ is clear. Between 60 K and $T_c$ for 200 G data, two step structures were observed at 62 K and 70 K, as shown in the insets of Fig. 7.10. Such steps usually appear as plateaus in magnetically measured critical current [277]. However, a closer view shows that these are concave steps rather than $T$-independent. The step below 70 K can be fitted to a "local" Ginzburg-Landau-like behavior: $I_0(T_c-T)^{3/2} + I_b$. This again seems to imply filamentary

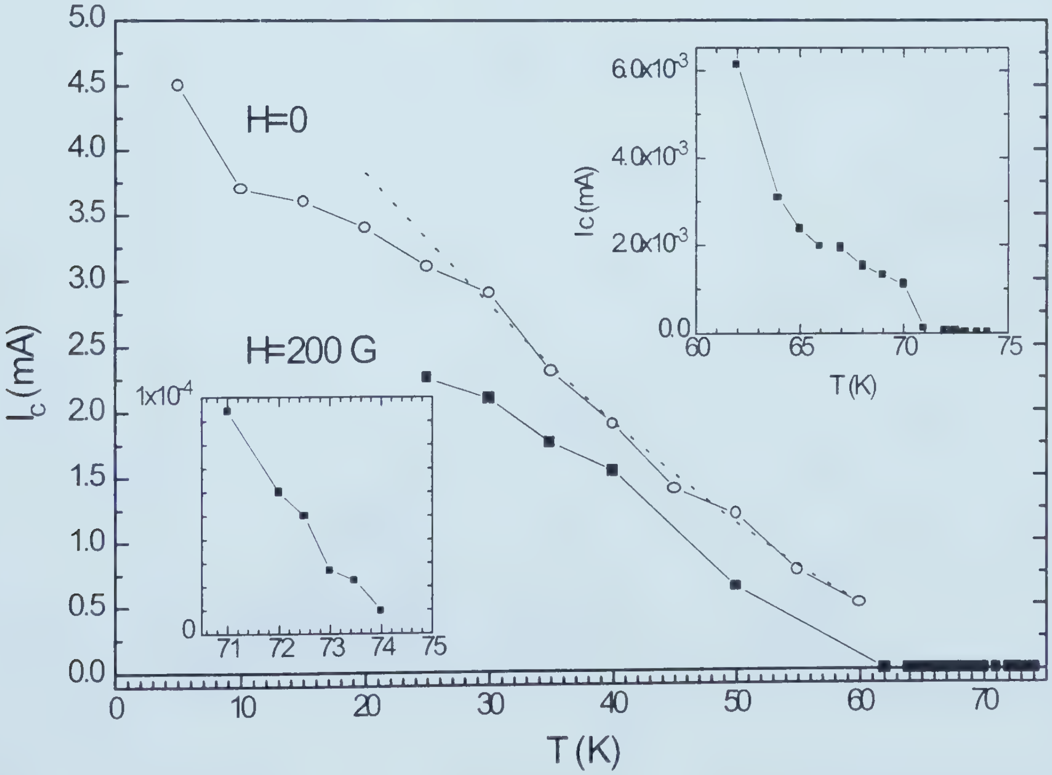

Fig. 7.10 Critical current of a Bi-2212 whisker for field $H = 0$ (open circles) and 200 G (solid squares). The two insets successively display the detailed features close to $T_c = 74$ K. The dotted line is a fit to $I_c = 6.14(1-T/T_c)^{3/2}$ mA.

superconducting as discussed below.

We estimate the quasilinear-$T$ dependence at low temperature by using the London penetration model [278]:

$$J_c(A/m^2) = 5.83\times10^{20}\frac{1}{\lambda_L^2 d}\left(\frac{m_{//}^*}{m_{\perp}^*}\right)^{1/2}$$

where $\lambda_L$ and interlayer spacing $d$ are in Å. For Bi-2212, $\lambda_L(0) = 2100$ Å, $d = 15$ Å, and $(m^*_{//}/m^*_{\perp})^{1/2} = 1/183$ (our measurement), this gives $J_c = 4.8 \times 10^{10}$ A/m$^2$. A linear fitting to the low temperature portion of the zero-field data in Fig. 7.10 yields $I_c$=4.5 $(1-T/T_c)$ (mA), which converts to $J_{c0}$ = 4.5 mA/ (0.48 × 5) μm$^2$ = 1.8 × 10$^9$ A/m$^2$, in reasonable agreement with the theoretical value.

Now we briefly discuss the issue of filamentary conduction. The step structure and crossover features in $J_c$-$T$ plots suggest continuous breaking down of micro-domains in the sample. In $I$-$V$ characteristic measurements, on the other hand, we sometimes

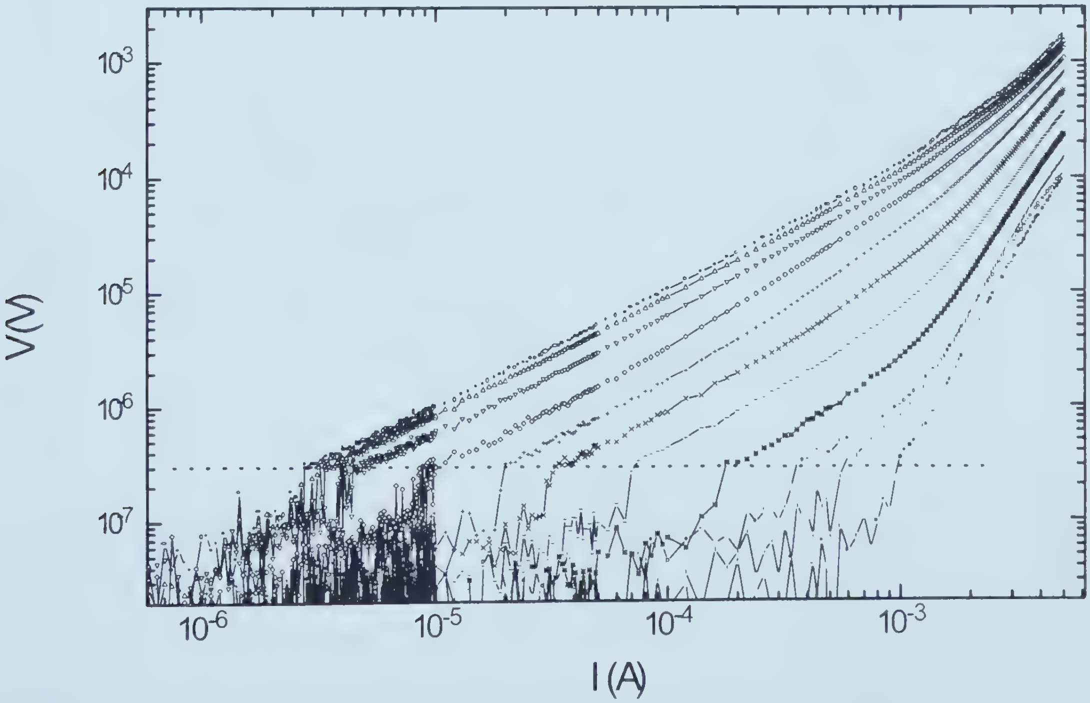

Fig. 7.11 $I$-$V$ characteristics of a Bi-2222 sample ($T_c \approx 109$ K). The dotted line marks the constant voltage jump at 0.3 μV. Temperature varied from 82 to 84 K in steps of 0.2 K.

observed voltage jumps at a constant level independent of temperature. A typical result is shown in Fig. 7.11, which was taken in the temperature interval 82 - 84 K in steps of 0.2 K. A constant voltage jump appeared at 0.3 μV independent of current and temperature. This translates into a nonlinear resistance which decreases at higher currents, e.g. from 0.1 Ω at $I$ = 3 μA to 0.3 mΩ for $I$ = 1 mA in a temperature interval of 2 K. A careful examination of the resistance data did reveal evidence of a mixed phase with lower $T_c$ ~ 81 K.

It is noticeable that the voltage jump happens at such low level (~ 0.3 μV) that a measurement with higher $I_c$ criterion (≥ 1 μV) could give false results of critical current. Such a $I_0$-$T$ plot is given in Fig. 7.12, in which $I_0$ is the current at the voltage jump. Around 83 K, the $I$-$V$ curves even has hysteresis for increasing and decreasing current. This shows that it is important to characterize the sample in $J_c$ measurements. Fig. 7.12 clearly reveals the two-phase structure in the sample.

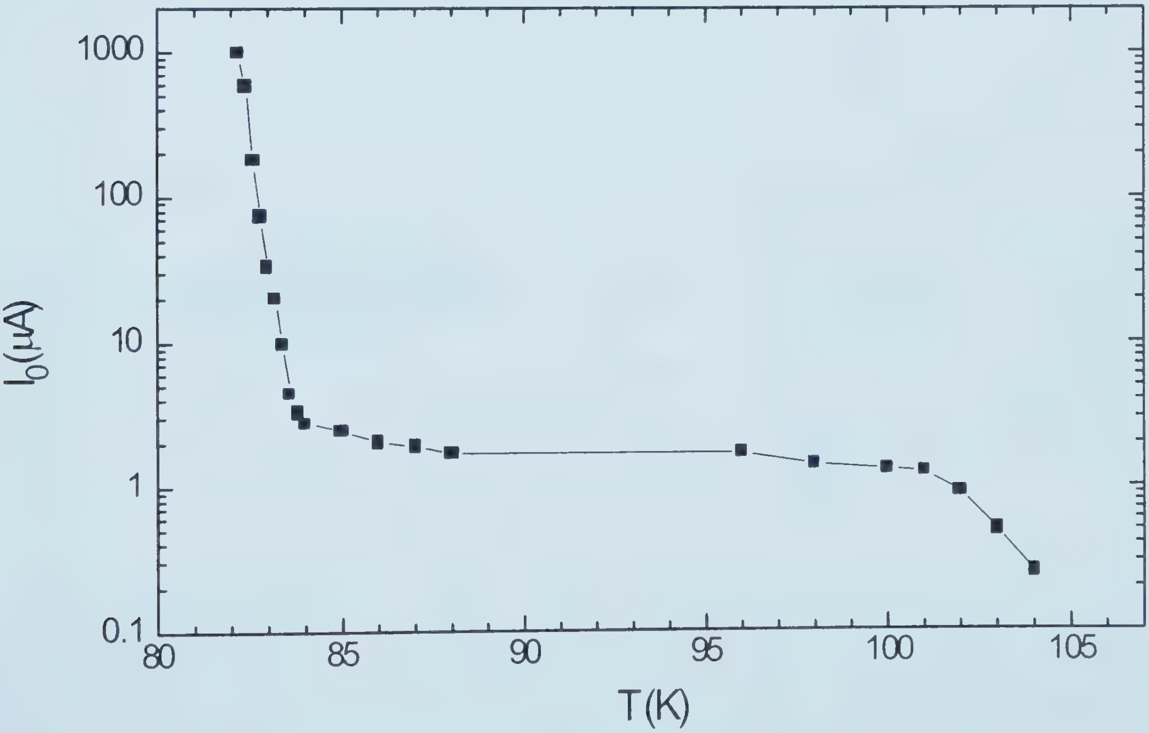

Fig. 7.12 Temperature dependence of the current at the voltage jump as demonstrated in Fig. 7.11 for a sample consisting of mixed phases.

## Chapter 8

# Anisotropy Factor and *c*-axis Transport

## 8.1 Anisotropy factor of BSCCO cuprates

The anisotropy factor is an important parameter characteristic of the layered structure of high-$T_c$ cuprates. It is defined as the anisotropic mass ratio [279]

$$\gamma \equiv \left(\frac{m_c}{m_{ab}}\right)^{1/2} = \frac{\lambda_c}{\lambda_{ab}} = \frac{\xi_{ab}}{\xi_c} = \frac{H_{c2//ab}}{H_{c2//c}} = \frac{H_{c1//c}}{H_{c1//ab}}, \tag{8.1}$$

where $H_{c2//c} = \Phi_0/2\pi\xi_{ab}^2$ and $H_{c2//ab} = \Phi_0/2\pi\xi_{ab}\xi_c$. $\Phi_0$ is the flux quanta. A schematic view of an anisotropic vortex is shown in Fig. 8.1.

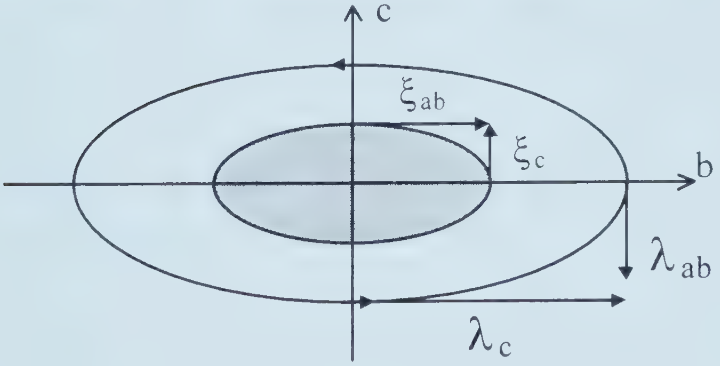

Fig. 8.1 A schematic view of a vortex along the *a*-axis. The normal-sate core size is characterized by $\xi_{ab}$ and $\xi_c$. For Bi-2212, the anisotropy factor $\gamma = \xi_{ab}/\xi_c = 183$, with $\xi_{ab}(0) \sim 2$ Å, and $\lambda_{ab}(0) \approx 2500$ Å.

The value of $\gamma$ differs for cuprates, even in the same series. For YBCO, $\gamma \sim 7$, whereas in the very anisotropic BSCCO it can reach about 150 to 200. Since the BSCCO whiskers have well-aligned crystalline axes along the surfaces, it is ideal to apply the field in these directions and evaluate the anisotropic properties.

Blatter *et al.* [280] developed a scaling approach that can map almost all results obtained from anisotropic superconductors to the isotropic ones. In resistance measurement with the applied field at an angle $\theta$ from the *c*-axis, we have:

$$\frac{R(\theta)}{R(0)} = \left[\cos^2\theta + \gamma^{-2}\sin^2\theta\right]^{-1/2}, \tag{8.2}$$

For $\theta = 90°$, this reduces to

$$\gamma = \frac{R_{H//ab}}{R_{H//c}}. \tag{8.3}$$

Resistance was measured on both Bi-2212 and Bi-2223 whiskers with the field applied successively along the *a*, *b* and *c*-axes, while the current flowed in the *a*-axis in all the cases. Figs. 8.2A and B show the typical data for *H//b* and *c*. As is expected, the broadening of superconducting transition for the two configurations of field is vastly different. The Lorentz-force-free orientation, in which *H//I //a*, yielded even smaller broadening. In all the measurements, the resistance curves for certain field values in different orientations show good overlap with each other, verifying the scaling behavior. The anisotropy factor can thus be calculated according to Eq. (8.3). For the cases in Figs. 8.2A and B, this gives:

$\gamma$ = 40000 G /110 G = 363 for Bi-2223;

$\gamma$ =55000 G /300 G = 183 for Bi-2212.

Other choices of field values also resulted in approximately the same $\gamma$. The result correctly reflects the fact that Bi-2223 is more anisotropic than Bi-2212. The deviation from the *T*-independent scaling below some characteristic temperature is an indication of 3D to 2D crossover as *T* decreases.

In the literature, the value of $\gamma$ scatters over a wide range. We list some typical values here for Bi-2212 from various techniques such as transport, magnetic torque, and

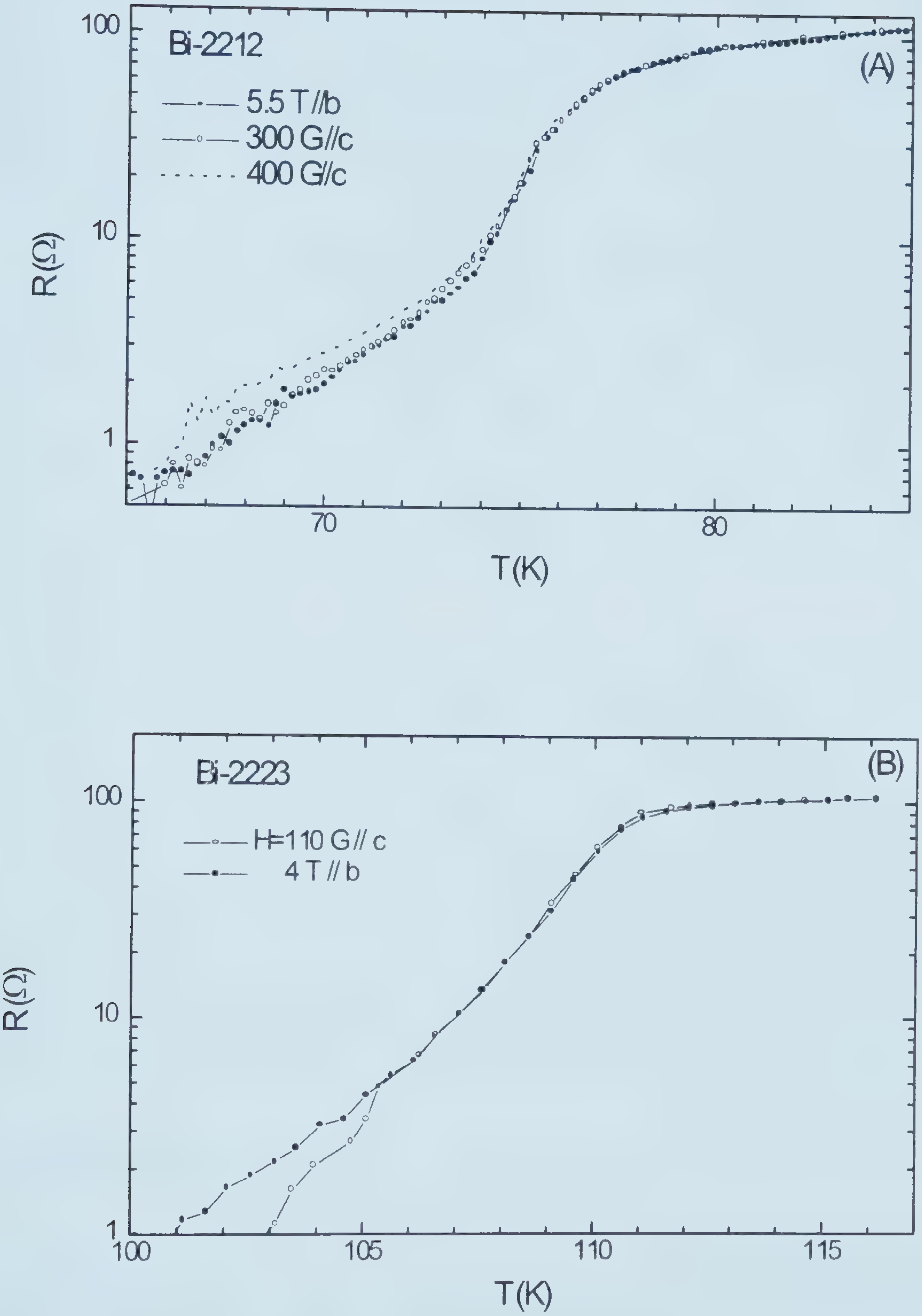

Fig. 8.2 Overlapping of *R-T* curves for different field orientations: H// *c* and H// *b* axes. The anisotropy factor is evaluated from such field values, $\gamma = H_{//b} / H_{//c}$. (A): Bi-2212, and (B) Bi-2223. For clarity, only the closest curves were shown among many others.

μSR.: $\gamma \approx 50$ [281-283], 150 [284, 285], and 243 in optimally doped samples [286]: This seems incompatible to the data from Ref. 283, which reported $\gamma = 50$ for oxygen-annealed samples and $\gamma = 280$ for Ar-annealed samples. Our present result, $\gamma = 183$, agrees well with those from μSR [287], transport [288], and magnetic torque [284] measurements.

For Bi-2223: $\gamma = 31$ [289], and 200 [290]. The apparent discrepancy in the values of $\gamma$ comes from such crucial factors as material (bulk or thin film), oxygen content, and analysis schemes. The evaluation of $\gamma$ is largely based on the continuum Ginzburg-Landau approximation, which may not be fully applicable for highly anisotropic systems. The oxygen content also plays a role. In $YBa_2Cu_3O_{7-\delta}$, for example, Rapp *et al.* [291] reported $\gamma = 5$ for fully oxygenated samples. $\gamma$ increases from 20 to 80 as $\delta$ increases from 0.1 to 0.5.

Since the mixed-state transport is dominated by flux dynamics, and hence is determined by the pinning in the materials, the vastly scattered values of $\gamma$ reflect this behavior. It is difficult to compare $\gamma$ from samples prepared by different methods, or measured with different techniques, unless the material quality is comparable.

The value of $\gamma$ can also be determined from the crossover field, $B_{cr} = 4\Phi_0/\gamma^2 s^2$ [Refs. 291, 292], where $s$ is the interlayer distance. The crossover is also reflected in the field dependence of activation energy of the thermally assisted flux flow. From experiment, we estimate $B_{cr} \approx 2000$ G, and $s = 15$ Å, which gives $\gamma = 132$ for Bi-2212.

## 8.2 *c*-axis transport

Study of *c*-axis conduction is important in that it can reveal interlayer correlation strength. It had been generally demonstrated that resistivity along this axis follows a semiconducting behavior above $T_c$, and the anisotropic resistivity ratio, $\rho_c / \rho_{ab}$, can reach $10^4$-$10^5$ in Bi-2212. Unfortunately for BSCCO whiskers, it is extremely difficult to fabricate electrodes on both *ab* surfaces to measure $\rho_c$. However, in a rare case of whisker sample, when we made the electrical leads intended for $\rho_{ab}$ measurement as usual, the data turned out to be mixed with $\rho_c$, as shown in Fig. 8.3. Since the

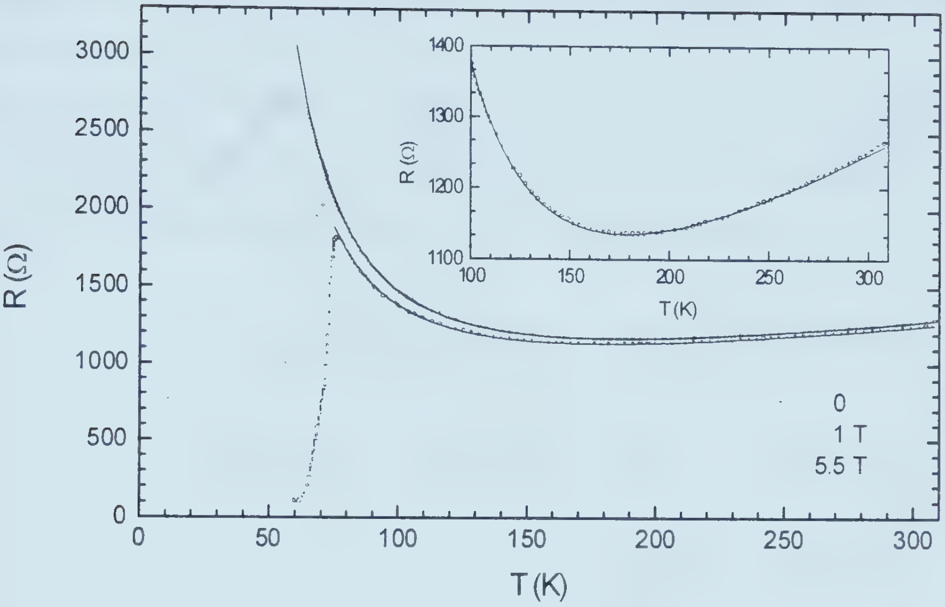

Fig. 8.3. Resistance of a whisker containing $c$-axis transport in different fields. Solid lines are fittings to the relation: $R_c = \frac{A}{T}\exp(\frac{\Delta}{T}) + BT + C$. Inset: magnified view of the high temperature part.

measurement configuration was for $\rho_{ab}$, and because $\rho_c$ is much higher than $\rho_{ab}$, the data shows a small mixture of $\rho_c$ with $\rho_{ab}$. This could have been caused by misoriented domains or twin boundary in the current path. The former and its semiconducting behavior were observed in misoriented Bi-2212 films [293]. The influence of twin boundary will be discussed later.

The $\rho - T$ curve has a broad minimum around $T_{\min} \approx 180$ K. It reaches maximum at the superconducting onset at $T_c \sim 76$ K, which is the usual value observed in most as-grown BSCCO whiskers. Applying magnetic fields (1 and 5.5 Tesla) has the effect that $\rho$ is extrapolated from the normal-state trend line down to lower temperature (Fig. 8.3). The field was set to be parallel to the $b$-axis and current flowed in the $a$-axis (the axes are as in the nominal case for BSCCO whiskers). All these features are closely similar to the $c$-axis resistivity data reported by two other groups [70, 294]. The slight shift of the 1 and 5.5 Tesla curves relative to the zero-field curve might be an artifact due to electrical contact. The fact that a mere 5.5 T field can easily suppress superconducting

transition means that the mixture from the *c*-axis conduction must be a small percentage. It was a great loss that this peculiar sample was destroyed in a subsequent oxygen annealing.

Many theoretical models had been proposed for the *c*-axis resistivity [295] Experimentally for YBCO and Bi-2212, Yan *et al.* [294] found $\rho_c$ fits to a combined relation consisting of an activation term and a linear-$T$ contribution:

$$\rho_c(T) = \frac{A}{T}\exp(\frac{\Delta}{T}) + BT + C. \tag{8.4}$$

Table 9.1 Fitting parameters $A$, $B$, $C$ and $\Delta$ in $\rho_c / \rho(300K) = (A/T)\exp(\Delta/T) + BT + C$, for $H$=0, 1 and 5.5 T.

| | $H=0$ | 1 T | 5.5 $T$ |
|---|---|---|---|
| $A$ | 15.16 | 16.06 | 19.30 |
| $B$ ($10^{-3}$) | 1.456 | 1.456 | 1.56 |
| $C$ ($10^{-3}$) | 489.6 | 483.9 | 438.89 |
| $\Delta$ (K) | 112.8 | 117.6 | 105.9 |
| $R$(300K) | 1248.34 | 1275.6 | 1281.0 |

A modified formula without the $BT$ term was proposed by Watanabe *et al.* [98]. We tried to fit our data to both versions and found that it agrees well with Eq. (8.4). The calculated $R_c(T)$ data are as shown by the solid lines in Fig. 8.3, with the parameters listed in the Table 9.1.

The fitting parameters are comparable with those in Refs. 98 and 294. Especially the activation energy $\Delta \sim 110$ K agrees well with the reported data. The fact that the present resistivity is well fitted to the combined contribution model agrees with the actual measurement that contains both $\rho_{ab}$ and $\rho_c$. It is noticeable that the results in Ref. 98 fit to the pure activation-type $\rho_c$ whereas data from Yan *et al.* [294] and the present work contain an extra linear-$T$ term. Our data shows that such linear-$T$ term could well come from the in-plane transport. This point is further supported by the very weak field

dependence of $B$ and $C$, which is the same situation for $\rho_{ab}$. This may resolve the $B = 0$ case in which the sample quality is presumably better. In addition, a trend of increasing $A$ and $\Delta$ with field was observed.

It was suggested that the semiconducting $\rho_c$ is related to the opening of a spin gap. We believe such a correlation is highly *unlikely* because: (1) $\Delta$ is much smaller than the spin gap obtained by various methods ($2\Delta_0 \sim 50$ meV); and (2) the so-called spin-gap related semiconducting onset near 200 – 300 K is a pure coincidence due to the combined transport of $\rho_c$ and $\rho_{ab}$, and thus is largely material-dependent.

## 8.3 Influence of twin boundary conduction

It must be stressed that an insulating $\rho$-$T$ relation can be mimicked by twin-boundary conduction. This may be related to the behavior of $\rho_c$ in poor quality samples. In another rare case of whisker growth (only one was found up to now), one

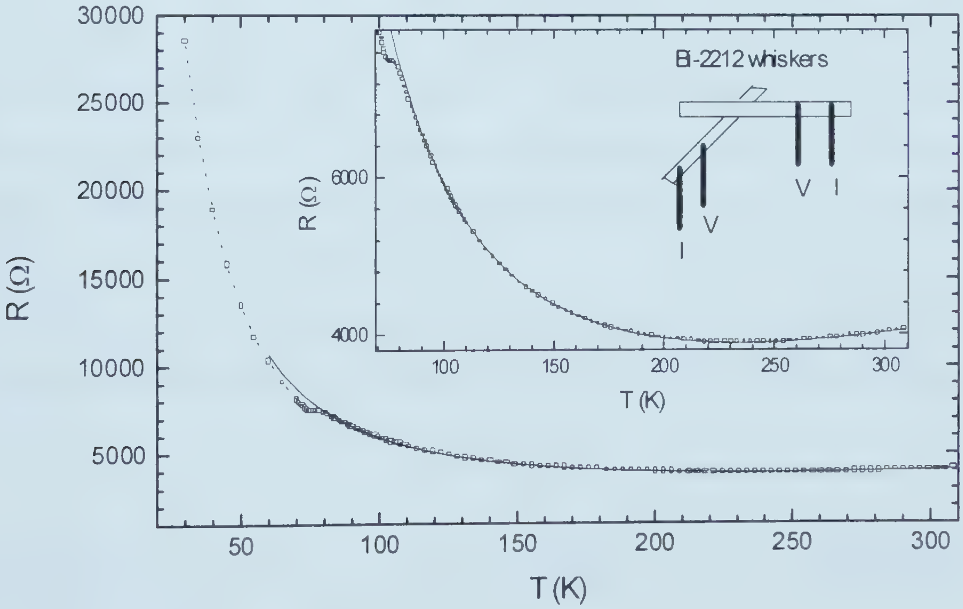

Fig. 8.4 Resistance of a sample consisting of two BSCCO whiskers and a stack-junction formed by them during crystal growth. A dip appears at $T_c$ when the two whiskers become superconducting. Inset: high-temperature portion of the $R$-$T$ curve. Also shown are the sample and the four electrodes.

whisker stacked on top of another whisker to form a junction along the $c$-axis, as shown in the inset of Fig. 8.4. Electrical leads were sputtered onto the legs of this "λ" junction for resistance measurement. The result is plotted in the main panel of Fig. 8.4. This is a clear example of composed resistance with both in-plane and crystal boundary contributions. The latter is semiconducting while the in-plane resistance is nearly linear in $T$. As a result, the $R$-$T$ curve has a minimum around $T \sim 235$ K. It also shows a dip at $T_c \sim 76$ K when the whiskers become superconducting. Again, the *whole* curve above $T_c$ can well be fitted to Eq. (8.4), as shown by the solid line in Fig. 8.4. This may offer an alternative explanation of the result in Fig. 8.3: it is caused by a twin boundary and tunneling rather than by $c$-axis contribution. In the present case, tunneling did not happen below $T_c$ due to the thick junction as indicated by the much higher resistance.

This result prompts questions about the true temperature dependence of $\rho_c$: the semiconducting behavior could be caused by defects, as demonstrated in the present results. Lavrov *et al.* [173] indicated that stacking faults could block $c$-axis conduction and give rise to an insulating $\rho_c$, whereas the screw dislocations may short-circuit the $CuO_2$ planes and result in metallic out-of-plane conduction. The combined effect is a crossover in $\rho_c$. Indeed, interlayer disorders commonly exist in most cuprates in the forms of dislocations, oxygen vacancies, or substituted cations, which could effectively block $c$-axis transport. In $YBa_2Cu_4O_8$ [296] and $RBa_2Cu_3O_6$ ($R$ = Tm, Lu) [173], it had been showed that the insulating $\rho_c$ is not a general feature of cuprates. In both materials, interlayer defects were largely reduced.

It would thus be highly interesting to check the situation of BSCO whiskers, because the specific growth mechanism results in no screw dislocation and stack faults. To over-

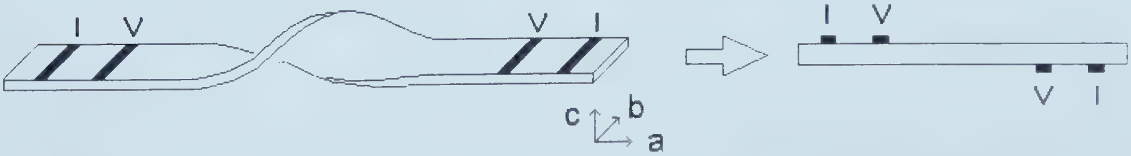

Fig. 8.5 A 180° twisted Bi-2212 whisker. The offset leads were sputtered onto the top and bottom surfaces (*ab* planes), as shown by the equivalent view on the right.

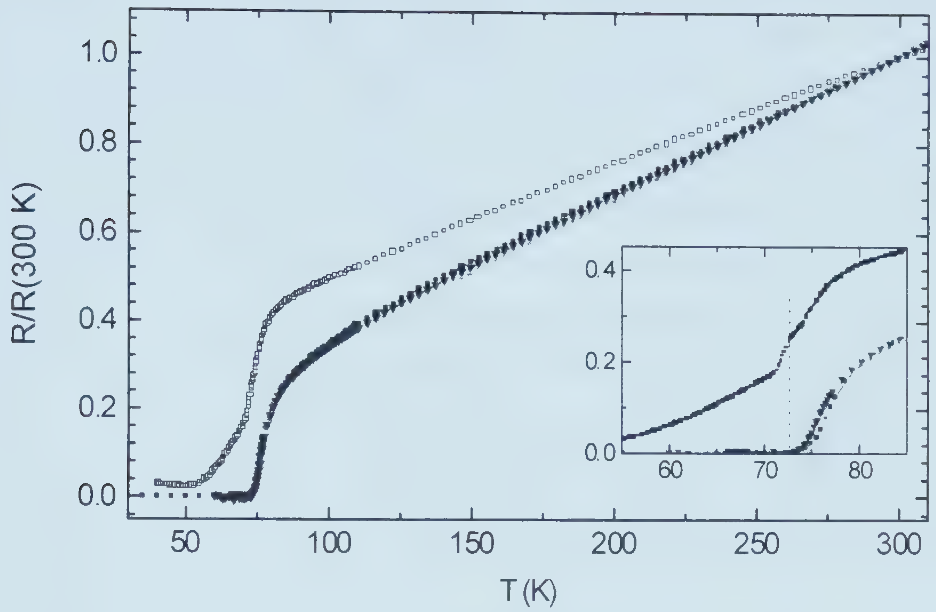

Fig. 8.6 Resistance of the twisted whisker (squares). Also shown for comparison are the in-plane data of four other samples from the same batch of crystals. Inset: details near $T_c$.

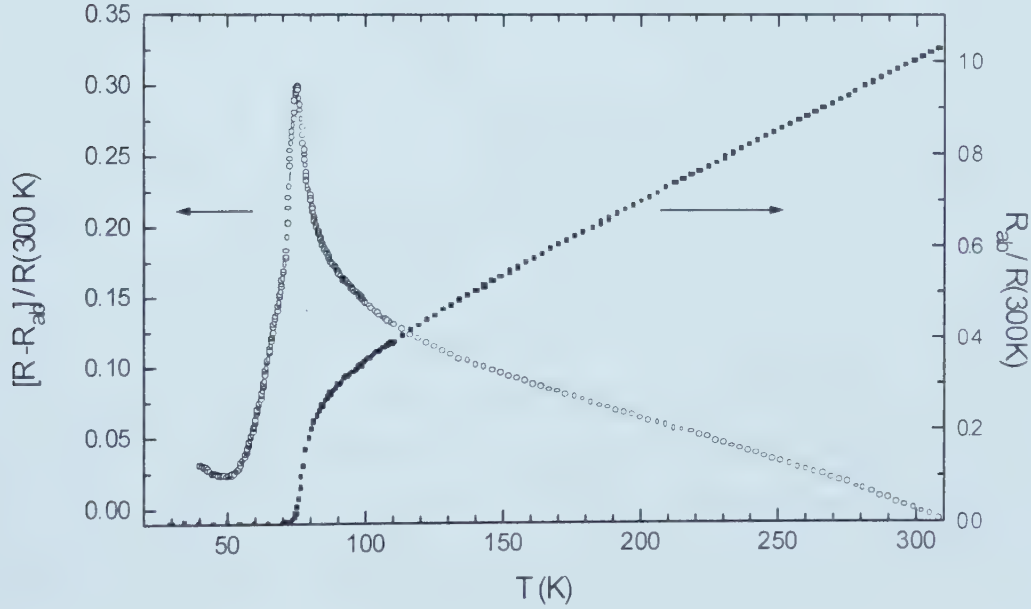

Fig. 8.7 ($R$-$R_{ab}$) of the twisted whisker, showing the semiconducting $c$-axis contribution. $R_{ab}$ is from a typical Bi-2212 whisker in Fig. 8.6.

come the difficulty in making aligned electrodes on top/bottom surfaces, we managed to twist one end of a long Bi-2212 whisker (~ 5 mm) by 180°, and sputtered a pair of current/voltage leads on the top and bottom surfaces. A schematic view of the leads is shown in Fig. 8.5. The resistance from such a configuration would contain the out-of-plane part. The result is presented in Fig. 8.6. To compare with the ordinary *ab*-plane measurement, we also plotted the in-plane resistance data of four other samples from the same batch. The effect of the twisting configuration is very clear, which really shows the *c*-axis contribution. The feature at the foot, where *R-T* bent as detailed in the inset of Fig. 8.6, may be linked to the disappearance of in-plane resistance. To extract the out-of-plane contribution, we tentatively subtracted one typical $R_{ab}$ curve from that of the twisted whisker, the result ($R$-$R_{ab}$), as plotted in Fig. 8.7, instantly showed the semiconducting behavior!

One distinct feature of ($R$-$R_{ab}$) is the monotonically decreasing value with increasing temperature in contrast to that of our two-whisker junction, Fig. 8.7. These results demonstrate that the minimum in $\rho_c$ is caused by two competing transport processes, one is activation-type associated with the *c*-axis and the other is linear in $T$ and may have originated from in-plane conduction.

In conclusion, *c*-axis transport mechanism was studied with clearly controlled sample configurations. Generally, $\rho_c$ was found to be activation-type, with or without an extra linear-$T$ term. This term seems to be of in-plane origin, which disappears for good quality samples, as found in the studies of Watanabe *et al.* [98] and the present work. Up to now, non-activating $\rho_c$ was only observed in $YBa_2Cu_4O_8$ and $RBa_2Cu_3O_{6-x}$, further studies on other high quality cuprates will shed light on this discrepancy. Finally, an activation-like conduction can be mimicked by a twin boundary (or other blocking mechanisms) in the current path. This should be carefully distinguished from that of intrinsic out-of-plane resistivity.

## Chapter 9

# Dissipation in the Vortex Core[†]

Free flux flow in the mixed state of superconductors describes the motion of vortices under the influence of the Lorentz force and an effective viscosity. The vortices move perpendicular to the applied current, and thus induce an EMF in the current direction. This leads to a sizable magneto-resistance, and a very small Hall effect [297]. The classical Bardeen-Stephen (BS) theory [255] describes this in terms of the normal state resistivity and normal electrons in the vortex core. Caroli, de Gennes, and Matricon [298] realized that quantized states with an energy gap $\omega_0$ exist in the vortex core. In the case of large impurity scattering these states are smeared and the BS theory gives the correct description of free vortex flow. In the "superclean" case as measured by $\omega_0\tau \gg 1$, where $\tau$ is the normal state relaxation time, the core levels are distinct. In this case the vortex motion in a field becomes parallel to the external current. This leads to an increasing Hall effect, and a diminishing flux flow resistivity for conventional (*s*-wave) superconductors. In the case of *d*-wave superconductors, it was proposed by Kopnin and Volovik [299] that the flux flow resistivity assumes at low temperature a universal value independent of the normal state relaxation time. Nodes in the superconducting gap of a *d*-wave superconductor lead to node structure of the vortex gap, resulting in resonance absorption of zero frequency vortex modes. An approach to a Hall angle of $\pi/2$ has been observed [300] in a 60 K YBCO single crystal. In this work we report the possible observation of the resistivity limit in very clean single crystal whiskers of Bi-2212 high-$T_c$ superconductors.

In order to observe free flux flow, one must have samples with very low concentration of pinning centers. In high-$T_c$ superconductors, this condition is difficult to obtain due to the microscopic layered structure, the small coherence length and the different order parameter. Because of this, free flux flow has been observed only in narrow ranges of field and temperature [269] or for pulsed large current density [301].

---

[†] Weimin Chen, J. P. Franck, and J. Jung, http://xxx.lanl.gov/cond-mat/9909072

In general, thermally activated flux flow (TAFF) is observed [254], followed by formation of a vortex solid at low temperatures [302]. For the observation of flux flow in very clean samples of high-$T_c$ superconductors, we have studied a number of Bi-2212 whiskers. These whiskers can be grown from 2212 ceramic pellets. They are generally very pure and in good specimens show free flux flow in the magneto-resistance down to the lowest flux flow resistances measurable. Below we describe the properties of two such whiskers, both showing free flux flow, but with different field dependencies. The differences in magnetoresistance can be correlated with the moderately clean and superclean regime reached. In the superclean regime we observed at low temperatures the universal flux flow resistivity, independent of carrier relaxation [299].

The whiskers were grown by long time annealing at temperatures between 835 and 855°C from ceramic (and non-stoichiometric) pellets of BiSrCaCu oxide as described previously. The whiskers have the shape of long blades, typically 1 - 2 mm long, 10 μm wide, and 0.5 μm thick. The crystallographic orientation is: the *a*-axis along the long direction, *b*-axis parallel to the width, and *c*-axis perpendicular to the blade. The first whisker (Whisker 1) described here was grown at atmospheric pressure (20% $O_2$), and can be assumed to be overdoped. The resistive $T_c$ is 74.6 K. The second whisker (Whisker 2) was also initially grown at atmospheric pressure, but following this was annealed in flowing nitrogen at nominal 500°C for 4 hours. This whisker is underdoped with a resistive $T_c$ of 73.2 K, a pseudogap near 220 K was observed in the normal state resistivity in support of this assessment. Its surface morphology is as shown in Fig. 2.2

Resistance measurements were done by standard four-probe method. We used true DC current rather than AC modulation in order to minimize disturbance of the flux flow. Each measurement was done by driving the current in both directions a few times and averaging the voltages so as to reduce thermal noise. The current is always along the *a*-axis and fixed at 0.5 μA (current density ~ 10 A/cm$^2$), whereas the magnetic field was applied along all the three axes and changed between 0 and 5.5 T.

The geometry of the whiskers and the attached leads were observed in a SEM, the dimensions are as follows (length measured between potential leads). Whisker 1: length 0.654 mm, width 4.9 μm, thickness 0.48 μm; Whisker 2: length 0.28 mm, width

4.38 μm, thickness 0.20 μm. One notices that the thickness is of the order, or smaller than the penetration depth (2600 to 3000 Å in Bi-2212). Because of this, and the large demagnetization effect in the $H // c$ configuration, we assume that the applied field $H$ equals the magnetic induction $B$ in the whiskers.

In Figures 9.1 and 9.2 we show the resistivity for both whiskers in different fields up to 5.5 T. Whisker 2 was only measured in fields of 3, 4, and 5.5 T, Whisker 1 was also measured at lower fields. We see below the extensive fluctuation range near $T_c$ an extended region where $\rho(T, B)$ is linear in $T$. This extends to very low values of $\rho(T, B)$. No sign of TAFF, or of flux line melting was observed in either whisker. Flux line melting occurs only at fields of 400 G or below and for $T$ larger than 40 K [302, 303], so it is not surprising that we did not observe it. We interpret this regime as the free flux flow regime, and the characteristics of the $\rho(T, B)$ for both whiskers in this regime show certain similarities, as well as differences.

The free flux flow regime starts at a given low temperature for given field. We call this field $B^*(T)$. Below $B^*(T)$, the resistance is zero due to immobilization of the vortices. The temperature dependence of $B^*$ could be fitted to:

$$B^* = B_o{}^*\left(1-\frac{T}{T_c}\right)^n \tag{9.1}$$

For Whisker 1 we find $n = 3.33 \pm 0.05$ and $B_0^* = 24.45$ T. For Whisker 2 we also fitted $B^*$ to Eq. (9.1) with $n = 3.33$, although the exponent is less certain here due to the few fields used ($n = 3.33 \pm 0.3$). We found then $B_0^* = 6.71$ T. At all fields we are well above the vortex melting line. The fields $B^*(T)$ are close to the depinning line, this line depends on the amount of disorder in the samples [303]. In spite of the very similar zero field transition temperature, we see that the two whiskers exhibit different properties. In particular, Whisker 2 shows magneto-resistance down to very low temperatures, close to 0 K. If the fit of Eq. (9.1) can be extrapolated, one would expect non-zero flux flow resistance at 0 K in this whisker at 6.7 T. Extension of the free flux flow regime to such low temperatures has not previously been observed.

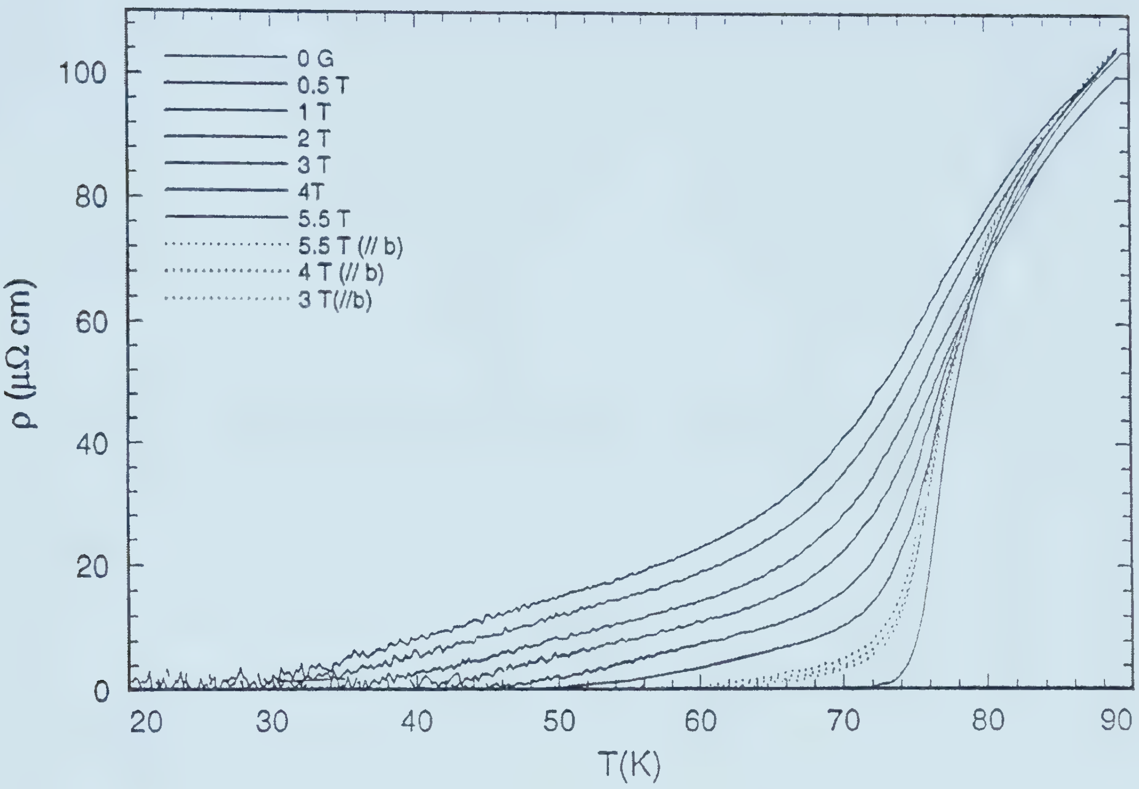

Fig. 9.1 The resistivity of Whisker 1 in fields between 0 and 5.5 T. Solid curves, *H*//c; And dotted curves, *H* // b.

A second difference between the two whiskers is the field dependence of the magneto-resistivity. For Whisker 1 we find that $\rho_f/\rho_n$ is linear in field above about 1.5 T and in the range 40 to 60 K. At lower fields we find curvature due to the transition from 3D to 2D at higher fields. We use then the Bardeen-Stephen relation [255] in its differential form in the high field regime:

$$\frac{d\rho_f/\rho_n}{dB} = \frac{1}{Bc_2}, \tag{9.2}$$

This corresponds to the field region where we have pancake vortices with small interplane interaction. We obtain reasonable values for $B_{c2}$ in this region of $T$ and $H$. For fields above about 1.5 T, we obtained $B_{c2}$ both for $H//c$ and $H//b$, in the range 40 to 60K ($H//c$), and 65 to 70 K ($H//b$). The fields extrapolate to $T_c$, with slopes of -1.33

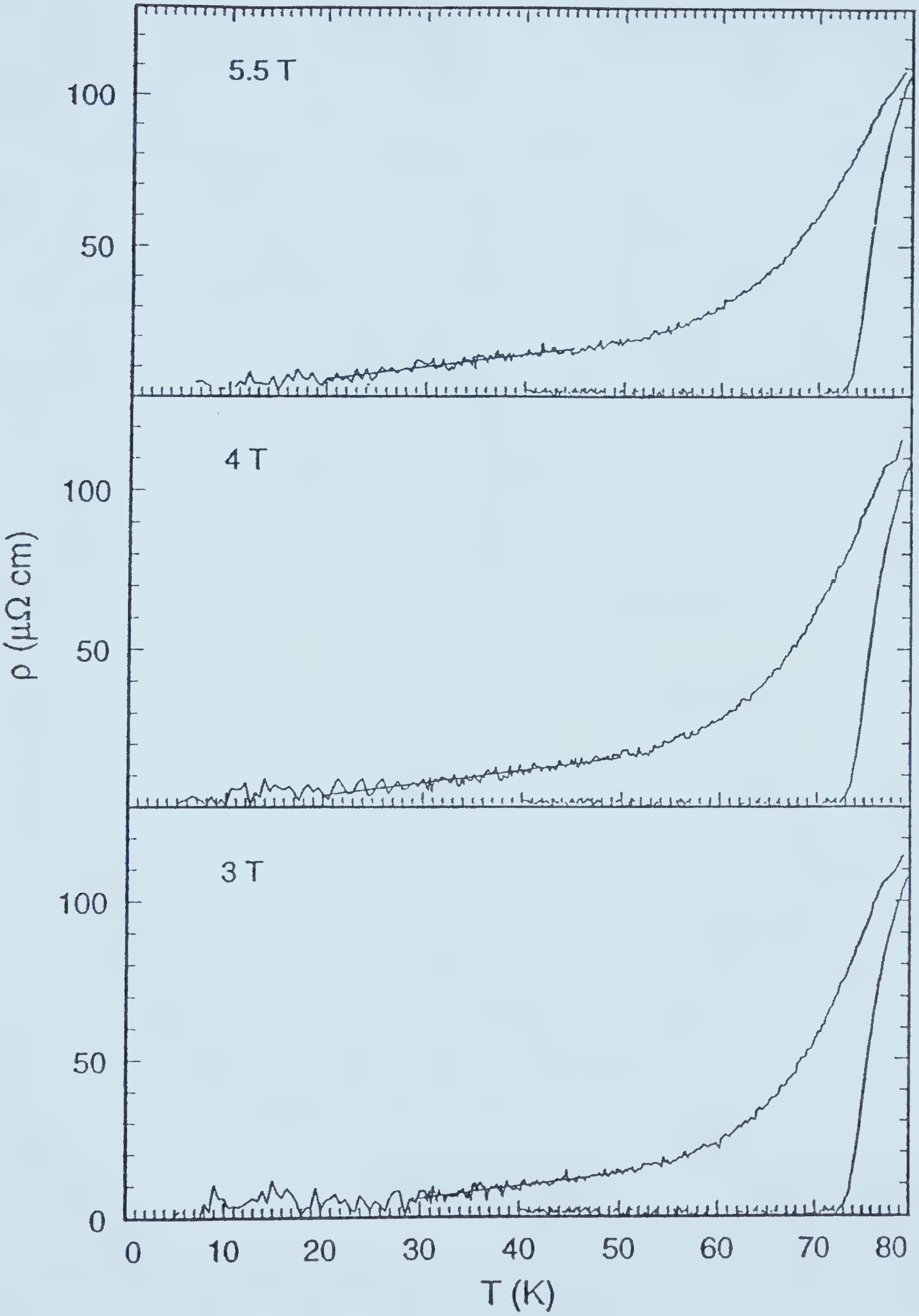

Fig. 9.2 The resistivity in 3, 4 and 5.5 T of Whisker 2. Fits to the linear in $T$ regime are shown.

T/K (*H//c*), and -30.8 T/K (*H//b*). This is shown in Fig. 9.3. These data are in good agreement with literature values both for the temperature dependence, and the anisotropy [304].

In the case of Whisker 2 no such analysis is possible. We show in Fig. 9.4 both $\rho_f$, and $\rho_f/\rho_n$ as function of field for this whisker. As can be seen, $\rho_f/\rho_n$ and $\rho_n$ at high temperatures are only weakly dependent on field above 3 T. For lower temperatures, the dependence of the flux flow resistivity $\rho_f$ on field increases, and assumes below approximately 30 K a uniform, temperature independent slope of $d\rho_f/dB = 1.40$ μΩcm/T. Attempts to fit to the Bardeen-Stephen expression Eq. (9.2) would lead to unacceptable fields $B_{c2}$, with the wrong temperature dependence.

The characteristic behavior of $\rho_f$ in Whisker 2 is the near-linearity of $\rho_f$ for fields above 3 T. Below 3 T we have extrapolated $\rho_f$ at each temperature to $B^*$ calculated

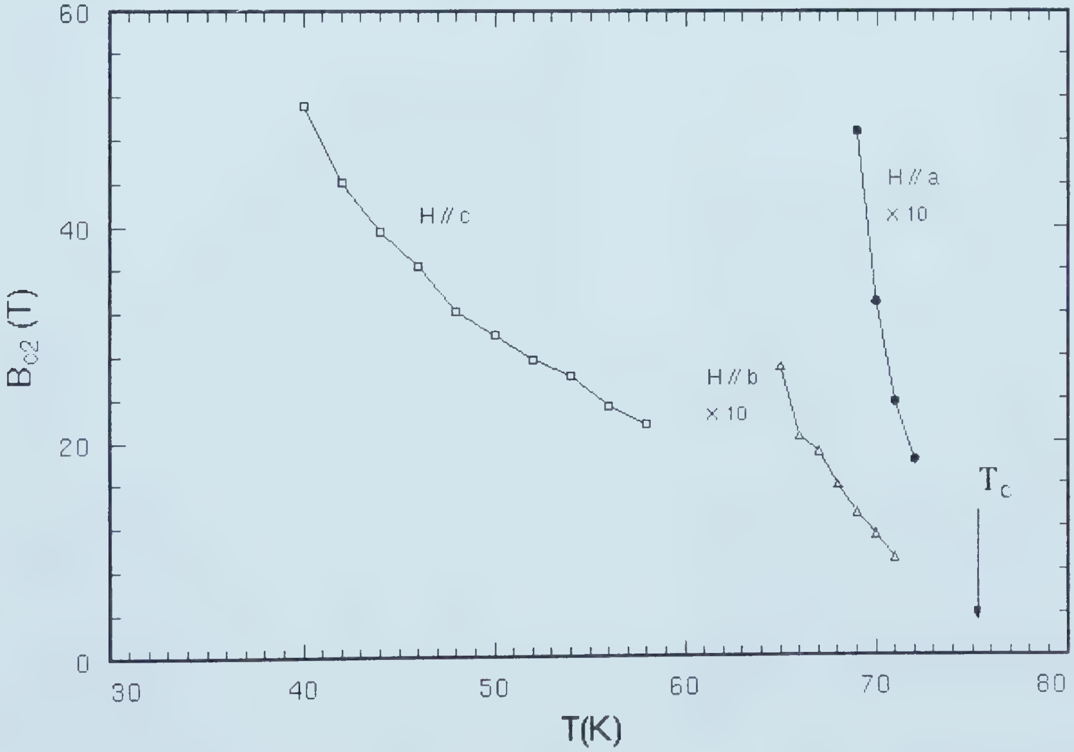

Fig. 9.3 Estimates of $B_{c2}$ for Whisker 1 obtained from the Bardeen-Stephen Theory, Eq. (9.2).

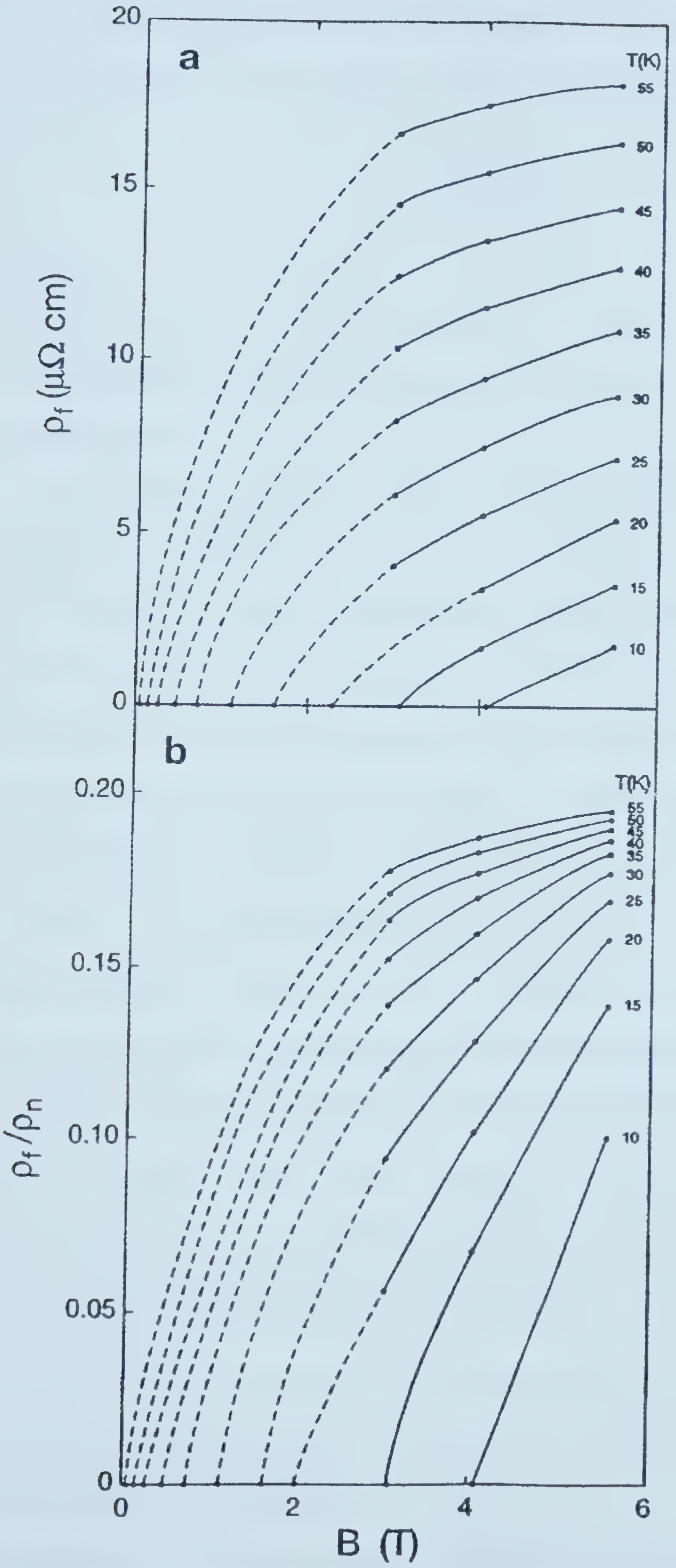

Fig. 9.4 The resistivity in the free flux region of Whisker 2. (a) Resistivity $\rho_f$ and (b) Reduced resistivity $\rho_f/\rho_n$, where $\rho_n$ is the extrapolated normal state resistivity. The dotted lines are rough extrapolations to the onset field from Eq. (9.1).

from Eq. (9.1). This involves curvature which probably again is connected to the 3D to 2D crossover at high fields. At temperatures below about 30 K, $\rho_f(B)$ has the same slope, and for $T = 15$ K and below this extends to $B^*$. In this regime we have, therefore:

$$\rho_f(T) = \rho_o(B - B^*) \tag{9.3}$$

where the constant is given by $\rho_o = 1.40 \pm 0.1$ μΩcm/T. Above about 30 K, the slope decreases, and at 55 K reaches 0.58 μΩcm/T, or one third of the low temperature limiting value.

The different magneto-resistive properties of the two whiskers are related to the microscopic properties of the whiskers. We first discuss the normal state properties. For Whisker 1, we find a linear temperature dependence of $\rho_n$ (in zero field) until the fluctuation regime near $T_c$ is reached. We base our analysis on an extrapolation of this linear part to the lowest temperatures. The axis intercept at 0 K is about 23.0 μΩcm, or about 6.4% of the resistivity at 300 K. The two-dimensional square resistance $R$ per $CuO_2$ layer was obtained from $R = \rho_n/d$, $d = 15$ Å. R varies between 2390 Ω at 300 K to 190 Ω at 5 K. From this we obtained the product $k_F l = h/e^2R$, where $k_F$ = radius of Fermi surface, $l$ = mean free path. $k_F l$ obtained in this way varies between 10.8 at 300 K and 135 at 5 K. At low temperatures the Whisker 1 is, therefore, in the moderately clean regime. One can estimate $l$ from this by using a reasonable value for $k_F$ (~ 0.33 Å$^{-1}$). $l$ reaches then a value of 330 Å at 5 K. For Whisker 2, we also extrapolate the linear part of $\rho_n$, the axis intercept at 0 K is close to zero, (± 5 μΩcm). R in this case varies from 3400 Ω at 300 K, to 56.7 Ω at 5 K. $k_F l = (h/e^2)/R$ varies from 7.6 at 300 K to 456 at 5 K. This leads to an estimate for $l$ ($k_F = 0.33$ Å$^{-1}$) of 1110 Å at 5 K. Whisker 2 enters, therefore, further into the clean, or the superclean regime at low temperatures, but this occurs only below 30 K. It is, however, important to notice that in fields of 5.5 T we can explore further into the superclean regime with Whisker 2.

A more drastic difference between the two whiskers is evident in the minigap $\omega_0$ related to the states within the vortex core [299, 305]. The minigap is given by:

$$\omega_o = \frac{\Delta_o{}^2}{\varepsilon_F} \tag{9.4}$$

where $\Delta_o$ is the (maximum) superconducting gap at 0 K, and $\varepsilon_F$ the Fermi energy. We use $\varepsilon_F$ = 500 meV for both whiskers [123]. The value of $\Delta_o$ is, however, drastically different. For Whisker 1 (overdoped) we estimate $\Delta_o$ = 10 meV, and for Whisker 2 (underdoped) $\Delta_o$ = 25 meV [306]. The minigaps are then 0.20 meV for Whisker 1, and 1.25 meV for Whisker 2. The region of superclean behavior is governed by the size of the product $\Gamma=\omega_0\tau$, where $\tau$ is the normal state relaxation time. The approximately six-fold increase of $\omega_0$ for Whisker 2 over that of Whisker 1 is remarkable. We can further estimate $\tau$ from

$$\tau = \frac{4\pi}{c^2}\frac{\lambda_o{}^2}{\rho_n} \tag{9.5}$$

where $\lambda_o$ is the penetration depth at 0 K. We use $\lambda_o$ = 2600 Å for Whisker 1 [306], and a slightly larger $\lambda_o \approx$ 3000 Å for Whisker 2 [307]. For Whisker 1, the relaxation time obtained from Eq. (9.5) reaches 0.37 psec at the lowest temperatures, and $\Gamma=\omega_0\tau$ goes to 0.1. For Whisker 2, on the other hand, we find that $\tau = 6.64/T$ (psec), $T$ in K, so that $\tau$ reaches very large values at low temperatures, $\tau$ at 5 K is 2.54 psec. It appears, therefore, that in this whisker, the superclean region is reached at low temperatures. All estimates are based on the extrapolated normal state resistivity, without adjustment for a possible reduction of $\rho_n$ in the vortex cores. The parameter $\Gamma$ is, therefore, at low temperatures considerably larger for Whisker 2, than for Whisker 1. This is due to the combination of a larger $\omega_o$ and a smaller $\rho_n$ for Whisker 2. Estimates of $\Gamma$ and $k_F l$ are shown in Fig. 9.5.

In the moderately clean regime, the free flux flow ohmic resistivity is given by Kopnin and Volovik [299] as:

$$\rho_f = \frac{B}{n_h ec\Gamma \ln\left(T_c / T\right)} \tag{9.6}$$

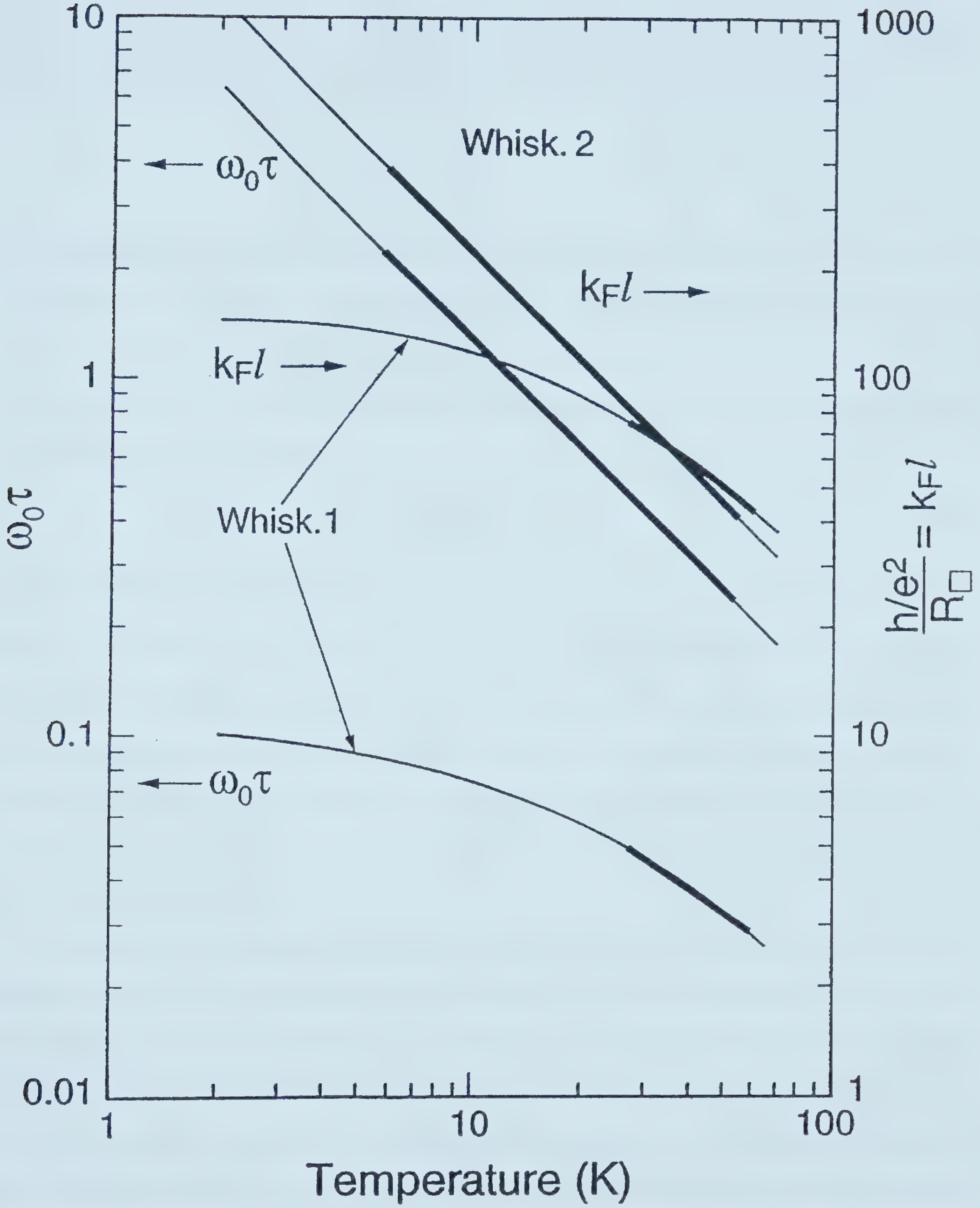

Fig. 9.5 Estimates of $k_F l$ and $\Gamma = \omega_0 \tau$ for Whisker 1 and Whisker 2. The regimes over which we observed free flux flow are shown heavy.

In the superclean regime the free flux flow resistivity assumes a universal, non-zero, limit, independent of the relaxation time, and, therefore, the normal state resistivity:

$$\rho_f = \frac{\pi}{2}\frac{B}{n_h ec} \tag{9.7}$$

The temperature at which the moderately clean value of $\rho_f$ equals the low temperature ideal limit was estimated by using the estimated value of $\Gamma$ for Whisker 2, it is found to be $T = 23$ K. This is in good agreement with our observations.

Since in Whisker 2 at low temperatures the free flux flow sets in at $B^*$ and is linear in $B$, we use Eq. (9.7) in the form

$$\rho_f = \frac{\pi}{2}\frac{B - B^*}{n_h ec} \tag{9.8}$$

The only system parameter in here is $n_h$, which we estimate from the 0 K penetration depth $\lambda_0 = 3000$ Å as $n_h = 0.63 \times 10^{21}$ cm$^{-3}$. We would then expect from Eq. (9.5) a limiting free flux flow resistivity of 1.56 ($B$-$B^*$) μΩcm. This compares extremely well with the observed value of 1.4 ($B$-$B^*$) μΩcm. The observed limiting behavior represents, therefore, most likely the predicted universal behavior. This result is connected to the gap nodes in a *d*-wave superconductor, which results in higher order nodes in the minigap [300].

There have been several observations of free flux flow in moderately clean, or superclean high-$T_c$ superconductors by Matsuda *et al.* [308], Harris *et al.* [300], and Doettinger *et al.* [309]. Harris *et al.* studied the magnetoresistance in an oxygen deficient single crystal of YBCO with $T_c = 64$ K, at fields up to 24 T, and T down to 15 K. They find that the normally small Hall angle increases with falling temperatures, and reaches 70° at 13 K. This increase is due to the expected deviation of the vortex motion from perpendicular to the current towards parallel with increasingly clean conditions measured by $\omega_0\tau$. The same effect leads to the reduction in the ohmic component of the flux flow resistance. The ohmic resistivities of Ref. 300 are indeed very similar to those seen by us in Whisker 2. At temperatures below about 30 K, and fields above 10 T, they observed a slope $d\rho_f/dB$ of 2.4 μΩcm/T. This is similar to what

we found, but larger than the estimated value of 1.42 μΩcm/T calculated from Eq. (9.6) and an estimated $n_h$ based on $\tau_0$= 2500 Å [310] or oxygen-deficient YBCO. The linear dependence of the Hall angle on $\omega_0 \tau$ observed by them suggests that the universal limit is not quite reached.

In conclusion, we observed free flux flow behavior at low temperatures in the magnetoresistance of Bi 2212 Whiskers. For an underdoped whisker, we observe free flux flow down to 5.4 K in a field of 5.5 T. Below about 30 K, the free flux flow resistivity assumes a universal, temperature-independent value, in numerical agreement with the calculations of Kopnin and Volovik [299].

# Summary and Remarks

In the present work, the superconducting and normal-state properties of $Bi_2Sr_2CaCu_2O_{8+\delta}$ and $Bi_2Sr_2Ca_2Cu_3O_{10+\delta}$ had been systematically studied through transport measurements. New features were observed and the experimental data had been examined in various theoretical scenarios. Following a decreasing temperature scale from room temperature towards 4.2 K, the results in different temperature regions are summarized below.

1. ***Normal-state resistivity and evidence of structure instability near $T^* \sim 250$ K.*** This instability (or lattice distortion) now seems to be a *general feature* in the high-$T_c$ cuprates. Although resistance data are limited to very few material series, mechanical and diffraction (X-ray and neutron) measurements have all revealed evidence for structural anomalies in the same temperature region where anomalous resistance behavior were observed. This region marks a transition between the two regimes of linear-$T$ resistivity and pseudogap opening. It is believed the pseudogap phenomenon is closely related to this structural transformation. If the material undergoes some sort of microscopic ordering, e.g. antiferromagnetic correlation or stripe formation, it is natural to anticipate some effect on the lattice structure.
2. ***Bipolaronic conduction model.*** In the temperature range below the structural anomaly, the normal-state resistivity was checked in this scenario. We obtained satisfactory fittings to the experimental data, which was also consistent among our samples. The effective polaron mass was estimated. The superconducting fluctuation region was found to be much narrower ($\leq T_c + 50$ K) than the unusual case, which is expected in the picture of a charged Bose gas. It may still remain under debate whether the polaronic theory is applicable to the high-temperature superconductors.
3. ***Superconducting fluctuation.*** The $c$-axis coherence length values were extracted according to the dimensional crossover (2D to 3D below $T_0$) temperatures in the superconducting fluctuation conductance. A careful analysis of many of our resistivity curves showed that a nearly linear-$T$ segment exists in the plot of $d\rho/dT$ vs. $T$ within a temperature range above the fluctuation regime. We thus adopted an

empirical fitting to the normal-state resistivity and found a new definition for the superconducting fluctuation region, which is much narrower than what is widely accepted. The latter is evaluated from the linear *R-T* criterion.

4. ***The anisotropy factor***, $\gamma \equiv (m_c/m_{ab})^{1/2}$, was found to be about 183 for Bi-2212 and 364 for Bi-2223, by measuring the magnetoresistance for different field orientations (*H//ab* and *H//c*) and using the scaling method. Good scaling behavior was observed in the mixed-state.
5. ***Various regimes of flux motion in the mixed-state flux dynamics*** were observed in connection with different pinning conditions. Defect pinning due to surface degrading caused by thermal annealing was found to significantly affect the flux flow, which usually cause a thermally activated behavior, $\rho = \rho_0 exp(-U/T)$. At the low temperature tip, resistance was found to follow that of a pinned vortex liquid. The plastic barrier was confirmed to agree with the prediction: $U_{pl} \sim (1-T/T_c)/H^{1/2}$. A crossover to pure free flux flow (FFF) was found in clean samples with perfect surface morphology. The resistance can be fitted to the Bardeen-Stephen theory, $\rho_f = \rho_n H/H_{c2}$. In other cases, a possible combination of both plastic motion and FFF appears above the crossover temperature. A universal limit in flux flow resistivity was also deduced from the "superclean" regime and the peculiar resistivity was interpreted as originating from dissipation in vortex core state excitations.
6. ***I-V characteristics and critical current ($J_c$)*** were measured. Both $(1-T/T_c)$ and $(1-T/T_c)^{3/2}$ dependence of $J_c$ were observed at low temperature and near $T_c$, respectively. Precise *I-V* measurement also revealed evidence of mixed phases in the samples.

It would be meaningful to further explore the resistance anomaly in other series of cuprates. The influence of oxygen content and isotopic effects should also be checked. Since the microscopic magnetic structure plays an important role in electronic processes, high magnetic field studies may reveal new clues in clarifying such assumptions as spin-fluctuations. More interestingly, as many theories are proposing preformed pairing in the normal state, which leads to coherent pairing at superconducting transition, it will be crucial for an experimental determination of this pairing.

# References

## Chapter 1

1. R. M. Hazen, in *Physical Properties of High-Temperature Superconductors*, ed. by D. M. Ginsberg (World Scientific, Singapore 1990) Vol. 2, p.121.
2. J. D. Jorgensen, *Jpn. J. Appl. Phys. Suppl.* **26**(3), 2017 (1987).
3. R. J. Birgeneau and G. Shirane, in *Physical Properties of High-Temperature Superconductors*, ed. by D. M. Ginsberg (World Scientific, Singapore, 1989) Vol. 1, p.151.
4. R. Moret, J. P. Pouget, C. Nouera, and G. Collin, *Physica C* **153-155**, 968 (1988); H. J. Kim and R. Moret, *Physica C* **156**, 363 (1988).
5. C. Howard, R. J. Nelmes, and C. Vettier, *Solid State Commun.* **69**, 261 (1989).
6. J. D. Axe, A. H. Moudden, D. Hohkwein, D. E. Cox, K. M. Mohanty, A. R. Moodenbaugh, and Y. Xu, *Phys. Rev. Lett.* **62**, 2751 (1989).
7. T. Suzuki and T. Fujita, Physica C **159**, 111 (1989); T. Suzuki, M. Tagawa, and T. Fujita, *Physica C* **162-164**, 983 (1989).
8. K. I. Kumagai, I. Watanabe, K. Kawano, H. Matoba, K. Nishiyama, K. Nagamine, N. Wada, M. Okaji, and K. Nara, *Physica C* **185-189**, 913 (1991).
9. S. S. P. Parkin, V. Y. Lee, A. I. Nazzal, R. Savoy, T. C. Huang, G. Gorman, and R. Beyers, *Phys. Rev. B* **38**, 6531 (1988).
10. S. A. Sunshine *et al.*, *Phys. Rev. B* **38**, 893 (1988).
11. C. H. Chen, D. J. Werder, G. P. Espinosa, and A. S. Cooper, *Phys. Rev. B* **39**, 4686 (1989).
12. S. Horiuchi *et al., Jpn. J. Appl. Phys.* **27**, L1172 (1988).
13. Y. Hirotsu *et al., Jpn. J. Appl. Phys.* **27**, L1869 (1988).
14. A. K. Cheetham, A. M. Chippindale, and S. J. Hibble, *Nature* (London), **21**, 333 (1988).
15. H. W. Zandbergen, W. A. Groen, F. C. Mijlhoff, G. van Tendeloo, and S. Amelinckx, *Physica C* **156**, 325 (1988).

16. C. C. Torardi, J. B. Parise, M. A. Subramanian, J. Gopalakrishnan, and A. W. Sleight, *Physica C* **157**, 115 (1989).
17. A. Yamamoto, M. Onoda, E. Takayama-Muromachi, F. Izumi, T. Ishigaki, and H. Asano, *Phys. Rev. B* **42**, 4228 (1990).
18. W. Dmowdski, B. H. Toby, T. Egami, M. A. Subramanian, J. Gopalakrishnan, and A. W. Sleight, *Phys. Rev. Lett.* **61**, 2608 (1988).
19. C. C. Torardi, J. B. Parise, M. A. Subramanian, J. Gopalakrishnan, and A. W. Sleight, *Physica C* **157**, 115 (1989).
20. B. H. Tobi, T. Egami, J. D. Jorgensen, and M. A. Subramanian, *Phys. Rev. Lett.* **64**, 2414 (1990).
21. Y. Tokura, S. Koshihara, T. Arima, H. Takagi, S. Ishibashi, T. Ido, and S. Uchida, *Phys. Rev. B* **41**, 11657 (1990); K. B. Lyons, P. A. Fleury, J. P. Remeika, A. S. Cooper, and T. J. Negran, *Phys. Rev. B* **37**, 2353 (1988); S. L. Cooper *et al.*, *Phys. Rev. B* **42**, 10785 (1990).
22. M. Imada, A. Fujimori, and Y. Tokura, *Rev. Mod Phys.* **70**, 1039 (1998).
23. S. Chakravarty, B. I. Halperin, and D. R. Nelson, *Phys. Rev. Lett.* **60**, 1057 (1988); *Phys. Rev. B* **39**, 2344 (1989).
24. P. Hasenfratz and F. Niedermayer, *Phys. Lett.* B **268**, 231 (1991).
25. B. B. Beard, R. J. Birgeneau, M. Greven, and U.-J. Wiese, *Phys. Rev. Lett.* **80**, 1742 (1998).
26. M. A. Kastner, R. J. Birgeneau, G. Shirane, and Y. Endoh, *Rev. Mod. Phys.* **70**, 897 (1998).
27. R. J. Birgeneau *et al.*, *Phys. Rev. B* **38**, 6614 (1988).
28. K. Yamada *et al.*, *J. Phys. Soc. Jpn.* **64**, 2742 (1995); K. Yamada *et al.*, *Phys. Rev. Lett.* **75**, 1626 (1995); H. Yoshizawa, S. Mitsuda, H. Kitazawa, and K. Tatsumata, *J. Phys. Soc. Jpn.* **57**, 3686 (1988).
29. S-W. Cheong *et al.*, *Phys. Rev. Lett.* **67**, 1791 (1991).
30. T. R. Thurston *et al.*, *Phys. Rev. B* **40**, 4585 (1989).
31. G. Apeppli, T. E. Mason, S. M. Hayden, H. A. Mook, and J. Kulda, *Science* **278**, 1432 (1997).

32. C. H. Pennington and C. P. Slitchter, in *Physical Properties of High-Temperature Superconductors*, ed. by D. M. Ginsberg (World Scientific, Singapore, 1990) Vol. 2, p.269.
33. A. J. Millis, H. Monien, and D. Pines, *Phys. Rev. B* **42**, 167 (1990).
34. T. Moriya, Y. Takahashi, and K. Ueda, *J. Phys. Soc. Jpn.* **59**, 2905 (1990).
35. J. M. Tranquada, D. E. Cox, W. Kunnmann, A. H. Moudden, G. Shirane, M. Suenaga, P. Zolliker, D. Vaknin, S. K. Sinha, M. S. Alvares, A. J. Jacobson, and D. C. Johnston, *Phys. Rev. Lett.* **60**, 156 (1988).
36. N. M. Plakida, *High-Temperature Superconductivity --- Experiment and Theory* (Springer-Verlag, Heidelberg, 1995).
37. See, for example, Y. Itoh, T. Machi, A. Fukuoka, K. Tanabe, and H. Yasuoka, *J. Phys. Soc. Jpn.* **65**, 3751 (1996); C. Berthier, M.-H. Julien, M. Horvatic, and Y. Berthier, *J. Phys.* (France) **6** 2205 (1996); C. Berthier, M.-H. Julien, O. Bakharev, M. Horvatic, and P. Segransan, *Physica C* **282-287**, 227 (1997).
38. H. Yasuoka, *Physica C* **282-287**, 119 (1997).
39. Y. Itoh, M. Matsumura, and H. Yamagata, *J. Phys. Soc. Jpn.* **66,** 3383 (1997).
40. Y. Itoh, T. Machi, S. Adachi, A. Fukuoka, K. Tanabe, and H. Yasuoka, *J. Phys. Soc. Jpn.* **67,** 393 (1998).
41. J. Bobroff, H. Alloul, P. Mendels, V. Viallet, J. -F. Marucco, and D. Colson, *Phys. Rev. Lett.* **78**, 3757 (1997).
42. H. A. Mook, Penchang Dai, S. M. Hayden, G. Aeppli, T. G. Perring, and F. Doğan. *Nature* (London) **395**, 580 (1998).
43. J. Rossat-Mignod *et al.*, *Physica B* **169**, 58 (1991); Rossat-Mignod, J. L. P. Regnault, C. Vettier, P. Bourges, P.Burlet, J. Bossy, J. Y. Henry, and G. Lapertot, *Physica C* **185-189**, 86 (1991); J. Tranquada *et al.*, *Phys. Rev. B* **46**, 5561 (1992).
44. F. F. Assaad, M. Imada, and D. Scalapino, *Phys. Rev. B* **56**, 15001 (1997).
45. P. W. Anderson, *Science* **235**, 1196 (1987); Y. Suzumura, Y. Hasegawa, and H. Fukuyama, *J. Phys. Soc. Jpn.* **57**, 2768 (1988); M. U. Ubbens and P. A. Lee, *Phys. Rev. B* **50**, 438 (1994).
46. D. Pines, in *High Temperature Superconductors and the $C_{60}$ System*, ed. Ren. H-C., (Gordon & Breach, 1995), p.1.

47. H. F. Fong, P. Bourges, Y. Sidis, L. P. Regnault, A. Ivanov, G. D. Gu, N. Koshizuka, and B. Keimer, *Nature* (London), **398**, 588 (1999).

48. D. J. Scalapino and S. R. White, *Phys. Rev. B* **58**, 8222 (1998).

49. E. Demler and S. C. Zhang, *Nature* (London) **396**, 733 (1998).

50. Pengcheng Dai, H. A. Mook, S. M. Hayden, G. Aeppli, T. G. Perring, R. D. Hunt, and F. Doğan, *Science*, **284**, 1344 (1999).

51. A. Kampf and J. R. Schrieffer, *Phys. Rev. B* **41**, 6399 (1990).

52. P. Aebi, J. Osterwalder, P. Schwaller, L. Schlapbach, M. Shi-moda, T. Mochiku, and K. Kadowaki, *Phys. Rev. Lett.* **72**, 2757 (1994).

53. H. Ding, A. F. Bellman, J. C. Campuzano, M. Randeria, M. R.Norman, T. Yokoya, T. Takahashi, H. Katayama-Yoshida, T.Mochiku, K. Kadowaki, G. Jennings, and G. P. Brivio, *Phys. Rev. Lett.* **76**, 1533 (1996).

54. V. J. Emery and S. A. Kivelson, *Physica C* **209**, 597 (1993).

55. M. I. Salkola, V. J. Emery, and S. A. Kivelson, *Phys. Rev. Lett.* **77**, 155 (1996).

56. C. N. A. van Duin and J. Zaanen, *Phys. Rev. Lett.* **80**, 1513 (1998).

57. C. Castellani, C. D. Castro, and M. Grilli, *Phys. Rev. Lett.* **75**, 4650 (1995).

58. A.H. Castro Neto and D. Hone, *Phys. Rev. Lett.* **76**, 2165 (1996); A. H. Castro Neto and F. Guinea, *ibid.* **80**, 4040 (1998); A. H. Castro Neto, *Z. Phys. B* **103**, 185 (1997).

59. A. H. Castro Neto, *Phys. Rev. Lett.* **78**, 3931 (1997);

60. J. M. Tranquada, J. D. Axe, N. Ichikawa, A. R. Moodenbaugh, Y. Nakamura, and S. Uchida, *Phys. Rev. Lett.* **78**, 338 (1997).

61. B. Nachumi, Y. Fudamoto, A. Keren, K. M. Kojima, M. Larkin, G. M. Luke, J. Merrin, O. Tchernyshyov, Y. J. Uemura, N. Ichikawa, M. Goto, H. Takagi, S. Uchida, M. K. Crawford, E. M. McCarron, D. E. MacLaughlin, and R. H. Heffner, *Phys. Rev. B* **58**, 8760 (1998).

62. M. V. Zimmermann, A. Vigliante, T. Niemöller, N. Ichikawa, T. Frello, J. Madsen, P. Wochner, S. Uchida, N. H. Andersen, J. M. Tranquada, D. Gibbs, and J. R. Schneider, *Europhys. Lett.* **41**, 629 (1998).

63. Z.-X. Shen, P. J. White, D. L. Feng, C. Kim, G. D. Gu, H. Ikeda, R. Yoshizaki, and N. Koshizuka, *Science* **280**, 259 (1998).

64. A. Bianconi and M. Missori, *Solid State Commun.* **91**, 287 (1994); A. Bianconi, M. Missori, H. Oyanagi, H. Yamaguchi, D. H. Ha, Y. Nishiara, and S. Della Longa, *Europhys. Lett.* **31**, 411 (1995); A. Bianconi, *Physica C* **235-240**, 269 (1994).
65. A. Bianconi, N. L. Saini, A. Lanzra, M. Missori, T. Rosseti, H. Oyanagi, H. Yamaguchi, K. Oka, and T. Ito, *Phys. Rev. Lett.* **76**, 3412 (1996).
66. K. Kumagai, K. Kawano, I. Watanabe, K. Nishiyama, and K. Nagamine, *J. Supercond.* **7**, 63 (1994).
67. J. M. Tranquada, B. J. Sternlieb, J. D. Axe, Y. Nakamura, and S. Uchida, *Nature* (London) **375**, 561 (1995).
68. M. R. Presland, J. L. Tallon, R. G. Buckley, R. S. Liu, and N. E. Flower, *Physica C* **176**, 95 (1991).
69. David Lawrie, *Ph.D. Dissertation*, University of Alberta, 1999.
70. T. Huang, L. Yu, Y. Zhang, M. Itoh, J. D. Yu, Y. Inaguma, T. Nakamura, *Physica C* **271**, 103 (1996).
71. M.-H, Whangbo, D. B. Kang, and C. C. Torardi, *Physica C* **158**, 371 (1989).
72. C. N. R. Rao and A. K. Ganguli, *Physica C* **235-240**, 9 (1994).

## Chapter 2

73. C. Michel, M. Hervieu, M. M. Borel, A. Grandin, F. Deslandes, J. Provost, and B. Raveau, *Z. Phys. B* **68**, 421 (1987).
74. H. Maeda, Y. Tanaka, M. Fukutomi, and T. Asano, *Jpn. J. Appl. Phys.* **27**, L209 (1988).
75. J. Jung, J.P. Franck, D. F. Mitchell, and H. Claus, *Physica C* **156**, 494 (1988).
76. J. Jung, J. P. Franck, S. C. Cheng, and S. S. Sheinin, *Jpn. J. Appl. Phys.* **28**, L1182 (1989).
77. V. N. Timofeev and I. G. Gorlova, *Physica C* **309**, 113 (1998).
78. R. S. Wagner and W. C. Ellis, *Appl. Phys. Lett.* **4**, 89 (1964).
79. A. B. Bykov, L. N. Demyanets, and E. M. Smirnovskaya, *Supercond. Phys. Chem. Tech.* **6**, 1008 (1993).
80. H. Jin, Z. Hu, Y. Ge, Q. Liu, C. Liu, and C. Shi, *Physica C* **211**, 49 (1993).

81. I. Matsubara, R. Funahashi. T. Ogura, H. Yamashita. K. Tsuru, and T. Kawai. *J. Cryst. Growth* **94**, 281 (1989).
82. S. Lee, K.-J. Kwon, W.-S. Kim, and S.-Ik Lee, *Physica C* **251**, 149 (1995).
83. I. Matsubara, H. Kageyama, H. Tanigawa, T. Ogura, H. Yamashita, and T. Kawai. *Jpn. J. Appl. Phys.* **28**, L1121 (1989); *ibid.* **28**, L1358 (1989); *Appl. Phys. Lett*. **56**. 2141 (1990).
84. Y.I. Latyshev, I. G. Gorlova, A. M. Nikitana, V. U. Antokhina, S. G. Zybtsev, N. P. Kukhta, and V. N. Timofeev, *Physica C* **216**, 471 (1993).
85. X. F. Chen, G. X. Tessema, and M. J. Skove, *Phys. Rev. B* **48**, 13141 (1993).
86. G. X. Tessema. X. F. Chen, and M. J. Skove, *Physica C* **185-189**, 1783 (1991).
87. R. H. Arendt, M. F. Garbauskas, and P. J. Bednarczyk, *Physica C* **176**, 126 (1991).
88. Ichiro Matsubara and Hiroshi Yamashita, *J. Crystal Growth*. **128**, 719 (1993).
89. M. Chung, D. T. Verebelyi, C. W. Schneider, M. V. Nevitt, M. J. Skove, J. E. Payne, M. Marone, and P. Kostic, *Physica C* **65**, 301 (1996).
90. H. Hayakawa, M. Kaise. K. Nakamura, and K. Ogawa, *Jpn. J. App. Phys*. **28**. L967 (1989).
91. P.V.P.S.S. Sastry and A. R. West. *Physica C* **250**. 87 (1995), and references therein.
92. Y. Abe, K. Hirata, H. Hosono, and Y. Kubo, *J. Mater. Res* **7**, 1599 (1992); T. Kasuga, M. Ono, K.Tsuji, Y. Abe, K. Nakamura, and E. Inukai, *ibid.* **9**, 1098 (1994).

## Chapter 3

93. P.W. Anderson. S. Chakravarty. S. Strong, and A. Sudbo. *Science* **261**, 337 (1993); See also P. W. Anderson. *The Theory of Superconductivity in the High-$T_c$ Cuprates* (Princeton University Press, Princeton, NJ, 1997).
94. P. B. Allen, Z. Fisk, and A. Migliori, in *Physical Properties of High-Temperature Superconductors*, ed. D. M. Ginsberg (World Scientific, Singapore, 1989) Vol. 1. p.213.
95. N. P. Ong, in *Physical Properties of High-Temperature Superconductors*, ed. D. M. Ginsberg (World Scientific, Singapore, 1990) Vol.2, p.459; *Physica C* **235-240**. 221 (1994).

96. H. Takagi, B. Batlogg, H. L. Kao, J. Kwo, R. J. Cava, J. J. Krajewski, and W. F. Peck, Jr., *Phys. Rev. Lett.* **69**, 2875 (1992);

97. M. Gurvitch and A. T. Fiory, *Phys. Rev. Lett.* **59**, 1337 (1987).

98. T. Watanabe, T. Fujii, and A. Matsuda, *Phys. Rev. Lett.* **79**, 2113 (1997).

99. B. Batlogg, H. Y. Hwang, H. Takagi, R. J. Cava, H. L. Kao, and J. Kwo, *Physica C* **235-240**, 130 (1994).

100. S. Uchida, *Physica C* **282-287**, 12 (1997).

101. Y. Nakamura and S. Uchida, *Phys. Rev. B* **47**, 8369 (1993).

102. J. L. Tallon, C. Bernhard, G. V. M. Williams, and J. W. Loram, *Phys. Rev. Lett.* **79**, 5249 (1997).

103. T. Ito, K. Takenaka, and S. Uchida, *Phys. Rev. Lett.* **70**, 3995 (1993).

104. K. Takenaka, K. Mizuhashi, H. Takagi, and S. Uchida, *Phys. Rev. B* **50**, 6534 (1994); K. Mizhuhashi, K. Takenaka, Y. Fukuzumi, and S. Uchida, *ibid.* **52**, R3884 (1995).

105. B. Wuyts, V. V. Moshchalkov, and Y. Bruynseraede, *Phys. Rev. B* **53**, 9418 (1996).

106. B. Bucher, P. Steiner, J. Karpinski, E. Kaldis, and P. Wachter, *Phys. Rev. Lett.* **70**, 2012 (1993).

107. C. Kendziora, M. C. Martin, J. Hartge, and L. Mihaly, *Phys. Rev. B* **48**, 3531 (1993).

108. Zhiqiang Mao, G. Xu, R. Wang, K. Wang, M. Tian, Y. Zhang, *Phys. Rev. B* **55**, 14581 (1997).

109. K. Knizek *et al.*, *Physica C* **302**, 209 (1998).

110. H. Yasuoka, T. Imai, and T. Shimizu, in *Strong Correlations and Superconductivity*, ed. by H. Fukuyama, S. Maekawa, and A. P. Malozemoff (Springer-Verlag, Berlin, 1989), p. 254.

111. A. J. Millis and H. Monien, *Phys. Rev. Lett.* **70**, 2810 (1993).

112. G. V. M. Williams, J. L. Talon, R. Michalak, and R. Dupree, *Phys. Rev. B* **54**, R6909 (1996).

113. M. Takigawa, A. P. Reyes, P. C. Hammel, J. D. Thompson, R. H. Heffner, Z. Fisk, and K. C. Ott, *Phys. Rev. B* **43**, 247 (1991).

114. M. Takigawa, W. L. Hults, and J. L. Smith, *Phys. Rev. Lett.* **71**, 2650 (1993).

115. R. Dupree *et al., Physica C* **179**, 311 (1991).

116. A. J. Millis and H. Monien, *Phys. Rev. B* **50**, 16606 (1994).

117. I. Tomino *et al., Phys. Rev. B* **49**, 15327 (1994).

118. N. Winzek *et al., Physica C* **205**, 45 (1993).

119. M.-H. Julien, P. Carretta, M. Horvatić, C. Berthier, Y. Berthier, P. Ségransan, A. Carrington, and D. Colson, *Phys. Rev. Lett.* **76**, 4238 (1996).

120. D. N. Basov, T. Timusk, B. Dabrowski, and J. D. Jorgensen, *Phys. Rev. B* **50**, 3511 (1994); D. N. Basov, R. Liang, B. Dabrowski, D. A. Bonn, W. N. Hardy, and T. Timusk, *Phys. Rev. Lett.* **77**, 4090 (1996).

121. A. V. Puchkov, P. Fournier, D. N. Basov, T. Timusk, A. Kapitulnik, and N. N. Kolesnikov, *Phys. Rev. Lett.* **77**, 3212 (1996); A. V. Puchkov, D. N. Basov, and T. Timusk, *http://xxx.lanl.gov/cond-mat/*9611083, and references therein.

122. R. Hauff, S. Tajima, W.-J. Jang, and A. I. Rykov, *Phys. Rev. Lett.* **77**, 4620 (1996).

123. Z.-X. Shen and D. S. Dessau, *Phys. Rep.* **253**, 1, (1995); Z.-X. Shen *et al., Science* **267**, 343 (1995).

124. D. S. Marshall, D. S. Dessau, A. G. Loeser, C-H. Park, A. Y. Matsuura, J. N. Eckstein, I. Bozovic, P. Fournier, A. Kapitulnik, W. E. Spicer, and Z.-X. Shen, *Phys. Rev. Lett.* **76**, 4841 (1996).

125. H. Ding, M. R. Norman, T. Yokoya, T. Takeuchi, M. Randeria, J. C. Campuzano, T. Takahashi, T. Mochiku, and K. Kadowaki, *Phys. Rev. Lett.* **78**, 2628 (1997); A. G. Loeser, Z.-X. Shen, D. S. Dessau, D. S. Marshall, C. H. Park, P. Fournier, and A. Kapitulnik, *Science* **273**, 325 (1996).

126. N. L. Saini, J. Avila, A. Bianconi, A. Lanzana, M. C. Asensio, S. Taijima, G. D. Gu, and N. Koshizuka, *Phys. Rev. Lett.* **79**, 3467 (1997).

127. A. Ino, T. Mizokawa, K. Kobayashi, A. Fujimori, T. Sasagawa, T. Kimura, K. Kishio, K. Tamasaku, H. Eisaki, and S. Uchida, *Phys. Rev. Lett.* **81**, 2124 (1998).

128. K. Yamada, S. Wakimoto, G. Shirane, C. H. Lee, M. A. Kastner, S. Hosoya, M. Greven, Y. Endoh, and R. J. Birgeneau, *Phys. Rev. Lett.* **75**, 1626 (1995).

129. P. Dai, M. Yethiraji, H. A. Mook, T. B. Lindemer, and F. Doğan, *Phys. Rev. Lett.* **77**, 5425 (1996).

130. P. Dai, H. A. Mook, and F. Doğan, *Science* **80**, 1738 (1998).

131. Ch. Renner, B. Revaz, J.-Y. Genoud, K. Kadowaki, and Ø. Fischer, *Phys. Rev. Lett.* **80**, 149 (1998); Ch. Renner, B. Revaz, K. Kadowaki, I. Maggio-Aprile, and Ø. Fischer, *ibid.* **80**, 3606 (1998).

132. N. Miyakawa, P. Guptasarma, J. F. Zasadzinski, D. G. Hinks, and K. E. Gray, *Phys. Rev. Lett.* **80**, 157 (1998).

133. R. Nemetschek, M. Opel, C. Hoffmann, P. F. Müller, R. Hackl, H. Berger, L. Forró, A. Erb, and E. Walker, *Phys. Rev. Lett.* **78**, 4837 (1997).

134. H. Y. Hwang *et al., Phys. Rev. Lett.* **72**, 2636 (1994).

135. V. Barzykin and D. Pines, *Phys. Rev. B* **52**, 13585 (1995).

136. H. Yasuoka, *Physica C* **282-287**, 119 (1997).

137. Robert Joynt, *Science* **284**, 777 (1999); A. J. Arko, *ibid.* **284**, 752 (1999).

138. S. Uchida, K. Tamasaku, K. Takenaka, and Y. Fukuzumi, *J. Low Temp. Phys.* **105**, 723 (1996).

139. H. Ding *et al.*, *Nature* (London) **382**, 51 (1996).

140. G. V. M. Williams, J. L. Tallon, E. M. Haines, R. Michalak, and R. Dupree, *Phys. Rev. Lett.* **78**, 721 (1997).

141. Guy Deutscher, *Nature* (London), **397**, 410 (1999).

142. D. Pines, *Z. Phys. B* **103**, 129 (1997).

143. N. Miyakawa *et al., Phys. Rev. Lett.* **80**, 157 (1998).

144. J. Corson, R. Mallozzi, J. Orenstein, J. N. Eckstein, and I. Bozovic, *Nature* (London) **398**, 221 (1999).

145. P. Monthoux and D. Pines, *Phys. Rev. B* **47**, 6069 (1993); **49**, 4261 (1994).

146. Branko P. Stojković and D. Pines, *Phys. Rev. B* **55**, 8576 (1997), and references therein.

147. V. J. Emery and S. A. Kivelson, *Nature* (London) **374**, 434 (1995).

148. J. Zaanen A. M. Oleś, *Ann. Phys.* (Leipzig) **5**, 224 (1996).

149. C. N. A. van Duin and J. Zaanen, *Phys. Rev. Lett.* **80**, 1513 (1998).

150. G. Baskaran, Z. Zou, and P. W. Anderson, *Solid State Commun.* **63**, 973 (1987); P. W. Anderson, *Science* **235**, 1196 (1987).

151. G. Kotliar and J. Liu, *Phys. Rev. B* **38**, 5142 (1988).

152. H. Fukuyama, *Prog. Theor. Phys. Suppl.* **108**, 287 (1992).

153. P. A, Lee and X. G. Wen, *Phys. Rev. Lett.* **76**, 503 (1996); Naoto Nagaosa and P. A. Lee, *ibid.* **64**, 2450 (1990).

154. C. Kim, A. Y. Matsuura, Z.-X. Shen, N. Motoyama, H. Eisaki, S. Uchida, T. Tohyama, and S. Maekawa, *Phys. Rev. Lett.* **77**, 4054 (1996); C. Kim, Z.-X. Shen, N. Motoyama, H. Eisaki, S. Uchida, T. Tohyama, and S. Maekawa, *Phys. Rev. B* **56**, 15589 (1997).

155. M. Marezio and P. D. Dernier, *J. Solid State Chem.* **3**, 340 (1971); B. K. Chakraverty, M. J. Sienko, and J. Bonnerot, *Phys. Rev. B* **17**, 3781 (1978); S. Lakkis *et al.*, *Phys. Rev. B* **14**, 1429 (1976); R. Gehlig and E. Salje, *Phil. Mag. B* **47**, 229 (1983).

156. A. S. Alexandrov, A. M. Bratkovsky, and N. F. Mott, *Phys. Rev. Lett.* **72**, 1734 (1994); *Supercond. Sci. Technol.* **6**, 755 (1993).

157. A. S. Alexandrov, V. V. Kabanov, and N. F. Mott, *Phys. Rev. Lett.* **77**, 4796 (1996).

158. A. S. Alexandrov, *Phys. Lett.* A **236**, 132 (1997); *Physica C* **282-287**, 269 (1997).

159. A. S. Alexandrov and P. E. Kornilovitch, *Phys. Rev. Lett.* **82**, 807 (1999).

160. A. S. Alexandrov and N. F. Mott, *Rep. Prog. Phys*. **57**, 1197 (1994); *High Temperature Superconductors and Other Superfluids* (Taylor and Francis, London, 1994).

161. J. Ranninger, *Physica C* **235-240**, 277 (1994).

162. G. Iadonisi, V. Cataudella, D. Ninno, and M. L. Chiofalo, *Phys. Lett. A* **196**, 359 (1995).

163. M. Capizzi, S. Lupi, P. Calvani, P. Maselli, A. Paolone, P. Roy, H. Berger, and G. Balestrino, *Physica C* **235-240**, 273 (1994).

164. K. A. Muller, Guo-meng Zhao, K Conder, and H. Keller, *J. Phys.: Condens. Matter* **10**, L291 (1998).

165. A. P. Mackenzie, S. R. Julian, D. C. Sinclair, and C. T. Lin, *Phys. Rev. B* **53**, 5848 (1996).

166. R. Hlubina and T. M. Rice, *Phys. Rev. B* **51**, 9253 (1995).

167. B. K. Chakraverty, J. Ranninger, and D. Feinberg, *Phys. Rev. Lett.* **81**, 433 (1999), and its comments: *ibid.* **82**, 2621; A. S. Alexandrov, *ibid.* **82**, 2620 (1999).

168. P. W. Anderson, *Science* **268**, 1154 (1995); *ibid.* **279**, 1196 (1999).

169. D. van der Marel *et al., Physica C* **235-240**, 1145 (1994).

170. A. J. Leggett, *Science* **274**, 587 (1996).

171. K. Moler, J. R. Kirtley, D. G. Hinks, T. W. Li, and Ming Xu, *Science* **279**, 1193 (1999); J. R. Kirtley, K. A. Moler, G. Villard, and A. Maignan, *Phys. Rev. Lett.* **81**, 2140 (1998).

172. N. E. Hussey, K. Nozawa, H. Takagi, S. Adachi, and K. Tanabe, *Phys. Rev. B* **56**, R11423 (1997); N. E. Hussey, M. Kibune, H. Nakagawa, N. Miura, Y. Iye, H. Takagi, S. Adachi, and K. Tanabe, *Phys. Rev. Lett.* **80**, 2909 (1998).

173. A. N. Lavrov, M. Yu. Kameneva, and L. P. Kozeeva, *Phys. Rev. Lett.* **81**, 5636 (1998).

174. Mohit Randeria, *http://xxx.lanl.gov/cond-mat/*9710223.

175. K. Gorny *et al., Phys. Rev. Lett.* **82**, 177 (1999).

## Chapter 4

176. J. M. Tranquada, B. J. Sternlieb, J. D. Axe, Y. Nakamura, and S. Uchida, *Nature* (London) **375**, 561 (1995).

177. Y. Nakamura and S. Uchida, *Phys. Rev. B* **46**, 5841 (1992).

178. J. M. Tranquada, J. D. Axe, N. Ichikawa, Y. Nakamura, S. Uchida and B. Nachumi, *Phys. Rev. B* **54**, 7489 (1996).

179. M. Akoshima, T. Noji, Y. Ono, and Y. Koike, *Phys. Rev. B* **57**, 7491 (1998).

180. T. M. Tritt, M. Marone, A. C. Ehrlich, M. J. Skove, D. J. Gillespie, R. L. Jacobsen, G. X. Tessema, J. P. Franck, and J. Jung, *Phys. Rev. Lett.* **68**, 2531 (1992).

181. G.A. Levin and K.F. Quader, *Phys. Rev. B* **46**, 5872 (1992).

182. M. Chung, D. T. Verebelyi, C. W. Schneider, M. V. Nevitt, M. J. Skove, J. E. Payne, M. Marone, and P. Kostic, *Physica C* **265**, 301 (1996).

## Chapter 5

183. For a review on ultrasonic measurements, see J. Dominec, *Supercond. Sci. Technol.* **6**, 153 (1993).

184. A. Migliori, W. M. Visscher, S. Wong, S. E. Brown, I. Tanaka, H. Kojima, and P. B. Allen, *Phys. Rev. Lett.* **64**, 2458 (1990).

185. J. Thoulous, X. M. Wang, and D. J. L. Hong, *Phys. Rev. B* **38**, 7077 (1988).

186. S. Hoen *et al.*, *Phys. Rev. B* **38**, 11949 (1988).

187. X. D. Shi *et al.*, *Phys. Rev. B* **39**, 827 (1989).

188. J. Dominec, C. Laermans, and V. Plechéček, *Physica C* **171**, 373 (1991).

189. Ye-Ning Wang *et al.*, *Phys. Rev. B* **41**, 8981 (1990).

190. O-M Nes *et al.*, *Supercond. Sci. Technol.* **4**, S388 (1991).

191. Yusheng He, Jiong Xiang, Xin Wang, Aisheng He, Jinchang Zhang, and Panggao Chang, *Phys. Rev. B* **40**, 7384 (1989); T. Fukami, A. A. A. Youssef, Y. Horie, and S. Mase, *Physica C* 161, 34 (1989); V. Plechéček, and J. Dominec, *Solid State Commun.* **74**, 6339 (1990).

192. S. Titova, I. Bryntse, J. Irvine, B. Mitchell, and V. Balakirev, *J. Supercond.* **11**, 471 (1998).

193. I. G. Gorlova, and V. N. Timofeev, *Physica C* **255**, 131 (1995).

194. Weimin Chen, J. P. Franck, J. Jung, *Phys. Rev. B* **60**, 3527 (1999).

195. R. H. Ardent, M. F. Garbauskas, C. A. Meyer, F. J. Rotella, J. D. Jorgensen, and R. L. Hitterman, *Physica C* **182**, 73 (1991).

196. Xin-Fen Chen, G. X. Tessema, and M. J. Skove, *Physica C* **181**, 340 (1991).

197. P. M. Hall, S. Legvold, and F. H. Spedding, *Phys. Rev.* **117**, 971 (1960).

198. S. von Molnar, *IBM J. Res. Develop.* **14**, 269 (1970); F. C. Schwerer and J. Silcox, *Phys. Rev. Lett.* **20**, 101 (1968); M. E. Fisher and J. S. Langer, *ibid.* **20**, 665 (1968).

199. S. Takada, *Prog. Theor. Phys.* **46**, 15 (1971).

200. P. G. de Gennes and J. Friedel, *J. Phys. Chem. Solids* **4**, 71 (1958).

201. Y. Iye, S. Nakamura, and T. Tamegai, *Physica C* **159**, 616 (1989).

## Chapter 6

202. L. G. Aslamazov and A. I. Larkin, *Phys. Lett.* **26A**, 238 (1968).

203. D. H. Kim, A. M. Goldman, J. H. Kang, K. E. Gray, and R. T. Kampwirth, *Phys. Rev. B* **39**, 12275 (1989).

204. A. K. Pradhan, S. B. Roy, P. Chaddah, C. Chen, and B. M. Wanklyn, *Phys. Rev. B* **50**, 7180 (1994).

205. A. Gauzzi and D. Pavuna, *Phys. Rev. B* **51**, 15420 (1995).

206. S. H. Han and Ö. Rapp, *Solid State Commun.* **94**, 661 (1995).

207. A. Pomar, M. V. Ramallo, J. Mosqueira, C. Torrón, and F. Vidal, *Phys. Rev. B* **54**, 7470, (1996); M. V. Ramallo, A. Pomar, and F. Vidal, *Phys. Rev. B* **54**, 4341 (1996).

208. W. Lang, G. Heine, W. Kula, and R. Sobolewski, *Phys. Rev. B* **51**, 9180 (1995).

209. A. Wahl, A. Maignan, C. Martin, V. Hardy, J. Provost, and Ch. Simon, *Phys. Rev. B* **51**, 9123 (1995).

210. X.-F. Chen, M. J. Marone, G. X. Tessema, M. J. Skove, M. V. Nevitt, D. J. Miller, and B. W. Veal, *Phys. Rev. B* **48**, 1254 (1993).

211. S. V. Sharma, G. Sinha, T. K. Nath, S. Chakraborty, and A. K. Majumdar, *Physica C* **242**, 351 (1995).

212. Q. Wang, G. A. Saunders, H. J. Liu, M. S. Acres, and D. P. Almond, *Phys. Rev. B* **55**, 8529 (1997).

213. S. Ullah and A. T. Dorsey, *Phys. Rev. B* **44**, 262 (1991).

214. D. V. Livanov, E. Milani, G. Balestrino, and C. Aruta, *Phys. Rev. B* **55**, R8701 (1997).

215. S. H. Han, Yu. Eltsev, and Ö. Rapp, *Phys. Rev. B* **57**, 7510 (1998).

216. P. Mandel, A. Poddar, A. N. Das, and B. Ghosh, *Physica C* **169**, 43 (1990).

217. W. E. Lawrence and S. Doniach, in *Proceedings of the 12th international Conference on Low Temperature Physics*, ed. E. Kanda (Keigaku, Tokyo, 1971), p.361.

218. V. B. Geshkenbein, L. B. Ioffe, and A. I. Larkin, *Phys. Rev. B* **55**, 3173 (1997).

219. W. J. Skocpol and M. Tinkham, *Rep. Prog. Phys.* **38**, 1409 (1975).

220. I. G. Gorlova, S. G. Zybtsev, V. Ya. Pokrovskii, and V. N. Timofeev, *Physica C* **282-287**, 1533 (1997); Yu. I. Latyshev, I. G. Gorlova, A. M. Nikitina, Y. U.

Antokhina, S. G. Zybtsev, N. P. Kukhta, and V. N. Timofeev, *Physica C* **216**, 471 (1993).

## Chapter 7

221. Ernst Helmut Brandt, *Rep. Prog. Phys.* **58**, 1465 (1995).
222. G. Blatter, M. V. Feilgel'man, V. B. Geshkenbein, A. I. Larkin, and V. M. Vinokur, *Rev. Mod. Phys.* **66**, 1125 (1994).
223. G. W. Crabtree, *Physics Today*, April issue, 1997.
224. David Nelson and H. Sebastian Seung, *Phys. Rev. B* **39**, 9153 (1989).
225. D. S. Fisher, M. P. A. Fisher, and D. A. Huse, *Phys. Rev. B* **43**, 130 (1991).
226. D. J. Bishop, P. L. Gammel, D. A. Huse, and C. A. Murray, *Science* **255**, 165 (1992).
227. L. I. Glazman and A. E. Koshelev, *Phys. Rev. B* **43**, 2835 (1991).
228. H. Pastoriza, M. F. Goffman, A. Arribére, and F. de la Cruz, *Phys. Rev. Lett.* **72**, 2951 (1994).
229. E. Zeldov, D. Majer, M. Konczykowski, V. B. Geshkenbein, V. M. Vinokur, and H. Shtrikman, *Nature*(London) **375**, 373 (1995); D. T. Fuchs, E. Zeldov, D. Majer, R. A. Doyle, T. Tamegai, S. Ooi, and M. Konczykowski, *Phys. Rev. B* **54**, R796 (1996); R. A. Doyle, B. Khaykovich, M. Konczykowski, E. Zeldov, N. Morozov, D. Majer, P. H. Kes, and V. Vinokur, *Physica C* **282-287**, 323 (1997).
230. Ruixing Liang, D. A. Bonn, and W. N. Hardy, *Phys. Rev. Lett.* **76**, 835 (1996).
231. Y. Kopelevic, S. Moehlecke, and J. H. S. Torres, *Phys. Rev. B* **49**, 1495 (1994).
232. T. Sasagawa, K. Kishio, Y. Togawa, J. Shimoyama, and K. Kitazawa, *Phys. Rev. Lett.* **80**, 4297 (1998).
233. T. Nishizaki, Y. Onodera, and N. Kobayashi, *Phys. Rev. B* **53**, 82 (1996).
234. W. K. Kowk, J. Fendrich, S. Fleshler, U. Welp, J. Downey, and G. W. Crabtree, *Phys. Rev. Lett.* **72**, 1092 (1994); W. K. Kwok, S. Fleshler, U. Welp, V. M. Vinokur, J. Downey, G. W. Crabtree, and M. M. Miller, *ibid.* **69**, 3370 (1992); J. A. Fendrich, U. Welp, W. K. Kowk, A. E. Koshelev, G. W. Crabtree, and B. W. Veal, *ibid.* **77**, 2073 (1996).

235. H. Safar, P. L. Gammel, D. A. Huse, D. J. Bishop, W. C. Lee, J. Giapintzakis, and D. M. Ginsberg, *Phys. Rev. Lett.* **70**, 3800 (1993); H. Safar, P. L. Gammel, D. A. Huse, D. J. Bishop, J. R. Rice, and D. M. Ginsberg, *ibid.* **69**, 824 (1992); P. L. Gammel, L. F. Schneemeyer, and D. J. Bishop, *ibid.* **66**, 953 (1991).

236. H. Ikuta, S. Watauchi, H. Kobayashi, Y. Nakamura, J. Shimoyama, K. Kitazaw, and K. Kishio, *Physica C* **282-287**, 2015 (1997); S. Watauchi, H. Ikuta, J. Shimoyama, and K. Kishio, *ibid.* **259**, 373 (1996).

237. D. T. Fuchs, R. A. Doyle, E. Zeldov, D. Majer, W. S. Seow, R. J. Drost, T. Tamegai, S. Ooi, M. Konczykowski, and P. H. Kes, *Phys. Rev. B* **55**, R6165 (1997).

238. T. Tsuboi, T. Hanaguri, and A. Maeda, *Phys. Rev. B* **55**, R8709 (197).

239. D. V. Livanov, E. Milani, G. Balestrino, and C. Aruta, *Phys. Rev. B* **55**, R8701 (1997).

240. Y. M. Wan, S. E. Hebboul, and J. C. Garland, *Phys. Rev. Lett.* **72**, 3867 (1994).

241. A. Schilling, R. A. Fisher, N. E. Phillips, U. Welp, D. Dasgupta, W. K. Kwok, and G. W. Crabtree, *Nature* (London) **382**, 791 (1996).

242. U. Welp, J. A. Fendrich, W. K. Kwok, G. W. Crabtree, and B. W. Veal, *Phys. Rev. Lett.* **76**, 4809 (1996).

243. E. Zeldov, D. Majer, M. Konczykowski, V. B. Geshkenbein, V. M. Nivokur, and H. Shtrikman, *Nature* (London) **375**, 373 (1995).

244. Matthew J. W. Dodgson, V. B. Geshkenbein, H. Nordborg, and G. Blatter, *Phys. Rev. Lett.* **80**, 837 (1998).

245. P. L. Gammel, L. F. Schneemeyer, J. V. Waszczak, and D. J. Bishop, *Phys. Rev. Lett.* **61**, 1666 (1988).

246. M. Willemin, A. Schilling, H. Keller, C. Rossel, J. Hofer, U. Welp, W. K. Kowk, R. J. Olsson, and G. W. Crabtree, *Phys. Rev. Lett.* **81**, 4236 (1998).

247. R. G. Beck, D. E. Farrell, J. P. Rice, D. M. Ginsberg, and V. G. Kogan, *Phys. Rev. B* **68**, 1594 (1992).

248. H. N. Bachman, A. P. Reyes, V. F. Mitrovic, W. P. Halperin, A. Kleinhammes, P. Kuhns, and W. G. Moulton, *Phys. Rev. Lett.* **80**, 1726 (1998).

249. S. L. Lee, P. Zimmermann, H. Keller, M. Warden, I. M. Savić, R. Schauwecker, D. Zech, R. Cubitt, E. M. Forgan, P. H. Kes, T. W. Li, A. A. Menovski, and Z. Tarnawski, *Phys. Rev. Lett.* **71**, 3862 (1993).

250. T. Blasius, Ch. Niedermayer, J. L. Tallon, D. M. Pooke, A. Golnik, and C. Bernhard, *Phys. Rev. Lett.* **82**, 4926 (1999).

251. Philip Kim, Zhen Yao, and Charles M. Lieber, *Phys. Rev. Lett.* **77**, 5118 (1996).

252. A. Oral, J. C. Barnard, S. J. Bending, I. I. Kaya, S. Ooi, T. Tamegai, and Henini, *Phys. Rev. Lett.* **80**, 3610 (1998).

253. R. Cubitt, E. M. Forgan, G. Yang, S. L. Lee, D. Mck. Paul, H. A. Mook, M. Yethiraj, P. H. Kes, T. W. Li, A. A. Menovsky, Z. Tarnawski, and K. Mortensen, *Nature* (London) **365**, 407 (1993).

254. T. T. M. Palstra, B. Batlogg, L. F. Schneemeter, and J. V. Waszczak, *Phys. Rev. Lett.* **61**, 1662 (1988).

255. J. Bardeen and M. J. Stephen, *Phys. Rev.* **140**, A1197 (1965).

256. T. W. Krause, T. R. Chien, An-Chang Shi, and W. R. Datars, *Physica C* **224**, 13 (1994).

257. H. Yamasaki, K. Endo, S. Kosaka, M. Umeda, S. Yoshida, and K. Kajimura, *Phys. Rev. Lett.* **70**, 3331 (1993).

258. P. Wagner, U. Frey, F. Hillmer, and H. Adrian, *Phys. Rev. B* **51**, 1206 (1995).

259. V. M. Vinokur, M. V. Feigel'man, V. B. Geshkenbein, and A. I. Larkin, *Phys. Rev. Lett.* **65**, 259 (1990).

260. M. V. Feigel'man and V. M. Vinokur, *Phys. Rev. B* **41**, 8986 (1990).

261. V. Geshkenbein *et al., Physica C* **162-164**, 239 (1989).

262. M. Tinkham, *Phys. Rev. Lett.* **61**, 1658 (1988).

263. J. Owliaei, S. Sridhar, and J. Talvacchio, *Phys. Rev. B* **69**, 3366 (1992).

264. H. Pastoriza and P. H. Kes, *Phys. Rev. Lett.* **75**, 3525 (1995).

265. B. Batlogg, T. T. Palstra, L. F. Schneemeyer, and J. V. Waszczak, in *Strong Correlation and superconductivity*, ed. by H. Fukuyama, S. Maekawa, and A.P. Malozemoff (Spinger-Verlag, Berlin, 1989), p.349.

266. T. T. M. Palstra, B. Batlogg, L. F. Schneemeyer, R. B. van Dover, and J. V. Waszczak, *Phys. Rev. B* **38**, 5102 (1988).

267. L. Miu, G. Jakob, P. Haibach, F. Hillmer, H. Adrian, and C. C. Almasan, *Phys. Rev. B* **57**, 3151 (1998).

268. H. Yamasaki, K. Endo, S. Kosaka, M. Umeda, S. Yoshida, and K. Kajimura, *Phys. Rev. B* **49**, 6913 (1994).

269. J. A. Fendrich, W. K. Kwok, J. Giapintzakis, C. J. van der Beek, V. M. Vinokur, S. Fleshler, U. Welp, H. K. Viswanathan, and G. W. Crabtree, *Phys. Rev. Lett.* **74**, 1210 (1995).

270. D. López, L. Krusin-Elbaum, H. Safar, E. Righi, F. de la Cruz, S. Grigera, C. Field, W. K. Kwok, L. Paulius, and G. W. Crabtree, *Phys. Rev. Lett.* **80**, 1070 (1998).

271. W. K. Kwok, L. M. Paulius, V. M. Vinokur, A. M. Petrean, R. M. Ronningen, and G. W. Crabtree, *Phys. Rev. Lett.* **80**, 600 (1998).

272. S. N. Gordeev, A. P. Rassau, R. M. Langan, P. A. J. de Groot, V. B. Geshkenbein, R. Gagnon, L. Taillerfer, preprint (to be published in *Phys. Rev. B*).

273. S. Sarti, D. Neri, E. Silva, R. Fastampa, and M. Giura, *Phys. Rev. B* **56**, 2356 (1997); E. Silva, S. Sarti, M. Giura, R. Fastampa, and R. Marcon, *Phys. Rev. B* **55**, 11115 (1997).

274. A. A. Zhukov, H. Kupfer, G. Perkins, L. F. Cohen, A. D. Caplin, S. A. Klestov, H. Claus, V. I. Voronkova, T. Wolf, and H. Wuhl, *Phys. Rev. B* **51**, 12704 (1995).

275. K. Deligiannis, P. A. J. de Groot, M. Oussena, S. Pinfold, R. Langan, R. Gagnon, and L. Taillefer, *Phys. Rev. Lett.* **70**, 2121 (1997).

276. B. Khaykovich, E. Zeldov, D. Majer, T. W. Li, P. H. Kes, and M. Konczykowski, *Phys. Rev. Lett.* **76**, 2555 (1996).

277. H. Darhmaoui and J Jung, *Phys. Rev. B* **53**, 14621 (1996).

278. Henrik Jeldtoft Jensen and Peter Minnhagen, *Phys. Rev. Lett.* **66**, 1630 (1991).

## Chapter 8

279. M. Tinkham, *Physica C* **235-240**, 3 (1994).

280. G. Blatter, V. B. Geshkenbein, and A. I. Larkin, *Phys. Rev. Lett.* **68**, 875 (1992).

281. T.T. M. Palstra, B. Batlogg, L. F. Schneemeyer, and J. V. Waszczak, *Phys. Rev. B* **43**, 3756 (1991).

282. D. E. Farrel, S. Bonham, J. Forster, Y. C. Chang, P. Z. Jiang, K. G. Vandervoort, D. J. Lam, and V. G. Kogan, *Phys. Rev. Lett.* **63**, 782 (1989).

283. R. Kleiner, F. Steinmeyer, G. Kunkel, and P. Müller, *Phys. Rev. Lett.* **68**, 2394 (1992).

284. J. C. Martínez, S. H. Brongersma, A. Koshelev, B. Ivlev, P. H. Kes, R. P. Griessen, D. G. de Groot, Z. Tarnavski, and A. A. Menovsky, *Phys. Rev. Lett.* **69**, 2276 (1992).

285. S. L. Lee, P. Zimmermann, H. Keller, M. Warden, I. M. Savic, R. Schauwecker, D. Zech, R. Cubitt, E. M. Forgan, P. H. Kes, T. W. Li, A. A. Menovsky, and Z. Tarnawski, *Phys. Rev. Lett.* **71**, 3862 (1993).

286. Y. Ando, S. Komiya, Y. Kotaka, and K. Kishio, *Phys. Rev. B* **52**, 3765 (1995), and errata, **59**, 6564 (1999).

287. C. M. Aegerter, S. L. Lee, H. Keller, E. M. Forgan, and S. H. Lloyd, *Phys. Rev. B* **54**, R15661 (1996).

288. R. Busch, G. Ries, H. Werther, G. Kreiselmeyer, and G. Saemann-Ischenko, *Phys. Rev. Lett.* **69**, 522 (1992).

289. Ichiro Matsubara, H. Tanigawa, T. Ogura, H. Yamashita, and M. Kinoshita, *Phys. Rev. B* **45**, 7414 (1992).

290. L. Miu, P. Wagner, U. Frey, A. Hadish, Dana Miu, and H. Adrian, *Phys. Rev. B* **52**, 4553 (1995).

291. M. Rapp, A. Murk, R. Semerad, and W. Prusseit, *Phys. Rev. Lett.* **77**, 928 (1996).

292. M. V. Feigel'man, V. B. Geshkenbein, and A. I. Larkin, *Physica C* **167**, 177 (1990).

293. G. Balestrino, M. Marinelli, E. Milani, A. A. Varlamov, and L. Yu, *Phys. Rev. B* **47**, 6037(1993).

294. Y. F. Yan, P. Matl, J. M. Harris, and N. P. Ong, *Phys. Rev. B* **52**, R751 (1995).

295. Yuyao Zha, S. L. Cooper, and David Pines, *Phys. Rev. B* **53**, 8253 (1996), and references therein.

296. N. E. Hussey *et al.*, *Phys. Rev. B* **56**, R11423 (1997)

297. C.F. Hempstead and Y.B. Kim, *Phys. Rev. Lett.* **12**, 145 (1964); Y.B. Kim, C.F. Hempstead, and A. R. Strnad, *Phys. Rev.* **131**, 2486 (1963).

298. C. Caroli, P. G. de Gennes, and J. Matricon, *Phys. Lett.* **9**, 307 (1964).

299. N. B. Kopnin and G. E. Volovik, *Phys. Rev. Lett.* **79**, 1377 (1997).

300. J. M. Harris, Y. F. Yan, O. K. C. Tsui, Y. Matsuda, and N. P. Ong, *Phys. Rev. Lett.* **73**, 1711 (1994).

301. N. B. Kunchur, D. K. Christen, and J. M. Phillips, *Phys. Rev. Lett.* **70**, 998 (1993).

302. R. Cubitt *et al.*,.*Nature* (London) **365**, 407 (1993).

303. B. Khaykovich, M. Konczykowski, E. Zeldov, R. A. Doyle, D. Majer, P. H. Kes, and T. W. Li, *Phys. Rev. B* **56**, R517 (1997).

304. Lu Zhang, J. Z. Liu, and R. N. Shelton, *Phys. Rev. B* **45**, 4978 (1992).

305. N. B. Kopnin and A. V. Lopatin, *Phys. Rev. B* **51**, 15291(1995).

306. J. M. Harris, Z.-X. Shen, P. J. White, D. S. Marshall, and M. C. Schabel, *Phys. Rev. B* **54**, R15665 (1996).

307. T. Jacobs, S. Sridhar, Q. Li, G. D. Gu, and N. Koshizuka, *Phys. Rev. Lett.* **75**, 4516 (1995).

308. Y. Matsuda *et al.*, *Phys. Rev. B* **49**, 4380 (1994).

309. S. G. Doettinger, R. P. Huebener, S. Kittleberger, and C. C. Tsuei, *Europhys. Lett.* **33**, 641 (1996).

310. Y. G. Uemura *et al.*, *Phys. Rev. B* **38**, 909 (1988).

University of Alberta Library
0 1620 1494 1072

B45386